ADAPTIVE OPTICS AND STRUCTURED ILLUMINATION IN FLUORESCENCE MICROSCOPY

by

BENJAMIN ALAN THOMAS

(Under the Direction of Peter Kner)

ABSTRACT

Fluorescence microscopy has become one of the most important tools for biological investigation. Unfortunately, diffraction limits the resolution of fluorescence microscopy to about 250nm for high numerical apertures, leaving many cellular features unresolved. Several techniques have been developed to breach the resolution limit of fluorescence microscopes, one of which is structured illumination microscopy (SIM).

SIM is based on the Moiré effect, where the interference of two patterns creates a lower frequency “beat” pattern. In SIM, the sample is illuminated structured pattern. The super-resolution details are encoded into the observed image, but can be mathematically extracted and restored to their proper positions. However, super-resolution details cannot be accurately restored if the illumination pattern is aberrated, which occurs as it passes through a complex biological sample. SIM is thus limited to thin samples without some means of correction, making in vivo imaging impossible and limiting its usefulness

Adaptive Optics (AO) offers a means for correcting sample aberrations, restoring image and illumination pattern fidelity. Over the past 20 years, AO has been applied to various forms

of microscopy. AO systems work by removing aberrations in the optical system through a correction element, which is typically a mirror whose shape can be precisely controlled.

In this dissertation I will present my contributions to the fields of SIM and AO during my graduate career under the direction of Dr. Peter Kner. I will present a new form of optical sectioning SIM and demonstrate its superior performance in comparison to previously reported methods. I will also present our application of AO to Differential Interference Contrast (DIC) microscopy, which has not yet to be reported in literature. This is important as it offers a means of aberration removal for photosensitive samples. Most importantly, I will detail the combination of AO and SIM and demonstrate that 140nm resolution images can be obtained through 35μm of sample tissue.

INDEX WORDS: Adaptive Optics (AO), structured illumination microscopy (SIM), fluorescence microscopy, super-resolution, thick tissue imaging

ADAPTIVE OPTICS AND STRUCTURED ILLUMINATION IN FLUORESCENCE MICROSCOPY

by

BENJAMIN ALAN THOMAS

B.S.A.E., University of Georgia, 2008

M.S., University of Georgia, 2011

A Dissertation Submitted to the Graduate Faculty of The University of Georgia in Partial Fulfillment of the Requirements for the Degree

DOCTOR OF PHILOSOPHY

ATHENS, GEORGIA

2014

ADAPTIVE OPTICS AND STRUCTURED ILLUMINATION IN FLUORESCENCE MICROSCOPY

by

BENJAMIN ALAN THOMAS

Major Professor:	Peter Kner
Committee:	Mark Haidekker
	Bingqian Xu

Electronic Version Approved:

Julie Coffield
Interim Dean of the Graduate School
The University of Georgia
December 2014

TABLE OF CONTENTS

Page

CHAPTER

CHAPTER 1: INTRODUCTION

For thousands of years, humans have manipulated light with glass. As lens construction methods were enhanced, so was our understanding of the world around us. The pairing of lenses to create telescopes and microscopes opened the door for scientific discovery of worlds both light-years away, and directly in front of us. The discovery of molecules that emit light after absorbing light at a shorter wavelength, gave rise to fluorescence microscopy. The next great advancement in light microscopy resulted from an investigation into the bioluminescence of the jellyfish *Aequorea Victoria*, leading to the Green Fluorescent Protein [1]. With further research, scientist determined how to genetically encode GFP, making the cell responsible for its production alongside a targeted protein [2]. Advancements in labelling specific targets through immunofluorescence have furthered the usefulness of fluorescence microscopy.

The importance of fluorescence microscopy to science cannot be overstated, as it has become one of the main tools of investigation for biological sciences. Unfortunately, diffraction limits the resolution of light microscopes to around 250nm, leaving many cellular details and features un-resolvable. This problem gave rise to super-resolution microscopy, a vastly growing field of research that has received recent international attention. Eric Betzig, Stefan Hell, and William Moerner were awarded the Nobel prize for chemistry in recognition of their

contributions to super-resolution microscopy this year. One of the techniques for breaking the diffraction limit is structured illumination microscopy (SIM)

SIM is based on the Moiré effect, where the interference of two patterns creates a lower frequency “beat” pattern. In SIM, the sample is illuminated with a structured pattern. The observed image contains the beat pattern created by the fluorophore distribution and the illumination structure. The super-resolution details are thus encoded into the observed image and can be mathematically extracted and restored to their proper positions with knowledge of the illumination structure [3]. However, super-resolution details cannot be accurately restored if the illumination pattern is distorted, which occurs as it travels through a complex biological samples. SIM is thus limited to thin samples without some means of correction, making in vivo imaging impossible.

When imaging fluorescent proteins through thick tissue, refractive index differences in the sample, and the refractive index differences between the sample, immersion medium, and cover glass cause distortion in the optical signal [4]. These distortions result in a loss of resolution and a decrease of the signal to noise ratio of the imaging system. In SIM, the illumination pattern suffers from these same aberrations. In fact, the performance of all super-resolution techniques depends on the system resolution. Aberrations that increase the width of the PSF will adversely affect the resolutions obtainable through these advanced techniques. Furthermore, aberrations will also decrease the peak intensity of the PSF which results in fewer photons being captured. Adaptive Optics offers a means for correcting aberrations and restoring image fidelity.

The development of a method to correct aberrations in imaging systems originated in the field of astronomy. Adaptive Optics (AO) is a technique designed for ground based telescopes to correct aberrations in the images caused by the earth's atmosphere. Over the past 20 years, the application of AO to microscopy has been performed for many different forms of microscopy. AO systems work by removing aberrations in the optical system through a correction element, which is typically a mirror whose shape can be precisely controlled. The illumination pattern needed for SIM can also be passed through the deformable mirror so that the pattern fidelity can be restored through the aberrant sample.

SIM and AO are important techniques that have extended the resolution and depth capabilities of fluorescence microscopes. Combining AO and SIM allows super-resolution images of fluorescent samples to be obtained through thick tissue, which is an important step towards in-vivo imaging. The development of the fluorescence microscope and discovery of GFP led to many important scientific discoveries. Continuing to develop these tools will lead to investigation at ever improving levels of detail, which historically proven to lead to new discoveries

In this dissertation, I will present the contributions to the fields of AO and SIM that I have made during graduate career under the direction of Dr. Peter Kner. My dissertation is organized as follows. Chapter 2 will provide basic background information on fluorescence microscopy, image system quality, and aberrations in microscopy. This will lead to an introduction to Adaptive Optics, where its basic principles will be presented and followed by a review of reported advances. Chapter 3 will introduce SIM. I will discuss the underlying physical principles behind SIM and review pertinent reported applications. In Chapter 4, I will

introduce our microscope system and present the optical elements needed to implement AO and SI.

Chapters 5 presents our contribution to SIM, a new optical sectioning method with enhanced resolution. A careful comparison to other algorithms reveals the superior performance of our algorithm. The implementation of the AO system and its combination with the SIM system (AO-SIM) are presented in Chapter 6. AO is demonstrated to improve the depth capabilities of SIM. In Chapter 7, I will discuss the use of AO in Differential Interference Contrast (DIC) microscopy, an application of AO that has yet to be reported which may be of particular use for photosensitive samples. The final chapter provides a summary of our contributions to the fields of AO and SIM and a glimpse at the next steps to combining these technologies.

CHAPTER 2: ADAPTIVE OPTICS - BACKGROUND AND LITERATURE REVIEW

In this chapter, I will review background information pertaining to applying Adaptive Optics to fluorescence microscopy. The discussion begins with microscopy basics, such as fluorescence, optical system resolution, and the causes and effects of aberrations. This will lead to an introduction to aberration correction with Adaptive Optics (AO). A review of the history of this technology and the basic principles of its operation will follow. In the second half of this chapter, I will provide an overview of the application of AO to numerous forms of microscopy.

Fluorescence microscopy basics

A Chromophore is a portion of a molecule that can absorb light. If the Chromophore emits light after absorbance, it is known as a Fluorophore. Fluorescence is the re-emission of light by a substance that has absorbed light at a shorter wavelength. When a Fluorophore

absorbs light, the energy moves electrons from the ground state to an excited state (Figure 2.1). The excited electron will transfer some energy to the vibrational states of the molecule. The electron then returns to the ground state by emitting energy as a photon. The emitted light is slightly red shifted (lower energy) compared to the absorbed light, due to energy lost in the excited state. This red-shifting of the excitation light is known as the Stoke's shift [5].

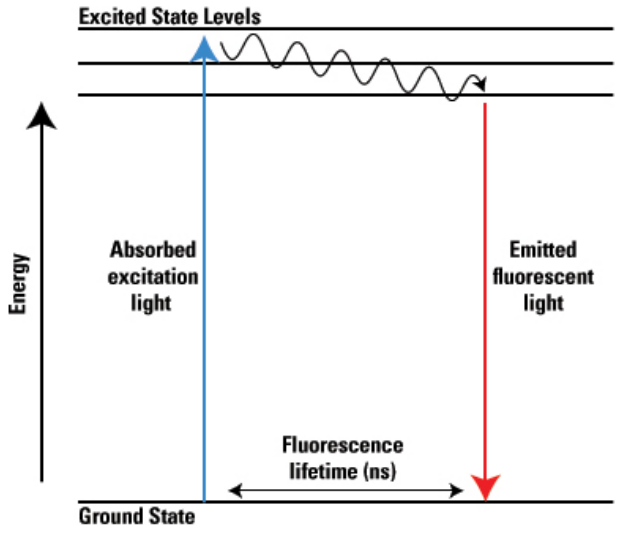

Figure 2.1: Absorption and emission of light by a fluorophore.

Fluorophores have been developed that absorb and emit at various wavelengths. As an example, the excitation and emission spectra for a common fluorophore, Alexa 488, are shown in Figure 2.2. Methods to attach fluorophores and dyes to specific proteins have furthered their scientific importance. Immunofluorescence and genetic encoding are two of the most common methods attaching fluorescent molecules to biological targets.

Immunoflourescence is based on the antibody/antigen relationship, where antibodies have binding sites that are specific to a certain bacteria or virus. Flourophores can be chemically linked to an antibody that will attach itself to the target (antigen). Primary immunoflourescence refers to a direct connection between label and target. Secondary, or indirect, immunofluorescence utilizes a non-fluorescent primary antibody which attaches to the target and has multiple binding sites for the secondary, fluorescent antibody.

The Green Flourescence Protein (GFP) is a naturally occurring fluorescent protein found in the jellyfish *Aequorea victoria [1]*. Consisting of 238 amino acids, GFP can be encoded into the genome of the organism being studied so that the production of GFP is controlled by the organism alongside its target protein. The excitation and emission spectra for GFP are also shown in Figure 2.2. Proteins, which all share the same 20 amino acids, could not be optically distinguished without immunofluorescence or genetic encoding.

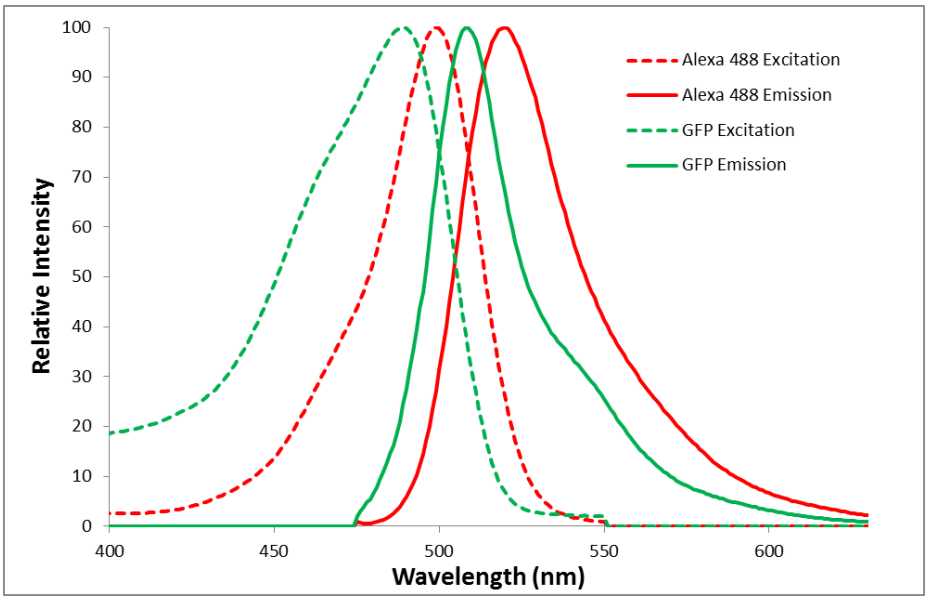

Figure 2.2: Excitation and emissison spectra for Alexa 488 and GFP.

Fluorescence microscopes were first developed in the 1940s and work by exciting the fluorophores in the sample with excitation light, then separating the fluorescent signal from the much stronger excitation light so that only light from the fluorophores is observed. Figure 2.3 displays a simplified fluorescence microscope setup. The excitation light and fluorescence signal are separated by a dichroic mirror so that only the much weaker fluorescence signal will reach the CCD camera.

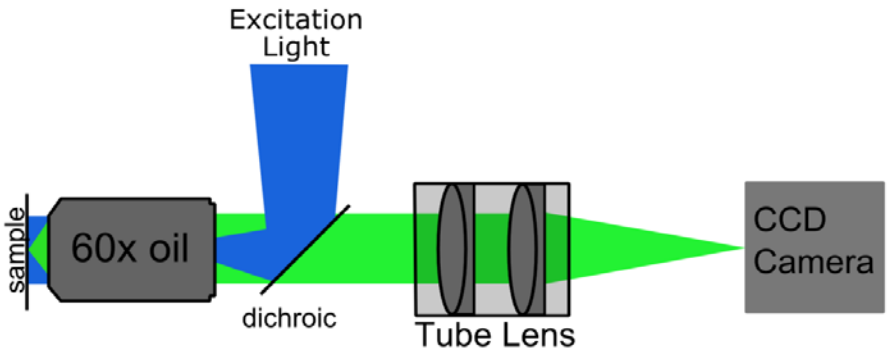

Figure 2.3: Fluorescence microscope basic setup

Image resolution in microscopy

When acquiring an optical image, it is desirable to acquire the best reproduction of the object possible. However, as light passes through an aperture, it bends. This is a phenomenon known as diffraction [6]. The diffraction limit is an inherent limit to optical resolution and is a result of the wave nature of light. Generally, if all of the elements of an optical system are perfect, then the resolution is said to be diffraction limited. The resolution limit that is due to

diffraction is inherent in Maxwell's equations for the propagation of light, and cannot be overcome. Therefore, the possible resolution that can be obtained in conventional optical systems is limited [7].

The image of a point source is the Point Spread Function (PSF) of the microscope and determines the system resolution. In optical systems with circular apertures, such as microscopes, diffraction causes light from point source passing through the aperture to form an image of a bright spot with concentric circular rings, known as Airy disks. A simulated PSF is shown in Figure 2.4 and is scaled to enhance visualization of the outer rings.

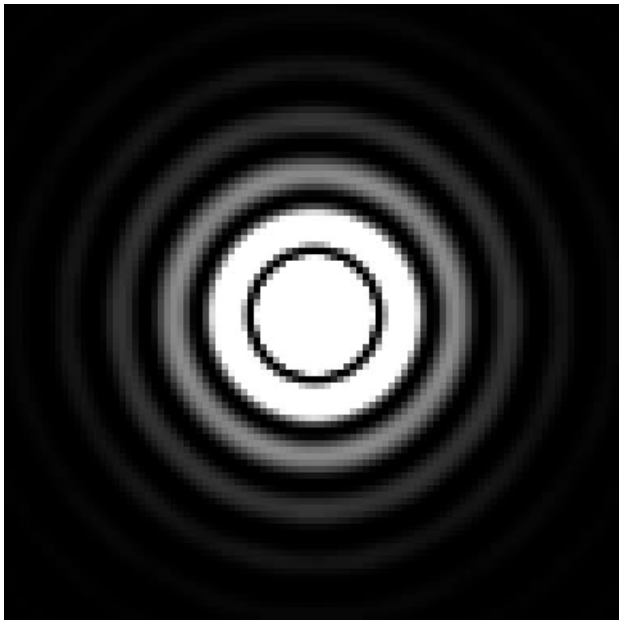

Figure 2.4: Simulated PSF scaled to enhance the Airy rings. The maximum displayed pixel value is 1% of the maximum intensity value.

The Rayleigh criterion is a measure of the minimum resolvable detail. If two point sources are close to each other, their images, the airy discs, will overlap. When the principle diffraction maximum of one Point-Spread-Function (PSF) coincides with the first minimum of the other, the two point sources are regarded as just resolved. This is a measurement of resolution., The diffraction limited resolution of a microscope is given by

$$R = 0.61\lambda/NA, \qquad \textbf{Eq. (2.1)}$$

where R is resolution and λ is the wavelength of light. The Numerical Aperture (NA) is a dimensionless quantity based on the maximum angle of light collection of the microscope lens defined as

$$NA = n \sin(\theta), \qquad \textbf{Eq. (2.2)}$$

where *n is the* index of refraction of the immersion medium, and θ is the half angle of the maximum cone of light that can enter the lens. It is obvious from this equation that systems with a higher numerical aperture will be able to resolve smaller details.

Point spread function (PSF)

When evaluating the performance of an optical system, the size of the PSF is the critical parameter [8]. The effect of wavefront aberrations on the PSF can be described using Fourier Optics. For a microscope objective, the plane one focal length in front of the lens is referred to as the focal plane while the plane one focal length behind the lens is referred to as the back pupil plane. The light from a point source can be considered coherent as the source is infinitesimal. For coherent light, the amplitude at the back pupil plane is the Fourier transform of the amplitude at the focal plane [9]. The relationship between the PSF and the back pupil plane is given by [10]

$$PSF = H(r) = |\int P(s)e^{i\phi(s)}e^{(\frac{i2\pi}{\lambda})(\frac{ds^2}{2f^2})}e^{(\frac{-i2\pi}{\lambda})\bar{s}\bar{r}}ds|^2 \quad \textbf{Eq. (2.3)}$$

where $P(u,v)$ describes the aperture of the objective, and u and v are spatial coordinates. Essentially, the PSF is the square of the absolute value of the Fourier transform of the pupil function. $P(u,v)$ describes the aperture of the objective, where u and v are the x and y coordinates. $P(u,v)$ for a circular aperture given by:

$$P(K_{x,}K_y) = \begin{cases} 1 & for\ \sqrt{u^2+v^2} \leq \frac{NA}{\lambda} \\ 0 & for\ \sqrt{u^2+v^2} > \frac{NA}{\lambda} \end{cases} \quad \textbf{Eq. (2.4)}$$

When dealing with an imperfect system, the optical field is distorted and the equation for the PSF changes to [9]

$$H = |\int\int P(u,v)e^{i\Phi(u,v)}e^{iux+ivy}\,du\,dv|^2 \quad \textbf{Eq. (2.5)}$$

where *Φ(u,v)* describes the wavefront aberrations. A 3D PSF can be generated by including the defocus in the calculation of the PSF, so the response becomes a function of both lateral position and axial defocus. To simplify the expression for the PSF, let

$$r = \sqrt{u^2+v^2} \quad \textbf{Eq. (2.6)}$$

As the aperture is radially symmetric, the magnitude of the vector in (*u*,*v*) coordinates is what is important. The 3D PSF can now be written as

$$H = |\int P(r)e^{i\phi(r)}e^{(\frac{i2\pi}{\lambda})(\frac{dr^2}{2f^2})}dr|^2 \quad \textbf{Eq. (2.7)}$$

where f is the effective focal length of the system and d is the axial offset from focus. Wavefront aberrations are represented by *Φ(r)* in Equation 2.5 and 2.7. As described by Goodman, the effect of aberrations can be completely described by introducing phase distortions within the imaging systems bandwidth [9] . A common form of expressing aberrations in images is by expanding *Φ* in Zernike polynomials. Zernike polynomials form a complete set on a unit circle,

meaning that any aberration can be described as the sum of these polynomials [11]. The lowest orders of Zernike polynomials correspond to common optical aberrations such as: wavefront tilt, defocus, and astigmatism [8]. Zernike polynomials have been exceptionally useful in adaptive optics as a basis set for the analytic evaluation of wavefront error [12].

The effect of aberrations on the PSF is simulated using the Zernike Polynomial corresponding to spherical aberrations (defocus)

$$\phi_{Def} = M(2\rho^2 - 1) \qquad \textbf{Eq. (2.8)}$$

and astigmatism,

$$\phi_{Astig} = M\rho^2 \sin 2\theta \qquad \textbf{Eq. (2.9)}$$

where ρ and is the normalized radial distance, and *M* is referred to as the magnitude. In general, the Zernike aberrations modes used throughout this study are normalized to an amplitude of 1 radians, and thus are 2 radians peak to valley. The aberration magnitude (*M)* is used for convenience throughout this paper to describe the maximum aberration amplitude (in radians). For this simulation, Equation 2.8 and 2.9 are inserted into Equation 2.5 with magnitudes of $\frac{\pi}{2}$ radians. Horizontal profiles through the ideal and aberrated PSFs are shown in Figure 2.5. The ratio of the peak intensity measured in the presence of aberration divided by the intensity with no aberrations present is known as the Strehl ratio. In Figure 2.5 the Strehl ratio of the PSFs distorted by defocus and astigmatism are 0.41 and 0.62 respectively.

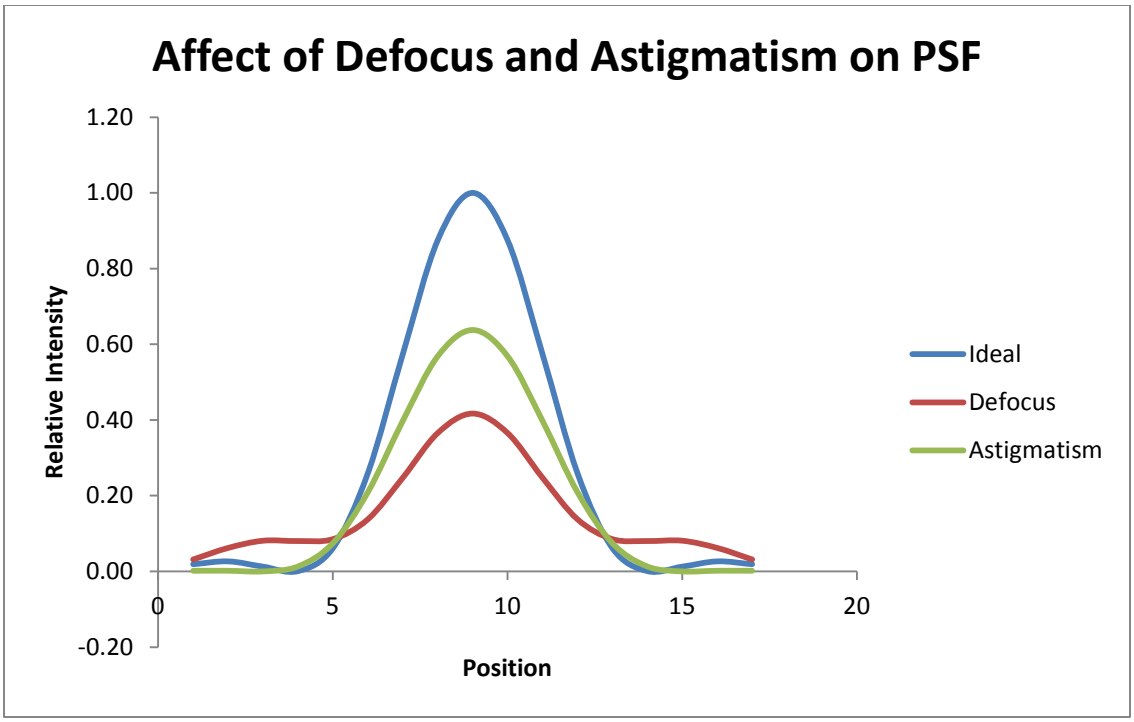

Figure 2.5: Ideal PSF compared to PSF distortions caused Defocus and Astigmatism aberrations at amplitude of $\pi/2$ radians

The image captured by an optical system (*D)* is mathematically represented as

$$D_i(r) = E(r) \otimes H(r) \qquad \textbf{Eq. (2.10)}$$

where *E(r)* is the light emitted from the sample and *H* is the impulse response (PSF) of the system. We see from the equation that the image is simply the convolution of the sample fluorescence with the PSF of the imaging system. The imaging system essentially acts as a low pass filter, as demonstrated by Figure 2.6. The center image of the figure is the diffraction limited PSF of the system. The image on the right represents what is captured by the optical system from the full resolution object on the left. The inset of Figure 2.6 shows that the details of the patterned shirt are almost completely filtered out by the simulated imaging system.

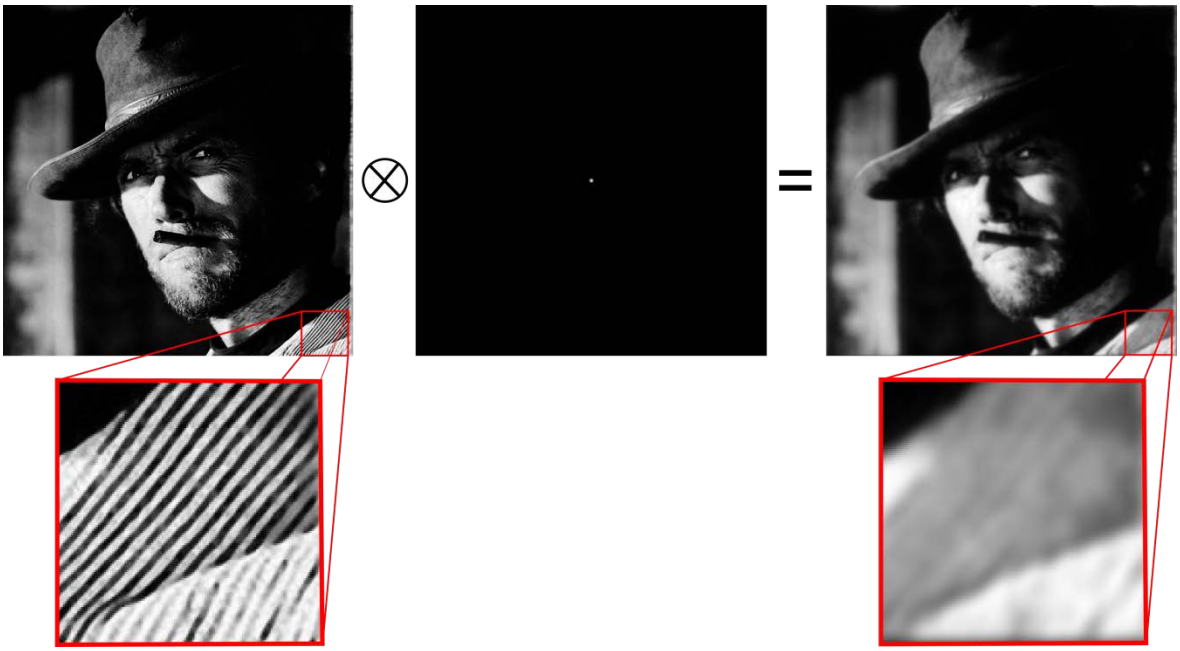

Figure 2.6: The observed image (right) is the object convolved with the PSF. The inset shows that the details of the shirt pattern are almost completely filtered out by the imaging system.

Optical transfer function (OTF)

The Fourier Transform of the PSF is known as the Optical Transfer Function (OTF). The OTF describes the frequency response of the imaging system. In two dimensions, the OTF for a fluorescence microscope with perfectly coherent light is simply a circle with limits described by Equation 2.4. The incoherent OTF is given by the autocorrelation of the coherent OTF. The frequency transmission for the incoherent and coherent 2D OTF for a circular aperture are shown in Figure 2.7. As shown, high frequency information is strongly attenuated near the resolution limit of the incoherent case. The region of support under coherent illumination is limited to NA/λ and the steep drop off results in ringing artifacts that degrade image quality.

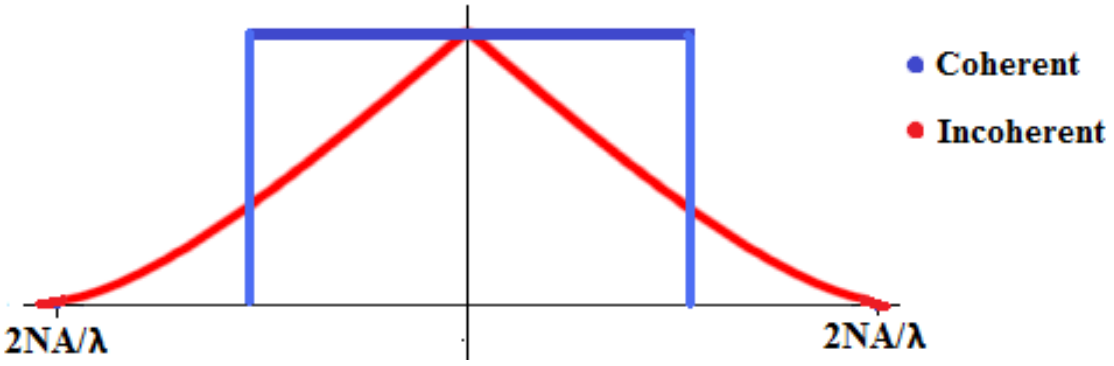

Figure 2.7: Normalized frequency support across the 2D OTF under coherent and incoherent illumination.

The diffraction limit manifests itself in the OTF as a region-of-support, where details outside the region-of-support are not present in the image. The complex OTF describes how strongly a certain frequency is represented in the data. Extending the resolution of a microscope is essentially extending the region of support of the OTF. The two dimensional diffraction limited region of support for a conventional fluorescence microscope is given by

$$k_{x,y} = 2NA/\lambda. \qquad \textbf{Eq. (2.11)}$$

A cross-section of the OTF for conventional microscope in three dimensions is shown in Figure 2.8. The region of support is torus shaped. Information just above and below the xy-plane along the z-axis is not inside the region of support of the OTF. This "missing cone" means that conventional light microscopes do not eliminate light from out-of-focus planes. Figure 2.9 gives the cross section of a simulated 3D PSF. The image of the point source appears to be elongated in the z-direction, which is due to the out-of-focus light being present in the image slice. The frequency content of a captured image can be acquire by taking the Fourier transform of Equation 2.10 and is given by

$$\widetilde{D}(k) = \tilde{E}(k)\widetilde{H}(k) \qquad \textbf{Eq. (2.12)}$$

where k is the frequency space coordinates with units of 1/length and the tilde denotes the Fourier Transform. It is important to note at this point that multiplication in the frequency domain corresponds to convolution in the spatial domain. The PSF essentially gives information about the optical system transfers information in the spatial domain while the OTF describes how information is transferred through the optical system in the frequency domain.

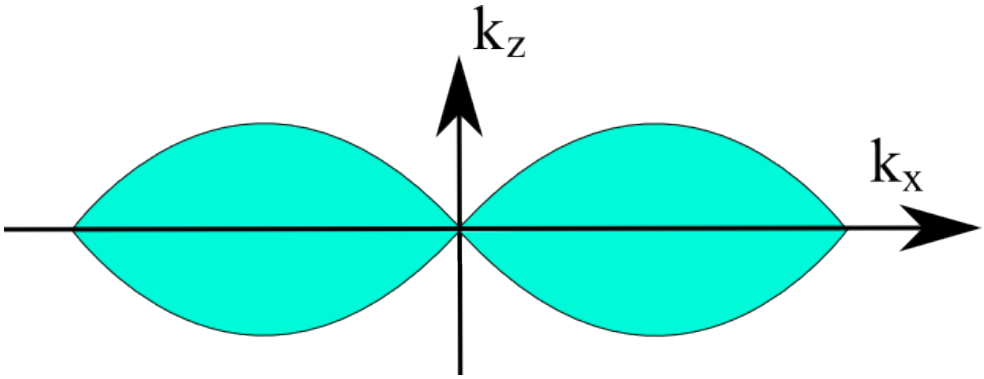

Figure 2.8: Region of support for a conventional fluorescence microscope

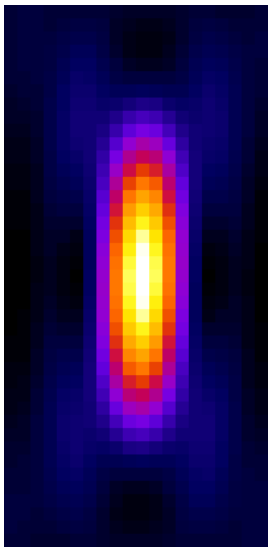

Figure 2.9: Axial Cross-section through the PSF for a conventional fluorescence microscope.

Sources of aberration in microscopy

Although the diffraction limit of an optical system cannot be breached with conventional methods, the images can be corrected for aberrations that prevent the imaging system from reaching its diffraction limit. Aberrations, in general, are distortions in image formation due to the optical system. In astronomy, aberration is experienced when light from a distant object becomes distorted by the varying refractive index of earth's atmosphere [8]. In microscopy, aberrations are caused by refractive index differences in the sample, and the refractive index differences between the sample, immersion medium, and cover glass. Sources of aberration in microscopy are demonstrated in Figure 2.10. Figure 2.10a shows an unaberrated case, where the wavefront at the back pupil plane is flat. Figure 2.10b shows the distortion of the wavefront caused by imaging through a sample that has a complex biological structure of varying refractive

indices. The aberrations due to the specimen being studied tend to be dominated by low order Zernike modes, which are common optical distortions [4].

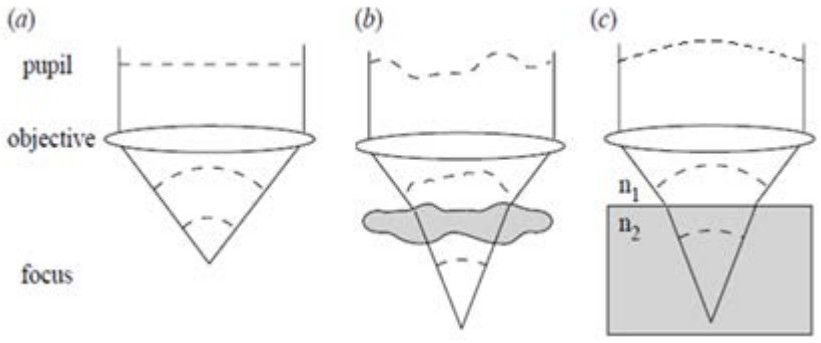

Figure 2.10: Common sources of aberrations in microscopy. (a) An unaberrated system produces a flat wavefront at the back pupil plane. (b)The wavefront is distorted by focusing through a sample with a complex structure and varying indices of refraction. (c) A mismatch between the sample immersion medium index of refraction and the objective lens causes depth aberrations [4].

When the immersion medium has an index of refraction that is not matched to the objective and coverslip, the wavefront is distorted as is shown in Figure 2.10c. The result is commonly referred to as depth aberrations, and is spherical in shape. The result of spherical aberrations is a decrease in the maximum intensity of the PSF and an increase in its width, corresponding to a loss of resolution. This effect increases with depth according to the formula [13, 14]

$$\Phi_{depth}(\rho) = 2\pi \frac{d}{\lambda}\left(n_2\sqrt{1-\left(\frac{(NA)\rho}{n_2}\right)^2} - n_1\sqrt{1-\left(\frac{(NA)\rho}{n_1}\right)^2}\right) \qquad \textbf{Eq (2.13)}$$

where Φ is the resulting aberration, n_1 = refractive index of sample, n_2 = refractive index of immersion medium, d is the depth, and ρ = normalized radial coordinate. In live, complex, biological samples, which contain tissues and organs of varying refractive index, it is impossible to match the index of refraction of the immersion medium, and therefore these aberrations are unavoidable. Adaptive Optics techniques have been proven as a way to improve these PSFs and increase the resolution at depth [14-16].

History of Adaptive Optics

The idea of Adaptive Optics was first developed for applications to astronomy. In 1953, Horace Babcock proposed using a deformable optical element along with a wavefront sensor to improve telescopic images. Babcock noted that without implementation of a system to correct for image aberrations caused by atmospheric turbulence, one was "fortunate to experience one hour out of 1000 of the finest seeing, even at the best locations" [17]. Adaptive optics technology is based on the idea that the effects of an optical system can be altered by removing, adding, or altering the elements within the system [7]. Advancements in computer processing and micro-electro-mechanical systems have allowed the Babcock's idea to become a reality, and Adaptive Optics has since proven to be an effective method for optically correcting image aberrations. A typical setup for a ground based astronomical Adaptive Optics system is shown in Figure 2.11. In this system, a light from a point source or "guide star" that travels through the aberrating medium, in this case earth's atmosphere, is sent to the wavefront sensor. The sensor changes the shape of the adaptive mirror to compensate for aberrations. In general, correction elements consist of a flexible, reflective surface mounted to an array of actuators. An example of the

improvement in image quality from an Adaptive Optics system is displayed in Figure 2.12, which shows Neptune in infrared light with and without correction using Adaptive Optics [18].

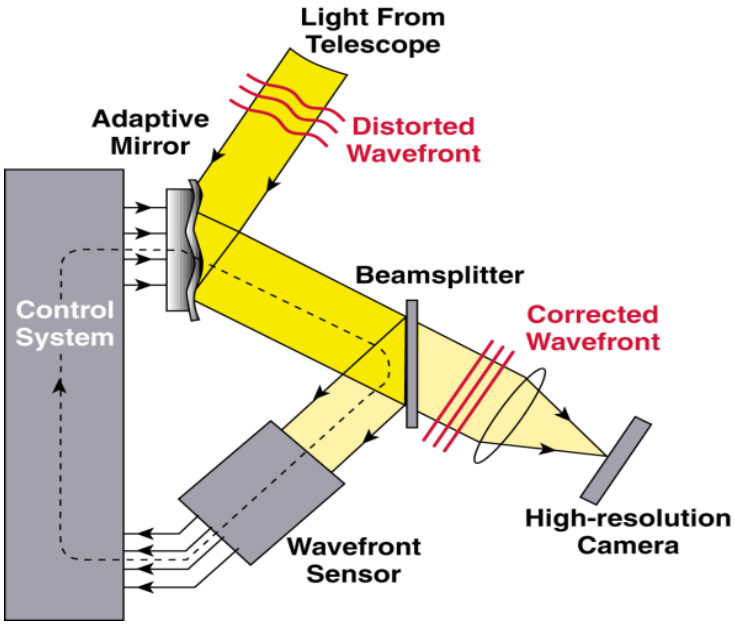

Figure 2.11: A typical ground-based astronomical Adaptive Optics system.

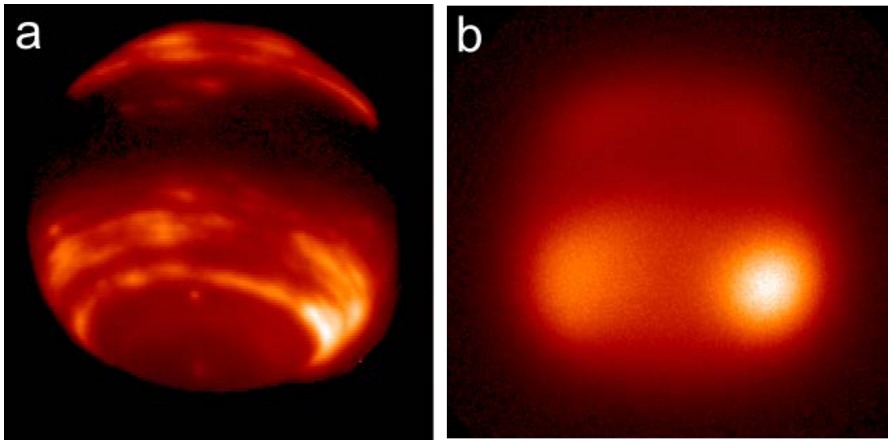

Figure 2.12: Neptune in Infrared Light with (a) and without (b) adaptive optics [18].

Wavefront measurement basics

Various techniques for measuring the wavefront of an optical system exist today. The Foucault Knife Edge Test, Shearing Interferometer, Wavefront Curvature Sensor, and Shack-Hartmann Wavefront Sensor (SHWFS) are a few examples [19] [20]. Generally, techniques for measuring the wavefront of a signal can be divided into two categories: Zonal and Modal [8].

Zonal sensors directly measure the wavefront. This is done by separating the pupil into an array of contiguous zones, or sub-apertures. In each zone, an independent measurement of the gradient, or slope, of the wavefront can be calculated and used to reconstruct the wavefront. In a SHWFS, an array of tiny lenses (called a lenslet array) is aligned to the image plane of the microscope. A point source of light or "guide star," which traverses through the aberrating medium as the sample fluoresces is used as the signal for the SHWFS. The "guide star" signal travels through the lenslet array, and is captured by a detector, most commonly a ccd camera. The resulting array of images or "spots" over the detector represent the sub-apertures. The displacement of these spots from their non-aberrated positions is determined at sub-pixel resolution using centroid calculation or curve fitting fitting [8]. The wavefront gradient is calculated for each respective sub-aperture.

Modal wavefront correction, often called "sensorless" Adaptive Optics, iteratively deduces the errors within the wavefront by their effect on a parameter, most commonly intensity [21]. Typically, low order aberration modes are introduced into the system at various magnitudes. The effects of the induced or "bias" aberrations on the image intensity are used to optimize the optical correction element's shape and produce the maximum possible signal. This type of wavefront correction has shown success in confocal [22] and multiphoton microscopes

[21, 23-25]. Sensorless correction methods are frequently implemented due to the simplicity of their implementation and operation, as well as lower cost.

Deformable mirrors

The low spatial frequency of the aberrations modes that occur due to imaging through a complex sample can be corrected by with Deformable Mirror (DM) due to the high frequency of actuators, as typical DMs utilize more than 32 actuators. A wide range of deformable mirrors have been developed for Adaptive Optics systems. Deformable mirrors have been manufactured to fit a wide variety of applications and usually fall into one of two categories: segmented and continuous surface mirrors. Segmented deformable mirrors have rectangular or hexagonal reflective surfaces can be raised or lowered individually. They are capable of correcting for two-axis tilt with piezoelectric and hydraulic actuators. Continuous surface deformable mirrors consist of a flexible reflective surface that is attached to an actuator array. A compressive review of the basic technology and requirements of deformable mirror can be found in the paper by Freeman and Pearson [26].

Currently available Adaptive Optics elements have proven suitable for use in correction of microscopic images. The model presented by Kam et al. concluded that the spherical aberrations existing in these images can be corrected and that the correction involves only 2μm of correction for every 10μm of depth [27]. For a sample at a depth of 100μm, the maximum movement of the actuators within the deformable mirror would need to be 20μm. Current manufactured deformable mirrors are capable of making this correction and can be purchased from companies such as Imagine Optic, Boston Micromachines, and OKO Technologies.

Literature review introduction

The effectiveness of adaptive optics technology applied to astronomy has been well documented [8]. This section will review applications of Adaptive Optics (AO) to various forms of microscopy. Over the past 25 years, AO has been applied to multi-photon microscopy [13, 23, 24, 28, 29], confocal microscopy [22], harmonic generation microscopy [30], wide field fluorescence microscopy, [14, 16], and optical sectioning structured illumination microscopy [31].

Adaptive Optics and two-photon microscopy

Two photon microscopy was developed in 1990 and is based on the idea that two photons of low energy can excite a fluorophore by simultaneously absorption [32, 33]. The probability of two photons being absorbed at the same time is extremely low, so a high concentration of excitation photons is necessary. A high temporal concentration of photons is achieved with a femto-second pulsed laser. Because two-photon excitation has a much higher probability of occurring within the tightly focused laser spot, out-of-focus fluorescence is not excited and does not need to be rejected with a pinhole as in single photon excitation. The fluorescence from the focal point is collected and the focal plane is scanned throughout the sample to form a complete image. A typical two-photon microscope setup is shown in Figure 2.13 [34]. The x-y mirror scans the sample with the pulsed excitation laser. A dichroic mirror separates the fluorescence from the excitation laser and the image is formed at the photon sensor.

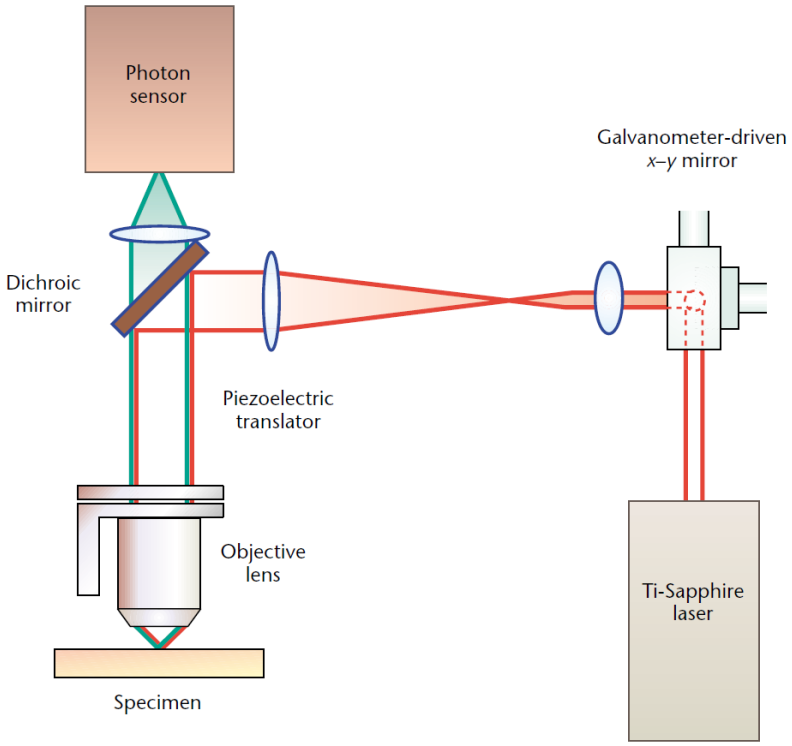

Figure 2.13: Typical two-photon microscope setup [34].

The successful implementation of an Adaptive Optics system in two-photon microscopy was first accomplished by Albert et al. [28]. In their system, the excitation beam is focused with a parabolic mirror, which suffers from large amounts of coma and astigmatism as the sample is scanned from its aligned initial position. A deformable mirror is placed in the excitation path to compensate for these aberrations. Its shape is optimized using the two-photon signal and a genetic learning algorithm with a Zernike mode basis. Using a thin β-barium borate crystal, they were able to obtain a 9 fold increase in the scan area with a Strehl ratio of 0.5 as the minimum acceptable signal.

Neil et al. demonstrated that specimen induced aberrations could be corrected in two photon microscopy using adaptive optics using a ferro-electric liquid crystal spatial light

modulator (FLCSLM) to measure and correct wavefront aberrations [24]. Aberrations were measured using a modal wavefront sensing technique, which measures and corrects individual Zernike aberration modes sequentially. They demonstrated correction of aberrations caused by a refractive index mismatch within the sample by restoring the optical sectioning capabilities of the two-photon microscope. This was accomplished by imaging fluorescent microbeads underneath 28μm of water at the coverslip with and without AO correction compared to beads fixed to the coverlsip [25].

Rueckel et. al. demonstrated a focus near the diffraction limit using a coherence-gated wavefront sensor (CGWS) and deformable mirror to correct aberration in a two-photon fluorescence microscope. The CGWS creates a virtual Shack-Hartmann with an interferometer and uses back-scattered light to determine the wavefront. This is important as the back-scattered light is independent of sample fluorescence, which allows low levels of excitation power to be used in the wavefront calculation. They demonstrated their system by correcting aberrations caused by a transgenic zebrafish (*Danio rerio)* larvae. With a single correction, they found image improvement over a 34μm x 34μm field of view [29].

In another two photon system, Marsh et al. demonstrated the correction of specimen induced aberrations using a 15mm diameter Deformable Mirror. Optimization of the deformable mirror was based on the magnitude of the two-photon induced fluorescence signal, which required several scans of the sample. Using 105nm fluorescent microbeads, an increase of attainable imaging depth was extended from 3.4μm to 46.2μm at a set resolution of a Full-Width-Half-Maximum (FWHM) of 1.25μm. This study also demonstrated a 40 % increase in maximum signal as compared to an uncorrected image of smooth muscle from a guinea pig bladder [13]. A similar system developed by Sherman et al. showed correction of depth induced aberrations by

optimizing the shape of a deformable mirror using the feedback fluorescence and a Genetic Learning algorithm [23].

Chang et al. coupled an image based AO system with a widefield multiphoton microscope [35]. In their AO system, a hill-climbing algorithm corrected the wavefront based on image intensity. Their system showed improved image quality in fluorescent microbeads suspended at various depths in agarose gel. They were able to achieve near video rate with a multi-photon microscope and AO utilizing spatiotemporal focusing. They demonstrated their system with a PMMA thin film. Aberrations were induced by applying nail polish to the coverslip and inserting it into the optical path of the system. A 3.5 fold increase in the mean intensity of a 512x512 image was achieved. They also demonstrated a 2 fold increased in an image of fluorescent microbeads with AO correction [35].

Ji et al. demonstrated AO correction in a two-photon microscope using rear pupil segmentation [36]. A diffraction limited focus is achieved when all rays entering the rear pupil of the objective lens are refocused to the same point with the same phase. Inhomogenieties in the sample, such as index of refraction mismatches will distort some of these rays causing them to miss the intended focus point and interfere non-constructively.

A reference image is first acquired with full illumination. An SLM aligned to the back-pupil plane divides the incoming rays into N sub-regions. All but one of the segments are blocked by applying a binary phase pattern, which causes them to be blocked by an intermediate field stop at an intermediate image plane. An image is acquired with the single segment, which is compared to the reference image to determine the correction needed to return the centroid of the signal back to its ideal focus position. The initial correction for each segment is performed in this manner.

To bring the beams from each segment into phase, two approaches were explored by the authors. The first being direct comparison with a reference beam. The phase of each segment is adjusted to maximize the signal resulting from its interference with the reference beam. In the second approach, the phases are directly extracted from the already determined beam angles. The beam angles are analogous to phase gradients, and an iterative algorithm is used to adjust the phase of each segment. Antibody labeled mouse brain slices 300μm thick were used to demonstrate the system. A two-fold gain in the image intensity was achieved with AO correction [36].

Adaptive Optics and confocal microscopy

Confocal microscopes utilize point illumination to increase optical resolution and contrast. This is accomplished through the use of a spatial pinhole which only allows light produced near the focal plane to be detected. The ability to optically section samples results in increased contrast, but limits the number of photons reaching the detector, which increases noise. Since only one point of the sample is imaged at a time, it necessary to scan the sample in order to produce a full 2D or 3D image [37].

Adaptive Optics systems have been successfully implemented with a confocal microscope [22, 38]. The system implemented by Booth et al. employs a modal sensor which consists of the existing pinhole detector of the confocal microscope and a deformable mirror [22]. A schematic of their microscope is shown as Figure 2.14. The deformable mirror served as the correction element as well as the sensor biasing device. Since the illumination and excitation light travel through reciprocal optical paths, both through the aberrating medium, the deformable mirror must be placed in both paths, as shown in the Figure. Wavefront aberrations were

measured by applying Zernike aberration modes to the deformable mirror and using the effect of each mode on the wavefront to determine the overall aberration.

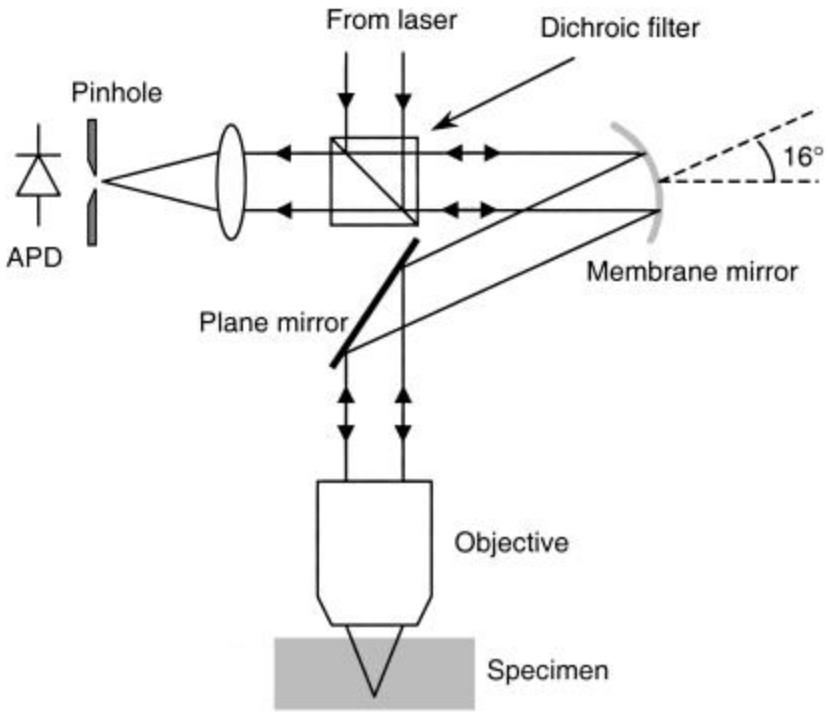

Figure 2.14: AO confocal microscope system [22].

To determine the magnitude of each lower order Zernike mode to be corrected, a positive bias aberration is applied and the sample is scanned, all image pixels were summed and averaged. A second scan is then performed with a negative bias aberration and averaging is repeated. The difference in the bias averages is proportional to the magnitude of aberrations. The mirror commands (c) are then updated by

$$c_{n+1} = c_n + \gamma(W_1 - W_2)\zeta_i \qquad \textbf{Eq. (2.14)}$$

where γ is the user chosen gain, W_1 and W_2 are the average bias intensities, ζ_i are the mirror control signals that generate a unit amount of Zernike mode *i*. Corrected images were obtained by sequentially correcting low order Zernike modes.

They initially demonstrated the system using fluorescent microbeads and found that correction decreased the axial length of the PSF by a factor of 1.8. Improved contrast and resolution were demonstrated in the X-Y and X-Z scans of fluorescently labeled mouse intestines [22]. A total of 28 scans at low laser power were required for correction

A recent confocal system developed by Tao et al. demonstrated the high speed correction of aberrations by direct measurement of the wavefront with a Shack-Hartmann Wavefront Sensor (SHWS) and correction with a deformable mirror containing 140 actuators. Fluorescent microbeads were fixed to the coverslip and slide to be used as the "guide star" for the Adaptive Optic system. A 240% increase in the signal intensity was observed while imaging mouse brain tissues at depths up to 100μm [38]. This system demonstrated that microbeads fixed beneath a sample could be used to measure wavefront aberrations in a confocal microscope.

Tao et al. extended their work and demonstrated that yellow fluorescent protein (YFP), a genetic mutant of GFP, could be used as the "guide star" for AO correction [39]. To improve the performance of the SHWS, out-of-focus light is blocked from entering the SHWS by a pair of irises placed in the sensors light path. They demonstrated correction using a YFP tagged neuron cell body beneath 70μm of brain tissue. The RMS errors of the wavefront were calculated before and after 10 iterations of correction and were found to be 0.35λ and 0.034 λ respectively. This corresponded to a Strehl ratio increase from 0.29 to 0.96 with correction. A careful comparison of microbead and YFP "guide stars" was performed by independently correcting the wavefront

aberrations with YFP and a microbead located 3μm from the fluorescent protein. The average RMS difference of 20 measurements was reported as 0.0272 λ [39].

Adaptive Optics and harmonic generation microscopy

Where confocal fluorescence relies on a physical pinhole to suppress out-of-focus light, harmonic generation microscopy relies on the non-linear optical response of the sample. In Second Harmonic Generation (SHG) Microscopy, frequency doubled light is generated by focusing a high powered laser onto a sample with a noncentrosymmetric molecular structure. Two photons from the laser can combined into a single photon of double the frequency through the nonlinear polarization of the material [40]. The harmonic photons can be separated easily from the illumination light and captured to form an image of the sample structure. Harmonic generation microscopy is typically performed on thick specimens, which can cause significant aberrations and degrade the performance of the microscope [41].

Jesacher et al. showed improved lived images of mouse embryos in an SHG and Third harmonic generation (THG) microscope. Total image intensity was used as the metric to optimize the mirror shape with Zernike modes. Zernike modes were iteratively induced into the system and initially optimized using a hill climbing algorithm. The precise aberration magnitude was then determined by peak detection through a parabolic fit. They demonstrated a signal increase of 54% in the captured signal at a depth of 45μm. This signal boost theoretically allows for a lower intensity illumination source to be used, which will extend the viability of live samples [30].

Adaptive Optics and widefield fluorescence microscopy

Adaptive Optics has been successfully implemented in wide-field fluorescence microscopy [14-16]. A two fold increase in signal intensity has been achieved using a deformable mirror placed in the emission path as the optical correction element. For widefield illumination, it is not necessary to place the correction element in the excitation path. In this system, correction of depth aberrations was simulated by calculating the phase correction based on the mathematical equations for the path length differences, resulting in improvement of the point-spread function. Figure 2.15 shows the result of the simulation. The authors demonstrated that with AO, a near perfect Strehl ratio can theoretically be maintained when focusing into a sample with an immersion medium with a mismatched index of refraction.

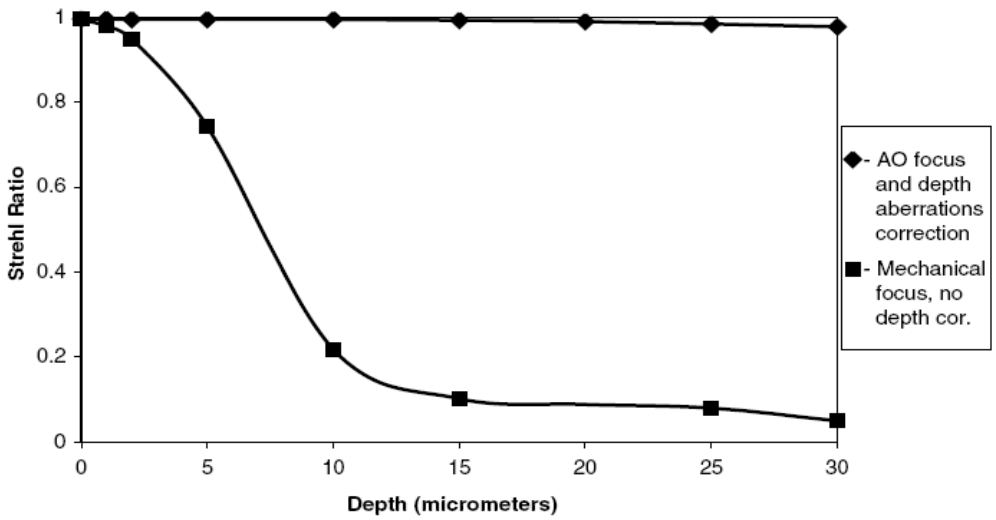

Figure 2.15: Strehl ratio comparison performed by Kam et al. [27]

An Adaptive Wide-Field Fluorescence system which directly measures wavefront aberrations with a Shack-Hartmann Sensor has shown improvement in the PSF of fluorescent microbeads injected into *Drosophila* embryos [16]. Fluorescent microbeads were used as artificial "guide stars" for the SHWFS. This system demonstrated an average two-fold increase in the Strehl ratio, with as much as a ten-fold improvement at a sample depth of 100µm. The improvement of the PSF and Strehl Ratio for a 1µm diameter microbead injected into the sample is shown in Figure 2.16.

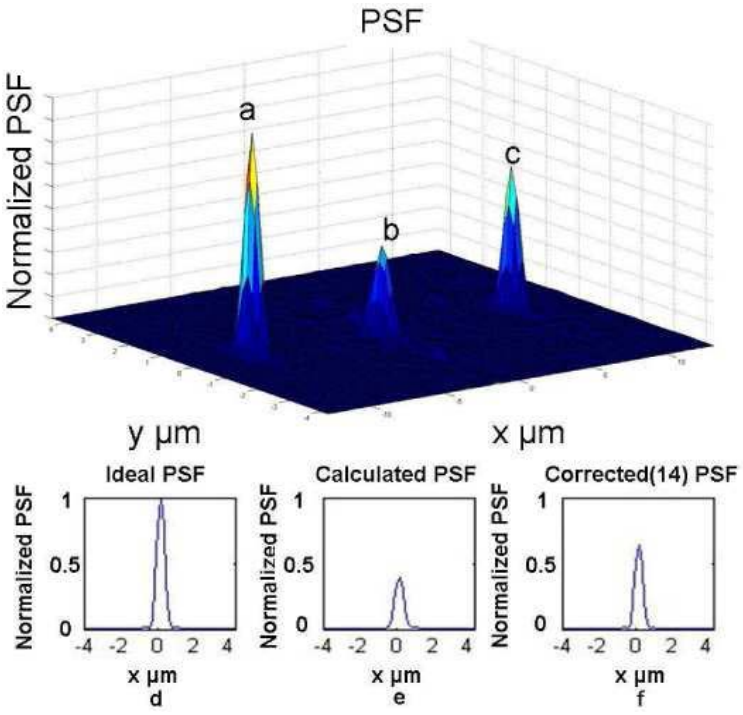

Figure 2.16: Results obtained by Azucena et al. showing improvement of the PSF and Strehl ratio a) Ideal PSF b) Uncorrected PSF c) Corrected PSF [16].

Vermeulen et al. demonstrated wavefront correction using "guide stars" which were spectrally independent from the sample fluorescence. The purpose of this study was to perform

wavefront correction without exciting the sample, and therefore without contributing to photobleaching. Injected red microbeads were used as the signal for a Shack-Hartman sensor and GFP tagged HeLa cells were then imaged after correction. An additional benefit to this setup is that the red microbeads do not appear in the final images. The calculated Strehl ratios before and after correction were .73 and .985 respectively [42].

Adaptive Optics for large aberrations

Booth et al. proposed focal spot radius as a correction metric in a sensorless Adaptive Optic system intended to correct large aberrations [21]. The authors minimized the spot radius of a focused laser as the AO metric as it has a distinct minimum and spherical symmetry for large aberrations. The intensity of a sample quickly drops off with aberration (as shown in the PSF simulation in Figure 2.4. For large magnitudes of multiple aberration modes, intensity based metrics may not be appropriate. Lukosz aberration modes, which are similar to Zernike modes but are more directly related to spot radius, were induced into the system by a spatial light modulator (SLM), which also acted as the correction element. A HeNe laser passes through the SLM and is focused onto a CCD camera. The authors demonstrated that the variation of the correction metric could be tuned by adjusting the spatial sensitivity of the detector [21].

Image based Adaptive Optics

Debarre et al. provided the theoretical background for using the low frequency content of the captured image could be used as a correction metric for a sensorless AO system [43]. Lukosz aberrations were induced through a deformable mirror. A parabolic relationship between the low

frequency content of the image and magnitude of aberration was found. The frequency content within a small annulus in Fourier space was optimized by applying bias aberrations for the aberration mode being removed and then finding the aberration magnitude corresponding to the metric peak. The magnitude of aberration corresponding to the maximum is then applied to the deformable mirror.

The authors demonstrated this method with an incoherent transmission microscope and holographic scatterer as the specimen. This ensured that all frequencies within the passband of the microscope would be present. Aberration consisting of the first eight Lukosz modes was induced into the system through the deformable mirror. With AO correction, the authors were able to achieve a Strehl ratio of 0.87 for single iteration of correction and 0.99 upon successive iterations [43].

Chapter 3: Structured Illumination Microscopy - background and literature review

Super-resolution microscopy background

As discussed previously, diffraction limits the resolution of conventional light microscopes to around 250 nm. Several techniques have been developed to breach the resolution limit of fluorescence microscopy, including Stimulated Emission Depletion Microscopy (STED), Photo-Activated Light Microscopy (PALM), Fluorescence Photoactivation Localization Microscopy (FPALM), Stochastic Optical Reconstruction Microscopy (STORM), and Structured Illumination Microscopy (SIM) [44-48]. STORM, FPALM and PALM localize individually activated fluorophores by finding the centroid of emission. This approach can provide resolutions of less than 25nm but requires many exposures to localize a sufficient number of fluorophores. STED microscopy increases resolution by inhibiting fluorescence in the outer portion of a confocal excitation spot and has achieved resolutions less than 50nm in biological samples. Linear SIM can reach a resolution of twice the diffraction limit in 2D and 3D fluorescence microscopy, superior to confocal imaging systems [48-50]. Although linear SIM

does not produce as high of a resolution as STORM, PALM, and STED, it can be performed at close to video rates over a large field of view [50-52]. In this Chapter, I review the underlying concepts behind SIM and review important applications and advances that have been reported in this fairly young field of research.

Basic principles behind SIM

The operation of a structured illumination microscope is based on the well-known Moiré effect. The Moiré effect is the phenomenon where a lower frequency beat pattern is created by the interference of two fine patterns. An example of the Moiré effect is shown in Figure 3.1.

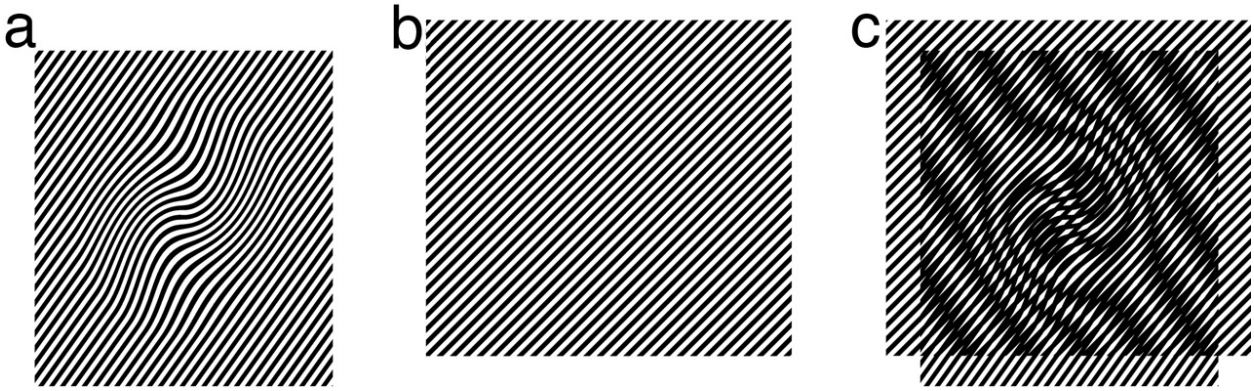

Figure 3.1: This interference of the patterns in (a) and (b) create a lower frequency beat pattern in (c) [53].

In SIM, the sample is illuminated with a striped pattern. The captured images include information outside the 2NA/lambda passband of the microscope as a result of the interference of the pattern and the fluorescence structure of the sample. These captured images contain the beat

pattern that is the result of the Moiré effect, which contains higher frequency information. Knowledge of the illumination pattern can be used to extract the unknown sample structure from the captured images. Numerous variations of SIM have been developed, here we review the basic ideas behind super-resolution SIM by following the formulation proposed by Gustafsson et al. [50].

SIM achieves sub-diffraction levels of resolution by exploiting the fact that the information that is ideally obtained from an imaging system is the fluorophore distribution within the sample, not the fluorescent emission. The fluorophore emission, E(r), is the product of the sample fluorophore distribution, S(r), and the illumination structure, I(r), as given by

$$E(r) = S(r)I(\mathrm{r}). \qquad \textbf{Eq. (3.1)}$$

Multiplication in the spatial domain is equivalent to convolution in the Fourier domain. Equation 3.1 can now be written as

$$\tilde{E}(k) = \tilde{S}(k) \otimes \tilde{I}(k) \qquad \textbf{Eq. (3.2)}$$

where *k* is the frequency space coordinate. Equation 3.2 represents the emitted fluorescence in frequency space. Combining Equations 3.1, and 2.10, we can now define the observed image as

$$D(r) = (S(r)I(r) \otimes H(r)) \qquad \textbf{Eq. (3.3)}$$

It is important to note that $\tilde{E}$ contains information about the sample structure ($\tilde{S}$) from outside the region of support of the OTF. This is the main idea behind SIM, the illumination pattern moves high frequency information into the passband of the system through frequency mixing ($S(r)I(r)$). The low frequency beat pattern resulting from the frequency mixing of the illumination structure and flourophore distribution contains high frequency information, or

information from outside the region of support of the OTF, but is encoded in the observed images. The Fourier transform of Equation 3.3 is given by

$$\widetilde{D} = (\tilde{S} \otimes \tilde{I})\widetilde{H} \qquad \textbf{Eq. (3.4)}$$

The super-resolution details can only be extracted if the illumination pattern has a spatially varying structure. Any number of illumination patterns could be used in theory. Extracting the encoded super-resolution information can be simplified if certain conditions are met by the illumination structure. Equation 3.5 gives the general form for the illumination structure.

$$I(r_{xy}, z) = \sum_m I_m(r_{xy}) J_m(z) \qquad \textbf{Eq. (3.5)}$$

The illumination structure must be the sum of separable axial and lateral components. The second condition is that the lateral function I_m should consist only of a single frequency. Finally, the illumination pattern should be fixed in relation to the focal plane of the microscope. This final condition ensures that the PSF (*H)* and the axial illumination function (*J*) share the same coordinates. The captured image and its Fourier transform may now be written as

$$D(r) = \sum_m [(HJ_m) \otimes (SI_m)](r) \qquad \textbf{Eq. (3.6)}$$

and

$$\widetilde{D}(k) = \sum_m \widetilde{H} \otimes \tilde{J}_m[\tilde{S}(k) \otimes \tilde{I}_m(k)] \qquad \textbf{Eq. (3.7)}$$

As mentioned previously, the spatial variation of the illumination pattern must only contain a single frequency. A simple harmonic equation can be defined as

$$I_m(r_{xy}) = e^{i(2\pi \boldsymbol{p}_m \cdot \boldsymbol{r}_{xy} + \phi_m)} \qquad \textbf{Eq. (3.8)}$$

where $\boldsymbol{p}_m$ is the frequency of the illumination pattern and ϕ_{m} is the initial phase for fundamental harmonic m. As the illumination pattern consists of only one frequency, it will be represented by a single peak in frequency space.

$$\tilde{I}_m(\boldsymbol{k}_{xy}) = \delta(\boldsymbol{k}_{xy} - \boldsymbol{p}_m)e^{i\Phi_m} \qquad \textbf{Eq. (3.9)}$$

Updating equation 3.7 gives

$$\widetilde{D}(k) = \sum_m \widetilde{D}_m(k) = \sum_m(\widetilde{H} \otimes \tilde{J}_m)[e^{i\Phi_m}\tilde{S}(k - p_m)]. \qquad \textbf{Eq. (3.10)}$$

The term $\widetilde{H} \otimes \tilde{J}_m$ shows that each component (m) of the illumination pattern is its own optical transfer function given by the convolution of the OTF ($\widetilde{H}$) of the optical system with the m^{th} harmonic component axial illumination pattern. This OTF is applied to the p_m shifted object information in frequency space. As shown in the above equation, the captured image for SIM is the sum of several components. A single image does not contain enough information to fully separate the components. Multiple images must be acquired with shifted illumination phases ($\delta\phi_m$) in order to obtain enough information to reconstruct the object (S). Equation 3.10 becomes

$$\widetilde{D}(k) = \sum_m \widetilde{H} \otimes \tilde{J}_m[e^{i(\Phi_{m0}+\delta\Phi_m)}\tilde{S}(k - p_m)] \qquad \textbf{Eq. (3.11)}$$

where ϕ_{m0} is the initial phase of harmonic m.

The object structure can be determined through solving a NxN matrix if the number of images acquired with N different phases is equivalent to the number of harmonic components. To avoid singular matrices, N images are captured with the illumination structure shifted by $2\pi/\mathrm{N}$ for each image. Further simplification of Equation 3.11 can be accomplished by making use of the symmetry property of the Fourier Transform. The real-valued illumination , I , will be

conjugate symmetric in the Fourier domain, ($\tilde{I}^*(k) = \tilde{I}(-k)$). If the lateral spatial frequencies are harmonics of a periodic pattern, then the spatial frequencies will be multiples of the fundamental frequency p_m. That is, $p_m = mp$. If the phase shifts of the illumination pattern $\delta\phi_m$ are evenly spaced, then they can be written as $\delta\phi_m = m\,\delta\phi$. If the illumination patterns have reflection symmetry then the starting phases and total phase can similarly be written in terms of integer multiples ($\phi_{m0} = m\phi_0$ and $\phi_m = m\phi$). Finally, the observed data can be written as

$$\widetilde{D}(k) = \sum_m \widetilde{H} \otimes \tilde{J}_m[e^{im\phi}\tilde{S}(k - mp)]. \qquad \textbf{Eq. (3.12)}$$

The captured image contains super-resolution data through the axially extended OTF ($\widetilde{H} \otimes \tilde{J}_m$) and the information that is moved inside the region of support of the OTF through the translation *mp*. Once the frequency components are separated, they can be manually restored to their proper positions and then recombined to produce the super-resolution image. Typically, the data is reassembled with a generalized Wiener filter defined as

$$\widetilde{D}_{SR-SIM}(k) = \frac{\sum_{d,m}\tilde{H}_m(k+mp_d)\tilde{S}_{d,m}(k+mp_d)}{\sum_{d,m}|\tilde{H}_m(k+mp_d|^2+w^2}\,A(k) \qquad \textbf{Eq. (3.13)}$$

where m represents the interference modes of the illumination pattern, d represents the pattern orientation, *A* is an apodization function, and *w* is the Wiener parameter. The Wiener parameter adjusts the bandwidth of the OTF, allowing the suppression of the low signal to noise regions at its edges. The frequency content of the final reconstructed image will drop off suddenly at the edges of the enhanced region of support, causing ringing artifacts in the SIM image. An apodization function (*A*) can be used to smooth these sharp edges and reduce ringing artifacts.

As shown in Equation 3.13, the extent to which the region of support is extended in SIM is dependent on the illumination pattern frequency. However, the illumination pattern is limited

by diffraction, so the maximum spatial frequency of the pattern is equivalent to the resolution limit of the microscope. This limits the maximum resolution enhancement obtainable through structured illumination to 2x [50].

Super-resolution 2D SIM (SR-SIM)

Gustafsson et al. and Heintzmann et al. can be credited with the development and implementation of the super-resolution Structured Illumination Microscope (SR-SIM) [3, 49]. The system implemented by Gustafsson et al. obtained a 2x resolution of a conventional fluorescence microscope with a diffraction limited illumination pattern created by a line-patterned phase grating [3]. The phase of the illumination laser was scrambled by a mechanical shaker and the light polarized to be parallel to the direction of the phase grating. A physical mask placed parallel to the back pupil plane was used to block all but the ±1 diffraction orders of the illumination pattern from reaching the sample. The authors chose a near diffraction limited pattern spacing to produce the highest lateral resolution enhancement possible.

With the illumination conditions described, Equation 3.12 is furthered simplified by noting that the axial illumination structure does not change (J_m =1) and taking into account the fact that the frequency content of the illumination pattern contains only three Fourier components (0,±1), due to the optical mask. The frequency content of the observed image can now be written as

$$\widetilde{D_\iota}(k) = 0.5\left(\tilde{S}(k) + 0.5e^{i\Phi_i}\tilde{S}(k+px) + 0.5e^{-i\phi_i}\tilde{S}(k-px)\right)\widetilde{H}(k), \qquad \textbf{Eq. (3.14)}$$

where ϕ_i is phase difference between the zero order and shifted frequency components. If three images are acquired at evenly spaced illumination pattern phases, the high-resolution details of the fluorophore structure can be extracted. Equation 3.14 shows that the resulting images will have three non-zero Fourier components and that the value at point k in frequency space depends only on three components of the sample structure ($\tilde{S}(k), \tilde{S}(k+px), and\ \tilde{S}(k-px)$). The first term represents the widefield image information. The second and third terms represent information in frequency space that has been shifted into the region of support of the OTF. ϕ_i in Equation 3.14 represents the phase difference between the $\tilde{S}(k)$ and $\tilde{S}(k+px)$ terns. The frequency components can be separated by a simple linear equation (Equation 3.15).

$$\begin{bmatrix} S_0 \\ S_p \\ S_{-p} \end{bmatrix} = \frac{1}{3}\begin{bmatrix} 1 & 1 & 1 \\ e^{i\phi_1} & e^{i\phi_2} & e^{i\phi_3} \\ e^{-i\phi_1} & e^{-i\phi_2} & e^{-i\phi_3} \end{bmatrix}\begin{bmatrix} D_1 \\ D_2 \\ D_3 \end{bmatrix} \qquad \textbf{Eq. (3.15)}$$

As frequency of the illumination pattern (p) is known, the super resolution information can be manually restored to its proper position in frequency space. It is important to note that S_0, S_p, and S_{-p} are not the flourophore structure itself, because the PSF must still be deconvolved. Also, Separating the components with Equation 3.15 does not restore the extended resolution details to their proper positions, it only separates the components which exist in the same frequency range as the S_0 in the captured image. The final reconstructed image is obtained through the Weiner filter given by Equation 3.13.

The resolution will only be enhanced along the direction of the illumination pattern. If the illumination pattern is rotated, an isotropic resolution enhancement can be achieved. The idea behind 2D SR-SIM is summarized in Figure 3.2. Figure 3.2a shows the creation of a beat pattern by interference with the illumination pattern. Figure 3.2b displays the Fourier

components of the illumination pattern (dots) and the OTF region of support of the microscope (dashed lines). As shown, the illumination pattern frequency chosen for this study was near the edge of the OTF region of support so that the maximum resolution enhancement can be obtained. As the illumination pattern is subject to diffraction, the maximum resolution enhancement that can be practically achieved is twice the conventional resolution. Figures 4.1b and c show the extended OTF with one (b) and three (c) pattern orientations. At each pattern orientation a total of 3 images are acquired at pattern phases 0, $2\pi/3$, and $4\pi/3$. A total of 9 images are used in this technique to produce an isotropic enhancement of the resolution.

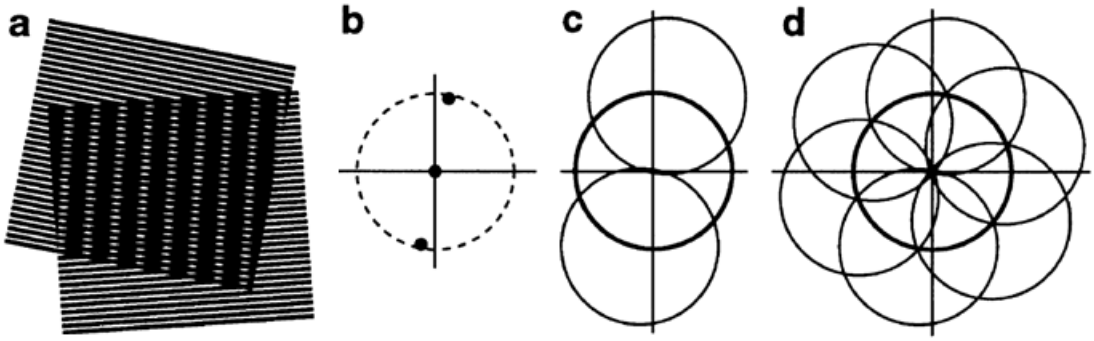

Figure 3.2: (a) A beat pattern is created by illuminating fluorophore distrubtion with structured light. (b) Region of support for a conventional system (dashed lines) with the Fourier components of an illumination pattern near the resolution limit (dots). The OTF support region for a single illumination pattern with a single (c) and three pattern orientations (d) [3].

The authors compared SR-SIM to conventional confocal microscopy. The 2D SIM method proved to produce images with greater lateral resolution than confocal microscopy. The FWHM of 120nm microbeads was measured to be 130nm with SR-SIM and 210nm with

conventional confocal microscopy. SR-SIM was also demonstrated on actin filaments at the edge of HeLa cells and produced double the resolution of the widefield images [48].

Optical Sectioning SIM

In confocal microscopy, the "missing cone" problem is solved by physically blocking out-of-focus light with a pinhole. The pinhole gives an effective PSF which is the square of the conventional PSF, resulting in an enhanced resolution. Using a pinhole to block out-of-focus light necessitates raster scanning the sample in order to obtain the image. Also, the resolution enhancement depends upon the pinhole diameter, where a very small pinhole gives the highest improvement to the resolution. A small pinhole also results in a loss in signal, which means that the sample must be illuminated with a relatively high-powered laser to produce a quality image. Exposing a biological sample to a high-powered illumination source results in rapid photobleaching and ablation of the sample.

Theoretically, confocal microscopy can produce the same OTF support as SIM if a very small pinhole is used. Somekh et al. performed a detailed comparison of 2D SR-SIM to confocal microscopy based on the number of photons required to distinguish two point objects [54]. They found that SIM needed fewer photons over all separation distances tested to distinguish between the two objects. The optimal balance between resolution enhancement and photon collection of the confocal microscope was acquired with a $0.25\frac{\lambda}{NA}$ diameter pinhole.

Although 2D SR-SIM more efficiently enhances the resolution compared to a confocal microscope, it still suffers from the same "missing cone" problem as a conventional microscope. As previously discussed, the 3D OTF of a light microscope is torus shaped (see Figure 2.4). The

3D representation of Figure 4.1b is shown as Figure 4.2. As shown, the OTF at the 0 frequency component, drops quickly with defocus and is not filled in by the shifted components.

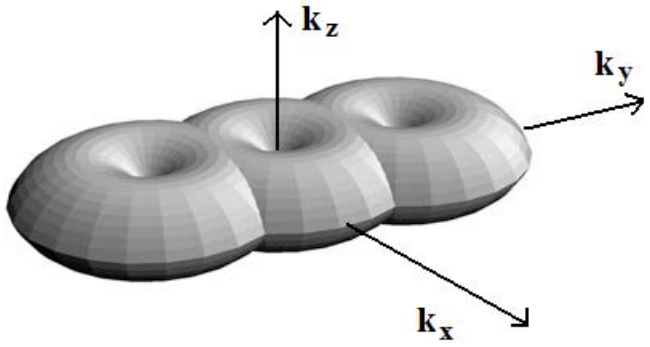

Figure 3.3: Shifted 3D OTF using 2D SIM [50].

Neil et al. proposed a simple and easily implementable method for producing optically sectioned imaged with Structured Illumination [55]. Similar to 2D super-resolution SIM, a grid pattern is projected onto the image plane of the microscope. Three images (D_0, D_1, D_2) are acquired at relative spatial phases 0, 2π/3, and 4π/3 of the illumination pattern. A coarser illumination pattern that is equivalent to half the OTF region of support (NA/λ) is used instead of the nearly diffraction limited pattern in super-resolution SIM. The 2D OTF attenuates most rapidly at NA/λ. By shifting the OTF support using a λ/NA wavelength grating, out of focus light near k~0 is attenuated rather than high frequencies at k~NA/λ. Neil et al. showed that an optically sectioned image can be simply obtained by

$$D_{RMS-SI} = [(D_1 - D_2)^2 + (D_1 - D_3)^2 + (D_2 - D_3)^2]^{1/2} \quad \textbf{Eq. (3.16)}$$

which is equivalent to the square law detection algorithm. As the illumination grid goes out of focus, there is no contrast in the illumination pattern and thus little difference between the phase shifted pattern images for out of focus fluorophores, thus their contributions to the final image can be removed by simple subtraction. Karadaglic and Wilson [56] showed that:

$$D_p(x,y) = |S_r(x,y)| \qquad \textbf{Eq. (3.17)}$$

where:

$$S_r(x,y) = \exp(-j2\pi px)\mathbb{F}^{-1}\{\tilde{S}(k_x,k_y)\widetilde{H}(k_x+p,k_y)\} \qquad \textbf{Eq. (3.18)}$$

Equation 4.3 essentially removes the widefield contribution of the observed images under structured illumination as the shifted frequency information drops off quickly with defocus. This method requires no knowledge of the illumination pattern phase or its exact frequency. The disadvantage is that only the shifted frequency components are used in the final image, which represents a loss of information. Neil et al. demonstrated widefield optically sectioned images of pollen grains that were similar to results obtained with a confocal microscope.

Heintzmann and Benedetti proposed another method for obtaining optically section images in SIM. Their method is based on the assumption that the intensity of a pixel will be at a maximum when it is in focus [57]. Once again, the sample is illuminated by a pattern, and the pattern is shifted so that the entire sample is covered. For each position (x,y) in the image, the image with the lowest intensity value, which mainly consist of out-of-focus light and background, is subtracted from the image with the highest intensity values (in-focus) for each set of structured illumination images. The optically sectionined image is given by

$$D_{Max-Min} = max_i\{D_i\} - min_i\{D_i\}. \qquad \textbf{Eq. (3.19)}$$

Any illumination pattern can be used with this technique, as long as the pattern varies between images. A variation of this idea was used by Mertz et al. in their development of HiLo microscopy[58]. In HiLo microscopy, the sample is illuminated by a laser generated random speckle pattern. When in-focus fluorophores are illuminated in this manner, they exhibit high contrast. By comparing the speckle illumination images to widefield images, out-of-focus contributions can be removed and an optically sectioned image can be obtained [58]. Heintzmann and Bemedetti chose a two dimensional distribution of points as the illumination pattern [57]. As with the Neil method, not all information acquired is used in the final image reconstruction, which means that the SNR of the final image is not optimal. If the object being imaged is small, then it will not fluoresce during the majority of image acquisition. This leads to a skewing of the histogram, which can be exploited by Equation 3.20 to produce an image that is optically sectioned [57].

$$D_{Super} = max_i\{D_i\} - min_i\{D_i\} - 2avg_i\{D_i\} \qquad \textbf{Eq. (3.20)}$$

The method described by Neil et al. [55] involves removing the widefield information from the observed data set and the method described by Heintzmann and Benedetti [57] involves taking the maximum or minimum of a set of images. Both methods are non-linear. The relative intensity of objects of varying shape are skewed by these reconstruction methods. Their non-linearity also infers that a true OTF does not exist for these reconstruction methods.

Karadaglic and Wilson proposed a simplified linear 2D reconstruction method which produces optically sectioned images at enhanced resolution [59]. A coarse illumination pattern (as in the Neil method [55]) is used and frequency components of the observed image are separated (as per Gustafsson [48]). The zero-order frequency component, whose intensity does

not attenuate with defocus, is omitted and the shifted frequency components are recombined according to Equation 4.8 [59]. This equation represents a single illumination pattern which varies along the x-direction.

$$\widetilde{D}_{2D-SI}(k_x, k_y) = \tilde{S}_{2D,p}(k_x + p, k_y) + \tilde{S}_{2D,-p}(k_x - p, k_y) \qquad \textbf{Eq. (3.21)}$$

The subscript 2D is included to emphasize that this approach operates on 2D image slices independently and therefore the OTF is also two-dimensional. Like the Neil and Heintzmann methods, detailed knowledge of the illumination pattern frequency and its phase are not required. The authors demonstrated their results using pollen grains. As shown in Figure 4.3, out-of-focus light strongly affects the widefield image (a) and is suppressed in the optically sectioned image (b) [59]. Because the zero ordered frequency content of the observed images are omitted, the lower order spatial frequency components will be weaker and noisier, strongly degrading the image quality.

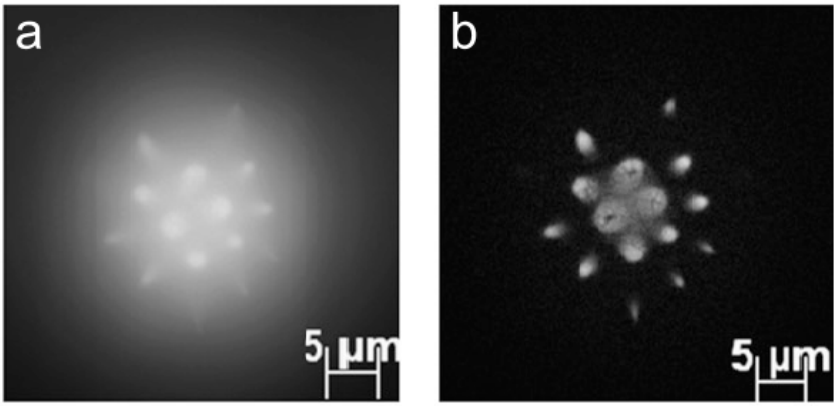

Figure 3.4: Results of the Karadaglic 2D-SI method on a pollen grain (b) compared to the widefield image (a) [56].

3D SR-SIM

Gustaffson et al. implemented a SIM system capable of producing double the resolution of a conventional microscope in both the axial and lateral dimensions [50]. Similar to the two dimensional version, an illumination pattern frequency near the diffraction limit of the scope is used. As discussed in the previous section, super -resolution 2D SIM utilizes only the ±1 modes of the illumination beam, which limits the frequency components of the illumination beam at the sample. The results will show the same enhanced lateral resolution, but suffer from the missing cone problem and thus poor axial resolution. Various methods were proposed to produce optically sectioned images, but do not fully take advantage of the resolution enhancements that are obtainable [55, 57-59].

A three-dimensional structured is created in the excitation by interfering the ±1 orders with the 0 order beam. The interference of three illumination beams produces a 3D illumination structure. The illumination structure can be represented as three wave vectors (Figure 3.5a). The autocorrelation of the excitation beam wave vectors gives the seven frequency components of the illumination structure. (Figure 3.5b).

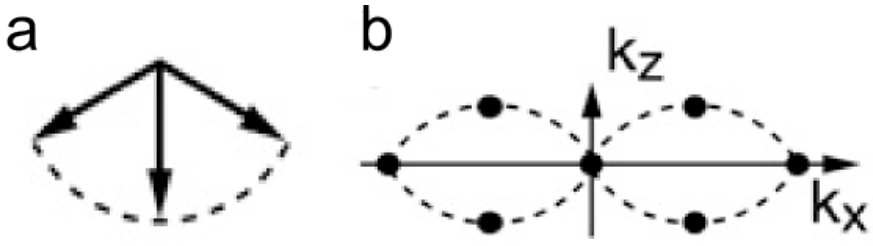

Figure 3.5: (a) The illumination wave vectors for 3D SR-SIM and (b) frequency components of the incoherent illumination structure [50].

The illumination intensity is real ($\tilde{I}^*(k) = \tilde{I}(-k)$, where * represents the complex conjugate operator), so there are only five independent Fourier components of the 3D illumination light. The shifted high-resolution details of the sample structure can be separated using a 5x5 set of linear equations similar to Equation 3.15. If at least five phase shifted images are obtained and if the pattern frequency and its initial phase are known, the extended resolution details can be restored to their proper positions. With a single pattern orientation, an OTF that doubles the resolution in pattern direction as well as the axial direction (Figure 3.6) is obtained. As shown in the figure, the missing cone is filled and the OTF region of support has been extended along the axial direction, k_z.

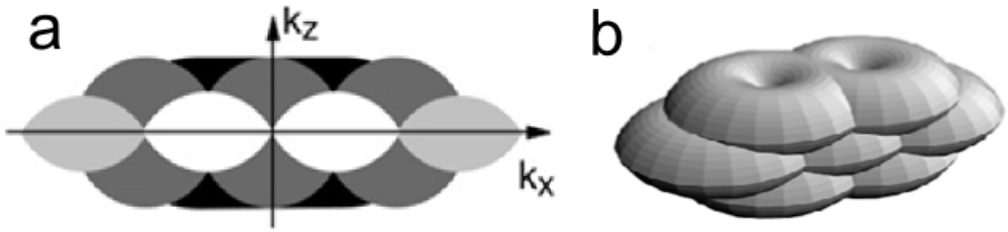

Figure 3.6: The OTF obtained under 3D SIM with a single pattern orientation shown in two (a) and three (b) dimensions [50].

Once again, the authors achieve an isotropic resolution enhancement by using three rotated orientation patterns. For each image slice of the three-dimensional image stack obtained, 15 images were acquired (5 phases of the illumination pattern for each of 3 angles). The super-resolution image stack is obtained by restoring the frequency components of the

sample structure to their proper positions and combining them through a generalized Weiner filter as defined by Equation 3.13. A triangular apodization function was used to reduce artifacts in the reconstructed images.

The authors compared conventional widefield microscopy to 3D SIM using both fluorescent microbeads as well as biological specimens. Widefield images were generated by combining the phase shifted SIM images of a single pattern orientation. To test the resolution of the system, the axial and lateral Full-Width-Half-Maximums (FWHM) of 100 microbeads with nominal diameters of 120nm were measured. They found a mean lateral FWHM of 103.9nm and an axial FWHM of 279.5nm.

Figure 3.7 compares the widefield and SI images of microtubules in HeLa cells. The maximum intensity projections obtained from conventional widefield illumination and SIM are shown as (a) and (b) respectively. As shown, the out-of-focus light is suppressed in the Structured Illumination. The inset sections show microtubules a distance of 125nm apart. Without SIM, they cannot be individually resolved. [50].

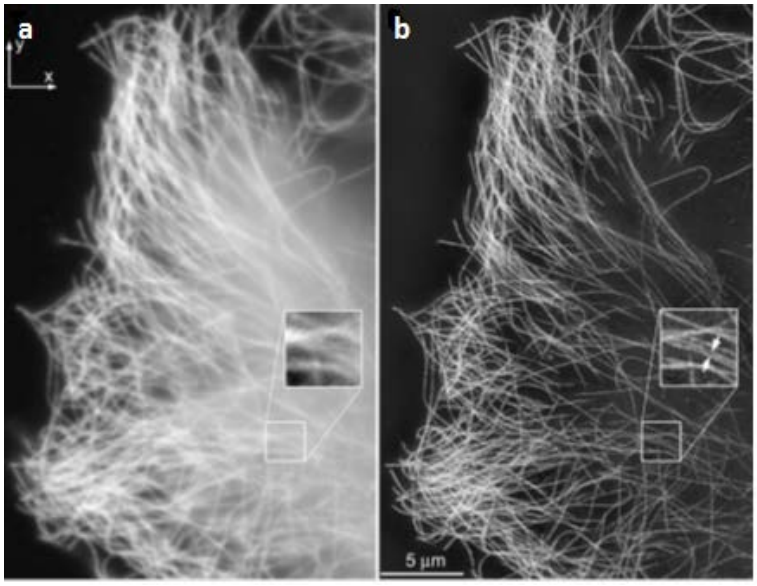

Figure 3.7: Comparison of conventional and 3D-SIM images of microtubules [50].

SIM and total internal reflection microscopy

Total internal reflection fluorescence microscopy (TIRF) is an important widefield method for selectively illuminating molecules attached to the coverslip surface. According to Snells law, when light travels from a medium with a relatively high index of refraction to one of lower index, the refracted ray is bent away from the normal to the interface. If the incident angle is greater than the critical angle,

$$\theta_{crit} = sin^{-1}\frac{n_2}{n_1}, \qquad \textbf{Eq. (3.22)}$$

total internal reflection occurs. The result is in an evanescent wave in the low-index material, which is an exponentially decaying field created at the intersection of the materials. TIRF microscopes can achieve axial resolutions of less than 100nm, and are important tools single

molecule studies. Despite the axial enhancements, the lateral resolution of TIRF is still limited by diffraction [60].

SR-SIM TIRF

Fiolka et al. demonstrated the concept of a SR-SIM TIRF system by producing 91nm resolution images of 50nm fluorescent microbeads [61]. An SLM was used to create two collimated beams which interfere at the sample to create the illumination pattern. Two interference patterns normal to each other were used for SIM. A half wave plate was used to maintain the polarization of the illumination light relative to the pattern orientation. The authors compared TIRF and SIM TIRF setups at illumination beam incident angles of 63° for both modes. The addition of the SIM system doubled the obtainable resolution [61].

Live SR-SIM TIRF

Kner et al. demonstrated a SR-SIM TIRF system capable of 11 Hz frame rates [62]. As per Gustafsson [ref], nine total images were acquired at three pattern orientations and three evenly spaced phases. Instead of translating a physical grid, patterns were generated by writing data to the SLM, providing a considerable speed boost to the process. The system was demonstrated by imaging α-tubulin fused to enhanced GFP. Over 156 measurements, microtubules had an average FWHM of 112 ± 12nm for the SIM reconstructions compared to the average conventional TIRF FWHM of 275 ± 21nm. The capability of the system to image live samples was tested using kinesin-73-EGFP in S2 cells, whose typical speeds average around

$780\frac{nm}{s}$ [63]. Although the signal-to-noise ratio of the sample decreased during video acquisition, the resolution of the system remained around 110nm throughout [62].

Live SR-SIM

Shao et al. demonstrated that 3D SR-SIM was a viable tool for imaging live samples [51]. As per Gustafsson [50], the system creates a three dimensional illumination pattern. To reconstruct the 3D image, 5 images at unique phases must be acquired for each of the 3 pattern orientations, resulting in 15 total images per axial slice. The authors noted that using a transmission phase grating placed in the illumination path to create the illumination pattern was too slow for imaging live cells, as mechanically rotating and shifting the grating limited the speed of the system, requiring around 1s and 10ms respectively. By generating the patterns with an SLM as per Kner et al. [62], the acquisition time becomes limited by the camera. The authors proved 3D SR-SIM to be a viable tool for live cell imaging with multiple biological samples. Over 50 times points of a bundle of EGFP tagged microtubules with EGFP were captured at 5 seconds per SIM volume. The system produced an axial resolution of 360nm and a lateral resolution of 120nm [51].

Two color video 3D SR-SIM

Fiolka et al. extended using SIM for imaging live cells to two colors [52]. The illumination pattern generating SLM allows the wavelengths of the separate illumination wavelengths to be compensated for in the pattern generation. The illumination lasers have wavelengths of 488nm and 561nm and are used to excite mitochondria tagged with MitoTracker

Green and microtubules labeled with mCherry (Clontech) repectively. A single time point consisting of two 3D SR-SIM volumes can be acquired in 8 seconds with their system. They noted that the limiting factor in the acquisition speed was the camera exposure time, which could be improved with the newest technology [52].

Non-linear 2D SR-SIM

The SR-SIM systems presented to this point are capable of producing a 2x increase in the conventional resolution by utilizing a diffraction limited illumination pattern. Decreasing the wavelength of the illumination pattern below the resolution limit will not further enhance the resolution limit as the pattern will be filtered out by the microscope. Gustafsson et al. proposed a nonlinear form of SIM with theoretically unlimited resolution [53]. The authors saturated fluorphores to their excited states, resulting in a nonlinear relationship between the illumination intensity and fluorescence emission. Under saturation conditions, the illumination pattern is not sinusoidal and therefore its frequency spectrum contains harmonics. Heintzmann et al. first proposed the idea of using saturated fluorophores to extend microscope resolution [64]. When a fluorophore is excited, it decays to its ground state after a short time. During this time, it cannot be excited by other incoming photons and thus has a non-linear response to incoming light. If a sample is illuminated by structured light with a peak above the saturation threshold, the fluorophore emission rate contains harmonics of the illumination pattern.

The high frequency of these illumination harmonics allows the OTF to be extended to a theoretically unlimited resolution. The idea behind non-linear SR-SIM is summarized in Figure 3.8 [53]. With a suitable number of images, the high frequency information can be restored to

its proper position and resolution beyond linear SIM can be obtained. In practice, the resolution of their system depends on photobleaching, which in turn determines the signal-to-noise ratio. The authors initially demonstrated their system by producing images of fluorescent microbeads at a resolution less than 50nm [53]. The illumination laser produced 3.6μJ pulses with 640ps duration at a rate of 6kHz. Although a high resolution can be achieved with this technique, the intense illumination needed to saturate fluorophores to induce a non-linear response is inappropriate for biological samples, as they will photobleach.

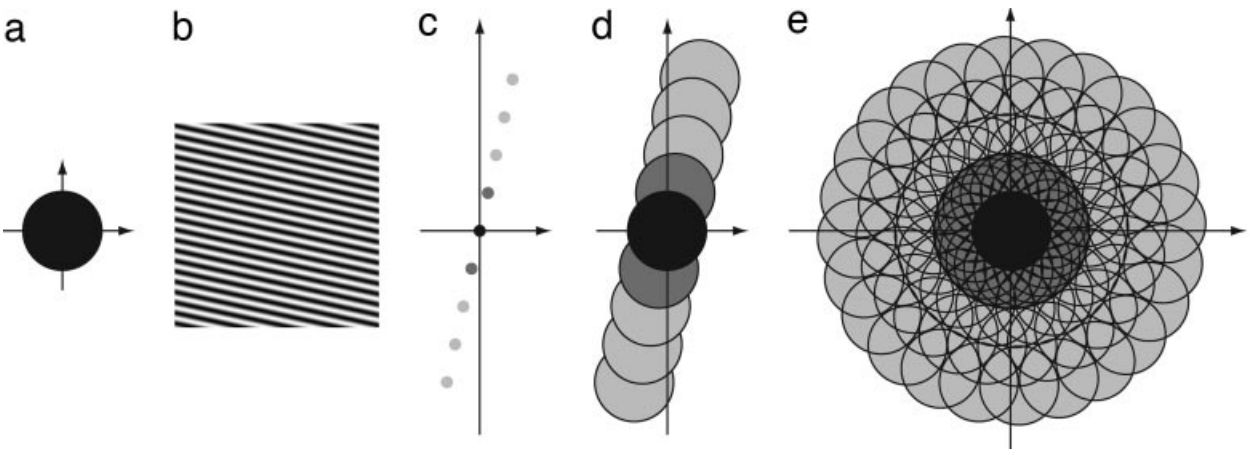

Figure 3.8: Enhanced resolution through non-linear SI. (a) The region of support for a conventional light microscope. (b) Illumination pattern example. (c)Frequency components generated by SI illumination. The dark circle represents average intensity (widefield information), the dark grey circles represent frequency shifts in linear SI, the light grey circles represent the first three harmonics (theoretically there are infinite harmonics) under saturation conditions. (d) The regions of support for the frequency components .(e) Theoretical OTF region of support after rotating the illumination pattern [53].

Rego et al. recently demonstrated non-linear SR-SIM using the photo-switchable fluorescent protein Dronpa [65]. Their Total Internal Reflection Fluorescence (TIRF) SIM

system is capable of 50nm lateral resolution by capturing 63 total images (seven phases for nine orientations). The illumination intensity required to produce non-linear effects in Dropna is six orders of magnitude lower than the initially reported non-linear SIM system [53]. The concept is the same, a non-linear relationship between the illumination intensity and emission produces harmonics of the illumination pattern. Most importantly, the authors demonstrated their system on biological samples. Figure 3.9 below compares non-linear and linear TIRF SIM as well as and conventional and filtered TIRF images of Dronpa-coated microtubules. As reported by the authors, the non-linear SIM image with 2 higher order harmonics resulted in microtubule cross-section of 42nm. In comparison, the conventional, filtered, and linear SIM images of the microtubule cross-sections were measured to be 232nm, 166nm, and 84nm respectively.

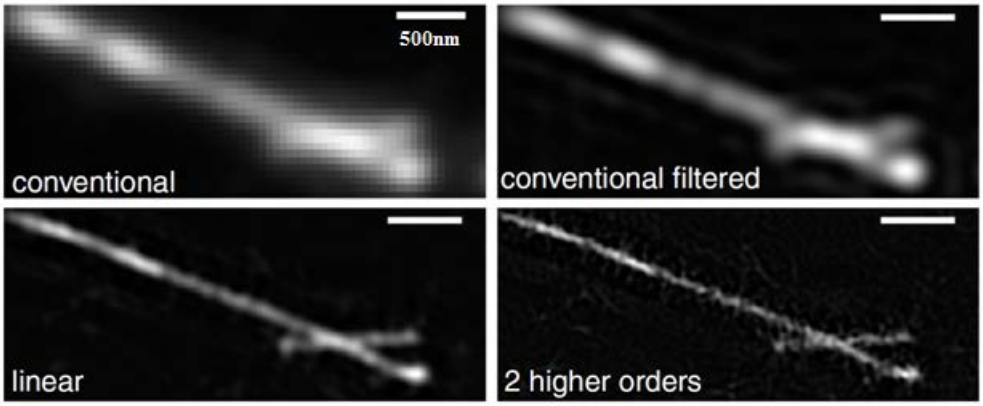

Figure 3.9: Microtubule stained with Dronpa imaged with conventional TIRF, conventional filtered TIRF, linear SIM, non-linear SIM with two higher order harmonics.

AO and optical sectioning SIM

The first reported combination of Adaptive Optics and SIM was published by Debarre et al. [66]. A sensorless AO correction scheme was used in conjunction with the optical sectioning SIM technique described by Neil et al. [55]. The authors found that the final image quality of a SIM is dependent on the fidelity of the illumination pattern on the sample. Aberrations due to optical imperfections, alignment errors, and the complex sample being imaged adversely affect the illumination pattern and its frequency and therefore reduce the quality of the reconstructed SIM image. The authors found that aberrations could be separated into two groups where SIM is concerned: those that affect the illumination pattern, and those that do not. Using this knowledge, they developed a unique set of aberrations modes for modal AO correction based on Zernike Polynomials with the intent of optimizing the pattern contrast. Using a coarse grid for the illumination pattern, the authors were able to demonstrate improved contrast and resolution through 10μm of mouse intestine tissue. In testing their system with mouse intestine tissue and pollen grain samples, the authors found that aberrations mostly consisted of astigmatism, coma, and spherical modes [66].

CHAPTER 4 AO-SIM SYSTEM DESCRIPTION

In the previous chapters, I introduced the theory behind Adaptive Optics (AO) and structured illumination microscopy (SIM), and presented recent advances in their respective fields. In this chapter, I will describe our optical system designed to combine AO and SIM. After introducing the system, I will describe removing aberrations inherent in the components, and specific steps taken to minimize errors due to the optical components.

A schematic of the AO-SI system is shown in Figure 4.1. We use an Olympus IX71 Inverted microscope with a Prior Proscan XY Stage (H117P2IX) and a Prior 200 micron travel NanoScan Z stage. The microscope objective is a 60x Plan Apo N oil immersion objective (NA 1.4), and the Olympus tube lens has a focal length of 180mm. The light exits the IX71 through the left side port where the back pupil plane is reimaged by a 300mm lens (OptoSigma 026-1250) onto a Imagine Optic Mirao 52-e deformable mirror (DM). The mirror consists of 52 electromagnetic actuators attached to a flexible reflective surface 15mm in diameter. The diameter of the collected light at the DM is given by

$$\emptyset_{DM} = \frac{2NAf_1 f_{obj}}{f_{tube}} \qquad \textbf{Eq. (4.1)}$$

where $\frac{f_{tube}}{f_{obj}}$ = 60. Given the 15mm diameter of the DM, the system NA of the system is limited to 1.285. The image plane at the exit port is re-imaged onto an Andor EMCCD camera with an additional magnification factor of 3 (f5/f3). The pixel size in sample space is given by

$$pixel\ size\ in\ sample\ space = Camera\ pixel\ size\ (\frac{f_{obj}}{f_{tube}})(\frac{f_1}{f_2})(\frac{f_3}{f_5}) \qquad \textbf{Eq. (4.2)}$$

where the total system magnification $(\frac{f_{tube}}{f_{obj}} * \frac{f_5}{f_3})$ is 180 and the pixel size for the Andor camera is 16μm. The result is an 89nm pixel width in sample space. For the 512x512 CCD chip, the total field of view captured is 45μm x 45μm.

The excitation source for SIM is a 488nm laser (Newport Cyan 488) which is coupled into a 100μm core diameter fiber. The fiber is shaken using a fiber shaker as described in [51] to remove speckle, creating a partially coherent source [50]. The structured illumination is created with a Texas Instruments 0.7" XGA Digital Light Projector (DLP). In order for the illumination beams to produce a pattern with maximum contrast, they must be polarized perpendicular to the diffraction grating. The polarization is controlled with a linear polarizer (Thorlabs LPVISE100-A) mounted in a motorized rotation stage (Altechna 8MRU) . To maintain the optical quality of the structured light, the dichroic mirror (DiM) is a custom dichroic (Omega) on a 9mm thick substrate (CVI) to maintain a better than $\lambda/10$ wavefront.

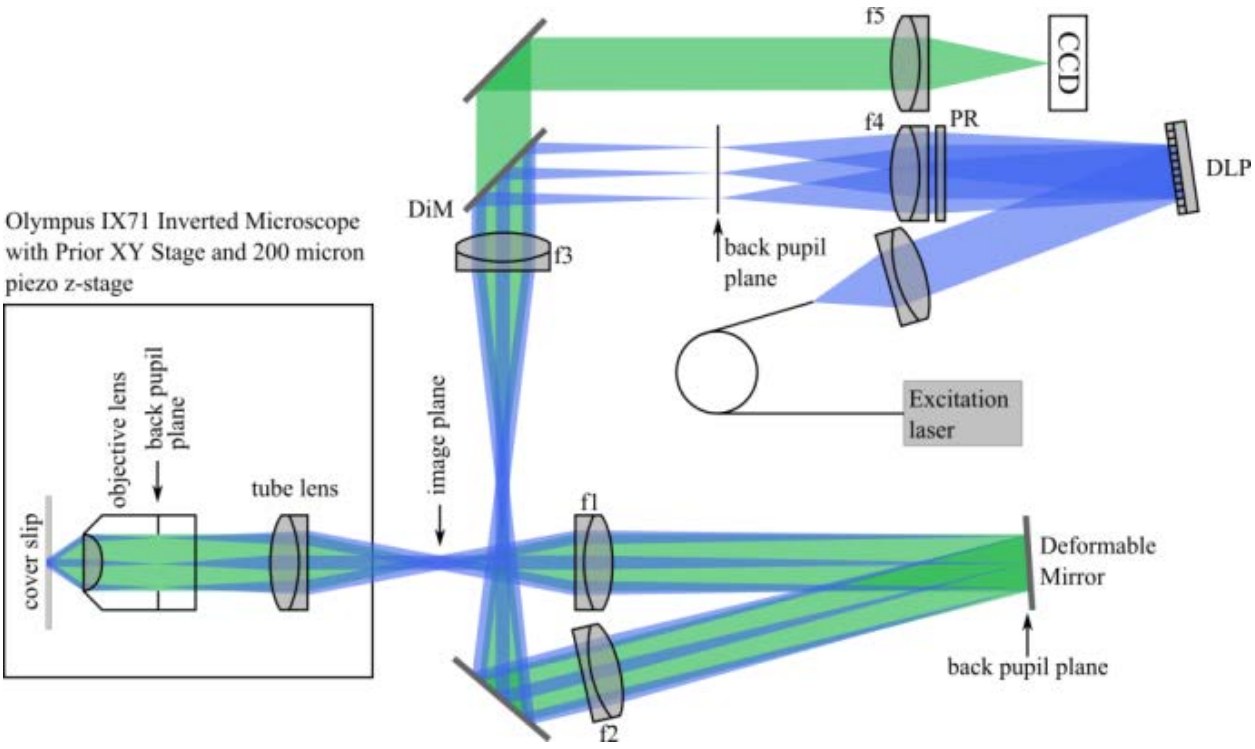

Figure 4.1: Schematic of the AO-SI system used for this study, where: f1=f2=350mm, f3=100mm, and f4=f5 = 300mm.

The DM acts as the Adaptive Optic correction element and is aligned to the back pupil plane of the microscope. This mirror consists of 52 electromagnetic actuators beneath a 15mm reflective surface. Corrections of aberrations caused by a full grown *C. elegans* (discussed in Chapter 6) show that the magnitude of aberration is well within the capabilities of the deformable mirror. The DM is capable of a ±35μm stroke for Defocus aberrations and ±30μm stroke for Astigmatism. The influence function matrix gives the relationship between the mirror commands and the wavefront. It consists of an array of 52 wavefront images. Each image represents the wavefront distubanced caused by applying 0.02V to an actuator, or "poking" the piston. An example of the wavefront by "poking" a single piston a single piston is shown as Figure 4.2.

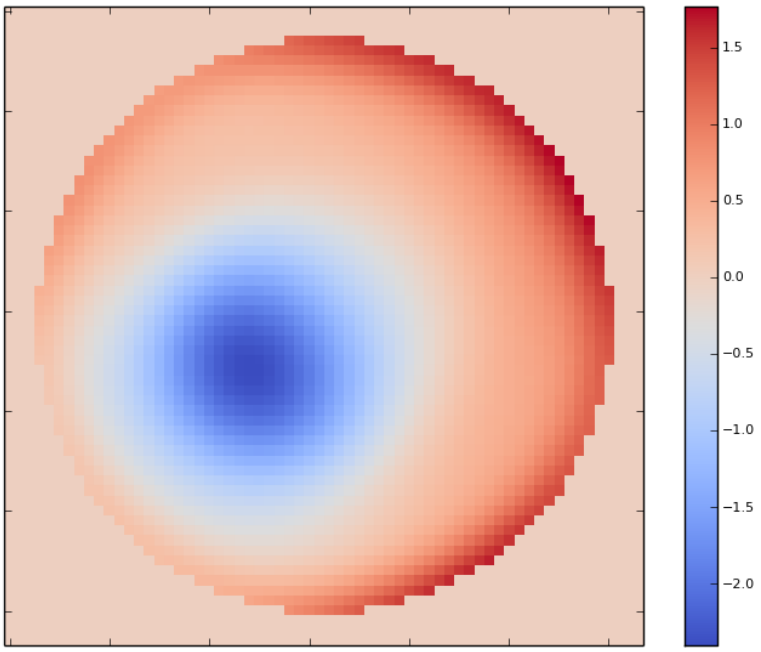

Figure 4.2: An example image from the influence function matrix giving the effect of a single DM actuator on the wavefront measured by phase retrieval.

The influence function was experimentally determined by sequentially poking the actuators and calculating the wavefront with phase retrieval [67-69]. For each actuator, a three dimensional image stack of a 200nm diameter microbead fixed to the coverslip was acquired at 200nm intervals. The axial extent of the 3D stack was 4 microns resulting in total of 21 images for each measurement. The bead acts as a point source. The wavefront phase is iteratively determined from intensity measurements at various axial offsets from the focused bead by minimizing the relative entropy between the theoretical and measured intensity distributions [69]. Sixty four iterations of the algorithm were performed for each wavefront measurement.

The wavefront resulting from poking an actuator is subtracted from the wavefront measured when no actuators are poked to isolate its effect.

Correcting system aberrations

Aberrations caused by the optical components were corrected so that the system maintained an initial Strehl ratio greater than 0.85 for imaging at the coverslip. The correction is performed by first measuring the wavefront phase and amplitude at the back pupil plane using phase retrieval. The measured phase is decomposed using Zernike polynomials. This was accomplished using a set of orthonormal vector polynomials derived from Zernike polynomials [70, 71]. The Zernike values are multiplied by -1 and then applied to the mirror.

Through several iterations of measurement and correction, system aberrations were removed. The wavefront of the system before correction is shown as Figure 4.3a. The wavefront after correction with phase retrieval is shown as Figure 4.3b. The large amount of aberration is due to the shape of the deformable mirror with all actuators set to 0V, which is not flat. The PSFs corresponding to the wavefronts in Figure 4.3 are shown in Figure 4.4. Figure 4.4a and 4.4b show the lateral (xy) images of a fluorescent bead before and after optimization respectively. Figure 4.4c and 4.4d show the xz profiles of the beads before and after optimization. For the xz images, the z pixel dimension (vertical) is 200nm.

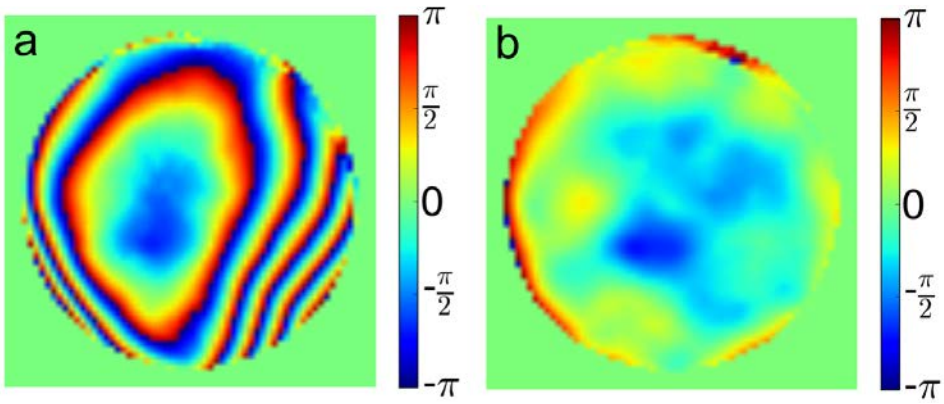

Figure 4.3: Phase aberration present in the system with the Mirao 52e deformable mirror actuators set to zero (a) and after correction with phase retrieval (b).

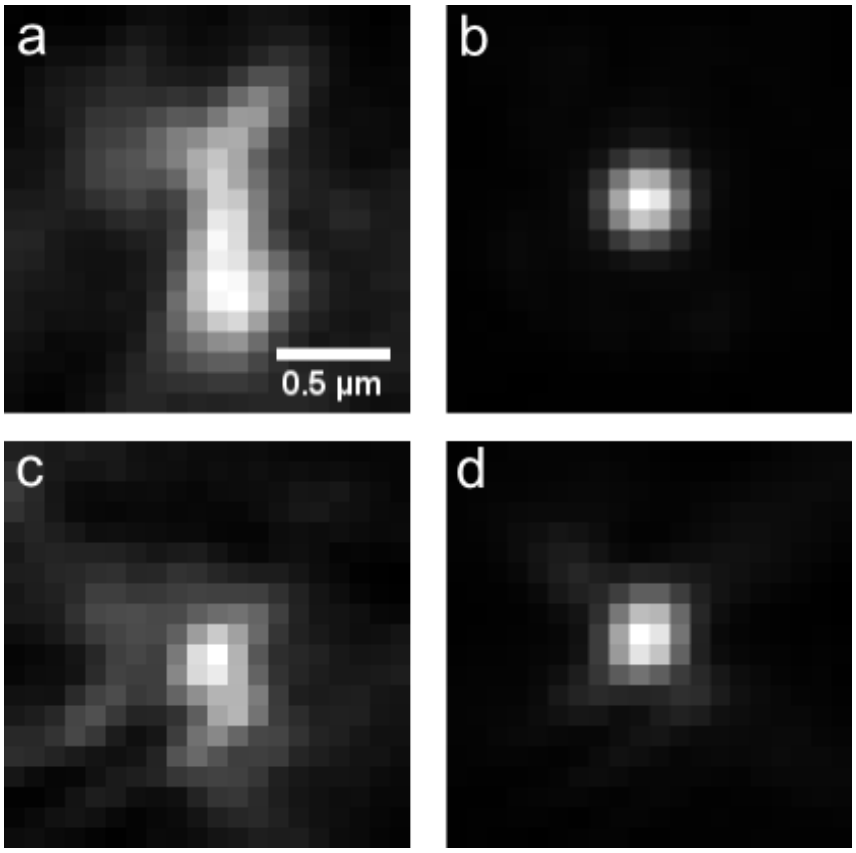

Figure 4.4: The PSF of a single bead before (a,c) and after correction (b,d). Figures a and b show the xy images of the bead before and after optimization of the DM with phase retrieval respectively. The xz images before and after optimization are shown as c and d. The vertical pixel length is roughly double the horizontal pixel length in the xz images.

Optical alignment

The precise alignment of the optical components is critical for producing the best image possible, and is especially important for creating a diffraction limited illumination pattern at the sample. To aid in alignment, a Thorlabs S1FC635 laser was mounted into an empty objective lens port in the IX 71 microscope. The laser exits the side port of the microscope at 3.5 inches above the optical table. Working from the side port of the microscope each lens was placed at its proper distance along the optical axis by measurement with a ruler and using the laser as a rough guide. To precisely align each lens so that the laser passed through its center, the alignment laser was passed through a small iris before it was allowed to hit the lens. The reflection of the laser off of the front and back surfaces of the lens was observed at the iris. Final adjustments to the lens placement were made by aligning the reflections and adjusting the tilt of the lens so that all the reflections returned back through the iris. The placement of each lens was optimized in this manner sequentially starting from the microscope and going working towards the Andor camera.

The alignment of the illumination arm needed for SIM presented its own challenges. The face of the DMD must be precisely aligned so that it is conjugate to the focal plane of the objective lens. Diffraction causes the illumination pattern to have a finite axial extent over which it will have high contrast. Furthermore, the lens l4 must be precisely placed so that the mask is conjugate to the back pupil plane of the objective lens. To accomplish this task, the DMD and lens l4 were placed initially based on ruler measurements. The distance along the optical path between lens l4 and the DMD was adjusted by observing the focused spot produced by the illumination beam at the DM. A micrometer attached to the base of the DMD allowed its placement to be finely adjusted to produce the smallest focal spot at the DM.

The distance between lenses f4 and f5 were finely tuned by observing the image of the fiber tip on the ceiling of the optics room after it passes through the objective lens. Lens l4 was placed on a cart and rail system (Thorlabs) to constrain the movement of lens l4 so that only movements along the optical axis were allowed. By iterating between these two adjustments, the illumination arm optics were accurately placed. Lateral adjustments were accomplished by a set of mirrors placed between lenses l4 and l5. The mirror closest to lens l4 was adjusted so that the illumination laser hit the center of the DM. The mirror closest to l5 was adjusted so that the illumination laser hit the center of an iris placed in front of the microscope side port. By iterating between these two adjustments the lateral alignment of the illumination beam was accomplished. For SIM, the mask was placed conjugate to the back pupil plane by observation at the DM. When the mask is placed conjugate to the back-pupil plane, an image of the mask holes is formed at the DM.

Creating a Structured Illumination Pattern.

Various devices have been used to create the illumination pattern necessary for SIM. One common method for creating the illumination pattern is to attach a phase grating [50], or a physical grid [55] to a precisely controlled piezo stage. As discussed in Chapter 2, the illumination pattern must be shifted by a precise phase in order for the reconstruction of a super-resolution image to be possible. For this research, a Digital Micromirror Device (Texas Instruments 0.7" XGA, D4000 development kit) is aligned to the image plane of the microscope and used to generate the illumination pattern. The DMD consists of an array of 1024x768 square mirrors which are 13.6μm across, with an overall efficiency of 89%. To measure the efficiency,

a collimated laser is passed through an iris to limit the beam size. Its power before and after it is incident to the DMD is measured and used to find the efficiency. The diffraction efficiency to the first order was also measured, using a 6 pixel wavelength pattern at the DMD. After the colliminated laser reflects off the DMD, it passes through a 270mm lens to separate the diffraction orders. A second iris is used to block all diffraction orders not being measured. The DMD has an 18% diffraction efficiency for the first order.

The micro-mirrors can be considered both opto-mechanical and electro-mechanical elements. When a current is applied to a micro-mirror, it is flipped along its diagonal from its off state (-12°) to its on state (12°). Switching micro-mirrors from their "off" to "on" state can be performed at 1 kHz. Instead of relying on a precisely positioned grating, the illumination pattern can be shifted by switching sets of mirrors on and off. Other advantages include the fact that the illumination pattern frequency can easily be adjusted, and rotation of the illumination pattern does not require additional hardware.

General microbead slide procedure

Three types of microbeads are used for our research; they are listed in Table 5.1. The general procedure for creating microbead slides is presented here. The first step is to dilute the microbeads from their initial concentrations. For dense slides, they are typically diluted by a factor of 10^3. When sparse bead samples are required, such as for phase retrieval, they are diluted by a factor 10^5. Ethanol and distilled water can both be used to dilute the microbeads. Using ethanol will result in more evenly distributed beads, as the alcohol will be more attracted to the glass than itself. However, ethanol breaks down the flourophores in the beads, thus it no good for long term storage. 15µl of the diluted mixture is

dried to a coverslip on a hotplate at 35°C. 15µl of glycerol is then applied to a slide, and the coverslip is placed on top. The edges of the coverslip are painted with over-the-counter nail polish hardener to fix the slides.

Table 5.1: Microbeads used for testing

Description	Invitrogen Part #	Nominal Diameter	Excitation/Emission
Yellow/green fluorescent	F8811	200nm	505/515
Yellow/green fluorescent	F8803	100nm	505/515
Latex	C37269	450nm	na

C. elegans slide procedure

Various tests are performed using microbeads fixed beneath *C. elegans* samples. The procure procedure for making *C. elegans* slides is presented in general here as several variations were performed. Microbeads are diluted in ethanol, the exact dilution varies and will be divulged alongside specific experiments. 15µl of the solution is then dried to the slide, as opposed to coverslip as described in the previous section. To fix the *C. elegans* samples 5µl of Tetramisole, a paralyzing agent, is applied to the slide. The worms were then transferred to the slide with inoculating loops. The worms were distributed across the slide by manually spreading the poison on the slide with an inoculating loop. After allowing the poison to dry, 15µl of glycerol is added to slide and the coverslip was applied and fixed. To prevent the microbeads

from being washed away from the slide while applying the worms, Colorfrost Plus (Shandon) charged slides are used.

Chapter 5: Linear reconstruction SIM for optical sectioning

In this chapter, I will present the development of a new structured illumination microscopy (SIM) algorithm for optical sectioning. This new method uses the same number of raw images as the RMS method, discussed in Chapter 4 [55]. With a little added complexity, three images can be used to create an optically sectioned image with better resolution, higher contrast and better image fidelity than optical sectioning SIM methods reviewed in Chapter 4. This algorithm is also linear which is an advantage for further post-processing of the image. This new method is first presented and then compared to the different SIM optical sectioning algorithms. Performance of the new SIM algorithm is then shown to have superior performance for low intensity images. Finally, the performance of the new SIM algorithm is demonstrated on several biological samples.

As discussed previously, the RMS-SI method removes the widefield contribution in the observed images to generate and optically sectioned result. This loss of information degrades SNR of the final image. This problem is addressed using a linear reconstruction method to create the final image. Linear reconstruction structured illumination microscopy (LR-SIM) leaves the simplicity of the data acquisition intact while creating a final image with a flatter frequency response and better sensitivity. Following the approach of Gustafsson [50], we consider the set of images $D_i(\vec{r})$ where $\vec{r}$ refers to the full three-

dimensional coordinates. With the illumination pattern given by Equation 3.8 (these patterns are uniform in the $\hat{z}$ direction) at a frequency of NA/λ, three shifted copies of $\tilde{S}\tilde{H}$ are created as given in Equation 3.14. The shifted copies are separated using a linear transformation (Equation 3.15) and the frequency components are manually restored to their proper positions. The components are then re-assembled using a generalized Wiener filter defined as

$$\tilde{D}_{SI}(\vec{k}) = \frac{\tilde{H}^*(\vec{k})\tilde{S}_0(\vec{k}) + \tilde{H}^*(\vec{k}+p\hat{x})\tilde{S}_p(\vec{k}+p\hat{x}) + \tilde{H}^*(\vec{k}-p\hat{x})\tilde{S}_{-p}(\vec{k}-p\hat{x})}{|\tilde{H}(\vec{k})|^2 + |\tilde{H}(\vec{k}+p\hat{x})|^2 + |\tilde{H}(\vec{k}-p\hat{x})|^2 + w^2}. \qquad \textbf{Eq. (5.1)}$$

The parameter *w* is the Wiener parameter which can be used to adjust the bandwidth of the OTF [72]. The Wiener filter will result in a final image with higher resolution than the wide field image in both directions in addition to the added resolution in the $\hat{x}$ direction

Using an excitation pattern of wavelength λ/NA, as in RMS-SI, the three sets of data are shifted by one-half the extent of the OTF. The missing cone in the conventional 3D OTF is filled in by the shifted copies, providing optical sectioning (demonstrated in Figure 5.1).

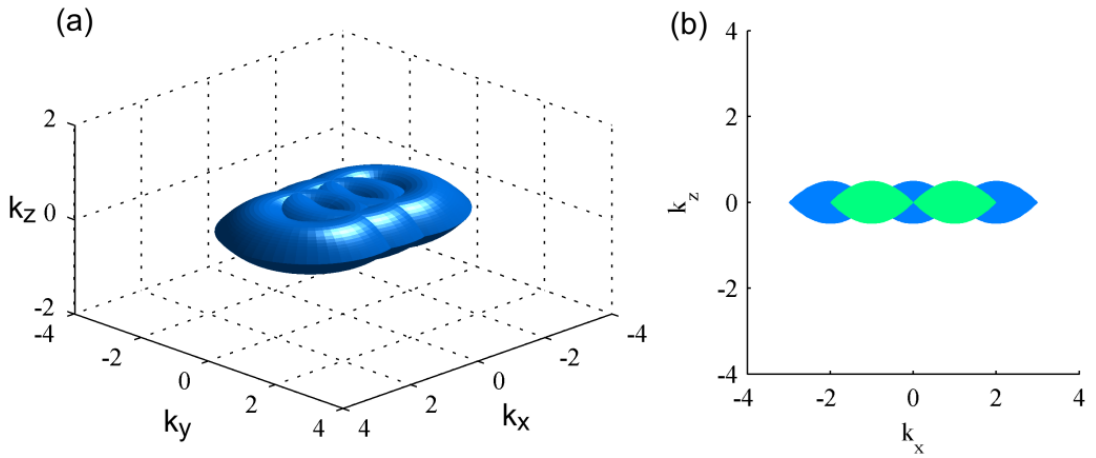

Figure 5.1: Support of the Effective OTF for LR-SI as described by Eqs. (6-11). The axes are in units of NA/λ. (a) three-dimensinoal image of effective OTF support. (b) $k_z - k_x$ cross-section of the OTF support. $\tilde{H}(\vec{k})$ is in green, and $\tilde{H}(\vec{k}+p\hat{x})$ and $\tilde{H}(\vec{k}-p\hat{x})$ are in light blue.

Given our system, the desired pattern wavelength is 400nm. As the DMD is conjugate to the sample plane, the wavelength of the pattern at the DMD is given by

$$\lambda_{p,DMD} = \frac{\lambda_{p,sample}}{2}\frac{f_4}{f_3}\frac{f_2}{f_1}\frac{f_{tube}}{f_{obj}}. \quad \textbf{Eq. (5.2)}$$

Converting the pattern wavelength into DMD pixels (13.6μm width) results in a wavelength near 11 pixels. Due to the facts that pixels are discrete and the wavelength in pixels must be divisible by three so that SIM images can be acquired at relative pattern phases of 0, $2\pi/3$, and $4\lambda/3$, we chose a pattern wavelength of 12 pixels at the DMD. This results in an illumination pattern with a wavelength near 450nm at the sample.

An optical mask blocks all but the ±1 frequency orders of the illumination beam created by the patterned DMD surface. The separation of two beams after focusing by lens f4, which places the mask conjugate to the back pupil plane, is given by

$$d_{mask} = \frac{2f_4\lambda_{laser}}{\lambda_{p,DMD}} \quad \textbf{Eq. (5.3)}$$

where λ_{laser} is the wavelength of the illumination laser (488nm). Given f_4 = 300mm, the separation of the mask holes must be 1.8mm. The optical mask consists of a 1 inch diameter disc with precisely placed holes. The mask is placed in a xxxx stage (Thorlabs xxx). The mask was drafted in Autocad. The drawing was then printed and used as a guide to create the mask out of thick construction paper. A simple sewing needle and a dissecting microscope were used to accurately create the mask holes. The mask holes have a 1mm diameter, which is large enough to allow the desired beam to pass while blocking all other diffraction orders.

This LR-SIM approach requires knowledge of the wavevector $\vec{p}$, but has several advantages over RMS-SI. One being that LR-SIM is completely linear so that the final result can be described by an effective OTF. The reconstruction given by the Weiner filter (Equation

3.13) also provides a relatively flat frequency response over the region of support. The overlap of the terms $S_{0,+p,-p}$ provides a higher signal than RMS-SI as will be demonstrated below. Because the OTF is wider in one direction, the PSF will have an elliptical shape. However, the result, $\tilde{D}_{SI}$, can be apodized to produce an isotropic lateral resolution if this is desired.

Super-resolution image reconstruction

Re-assembling the data requires precise knowledge of the pattern orientation, frequency, and relative phase. The first two quantities are determined by checking the correlation between S_{+p} and S_0 in the area in which they overlap. Figure 5.2 shows the overlap magnitude for a sample of 200nm yg beads fixed to the coverslip over a search area of 0.04 radians and 20nm for the pattern orientation and wavelength respectively.

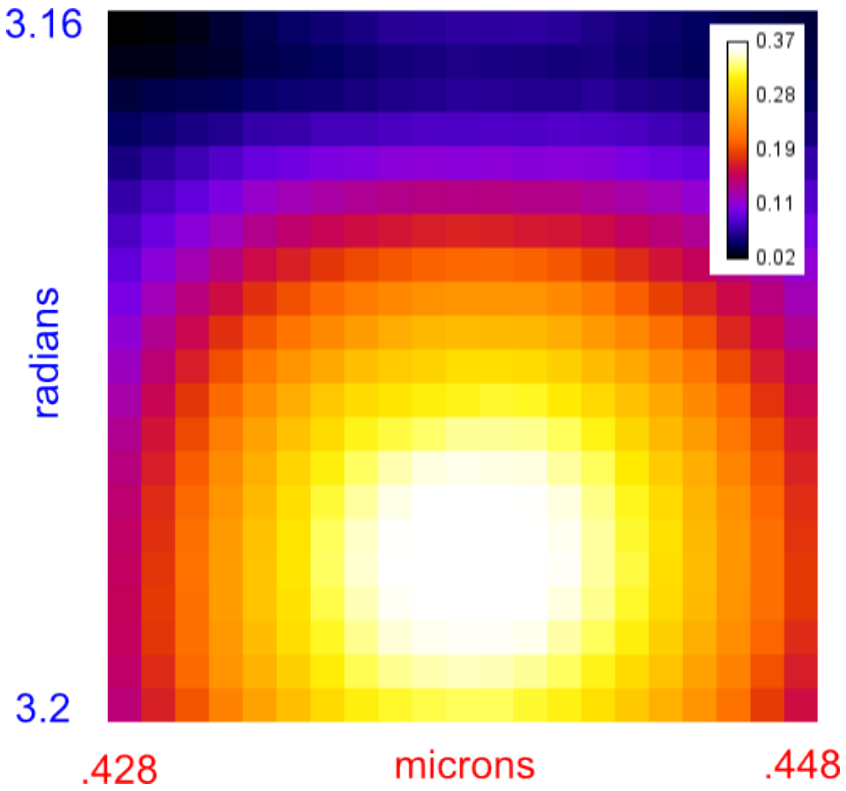

Figure 5.2: Correlation between the widefield and shifted frequency components. The pattern angle (radians) is the vertical dimension and the pattern wavelength (microns) is the horizontal dimension.

To determine the phase (ϕ_i from Equation 3.15) needed for LR-SI, the angle between widefield component and shifted frequency component is plotted. An example is shown as Figure 5.3. The phase used for reconstruction is chosen manually by plotting lines through the phase image. Calculating the phase by an averaging method will produce skewed results due to the noise in the phase, which is severe at the edges of the overlap area.

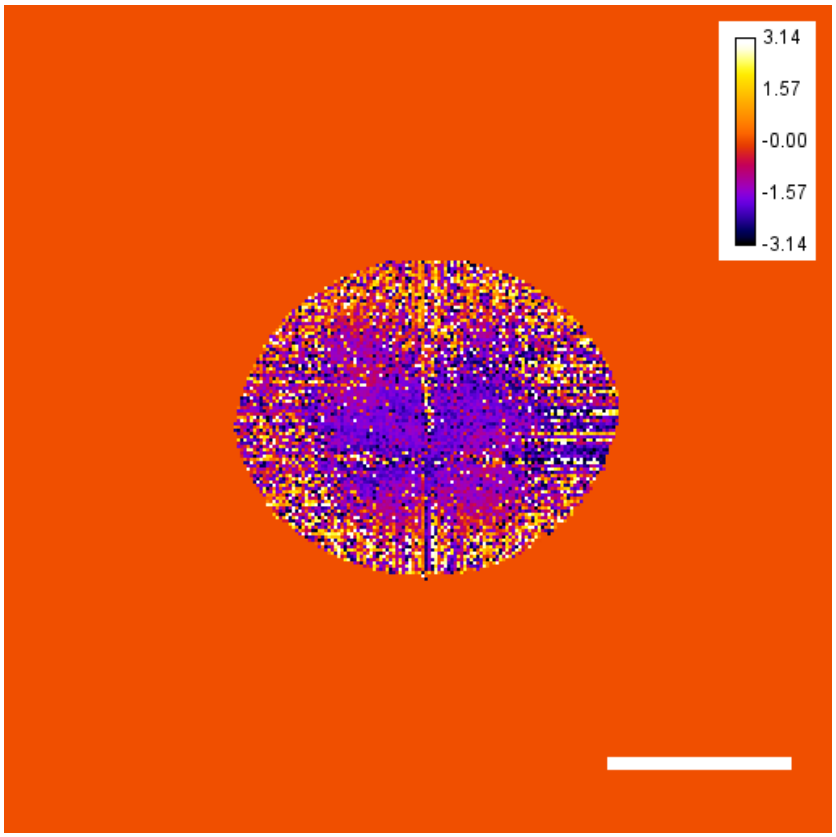

Figure 5.3: Angle (in radians) between the shifted and widefield components. The horizontal and vertical axes are the k_x and k_y vectors in frequency space. The scale bar has a length of $2NA/\lambda$.

Comparison of Optical Sectioning SIM Methods

To compare different structured illumination sectioning methods, several experiments are performed. Widefield, RMS-SI and LR-SI images are all generated from the same set of raw data to make the comparison of images straightforward. The background is removed from all images by subtraction using the average pixel value in an area of the image where no signal exists. The widefield image is simply the sum of the raw images [73].

$$D_{wf} = \frac{2}{3}\sum_i D_i \qquad \textbf{Eq. (5.4)}$$

LR-SIM reconstruction requires the number of pixels to be doubled in each direction so that the pixel size is 44.5nm in the lateral direction and 100nm in the axial direction. For the other methods (RMS-SI, etc.), the pixel size is decreased by a factor of two by Nyquist interpolation so that the final pixel size is 44.5nm laterally and 100nm axially for all images.

Our LR-SIM method was compared to the optical sectioning SIM algorithms presented in Chapter 3. Figure 7.3 shows lateral and axial cross sections of the 200nm diameter fluorescent microbeads using widefield, LR-SI, RMS-SI, Max-Min SI, and the 2D linear method from Equation (3.21) without and with Weiner filtering. At intensities where the signal to noise is high, both RMS-SI and LR-SI produce images with less background light and good axial sectioning although the LR-SI image has higher resolution. The 2D linear techniques, Figure 5.4e and 5.4f, give enhanced resolution in the x direction, but have weak support along the horizontal, y, direction, so they yield images that are strongly asymmetric with stronger noise artifacts than the other methods; we do not consider them further.

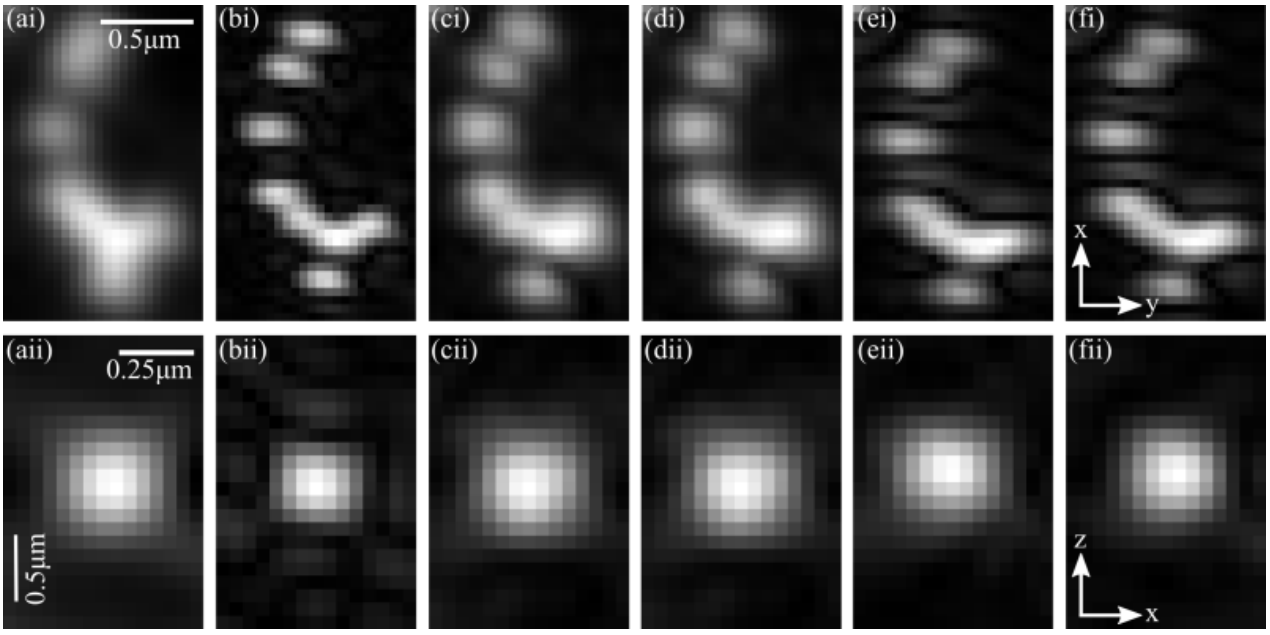

Figure 5.4: Images of 200nm diameter YG beads. The images are from left to right (a) widefield, (b) LR-SI, (c) RMS-SI, (d) Max-Min SI - Equation (3.19) (e) SIM from Equation (3.21), (f) Equation (3.21) with Weiner filtering. The images on the top row (i) are lateral in-focus images, and the images on the bottom row (ii) are axial cross sections. For these images the exposure time is 200ms and the excitation intensity is 5.6 W/cm^2. Estimates of the SNR and Contrast for the images are (a) (80, 3.7), (b) (70, 6.7), (c) (100, 4.1), (d) (86,4.5), (e) (60, 5.7), and (f) (60, 5.9).

At a factor of 37 lower intensity, as shown in Figure 5.5, the difference between RMS-SI and LR-SI becomes more evident. The shape of the beads in the RMS-SI images is distorted compared to the widefield and LR-SI images. Also shown in Figure 5.5 are the results of the Max-Min algorithm, the results of which are comparable to the RMS-SI algorithm. Figure 5.6 shows the Fourier Transforms of the data in Figure 5.4. While not the OTF, these show clearly the region of support of the OTF for the different techniques.

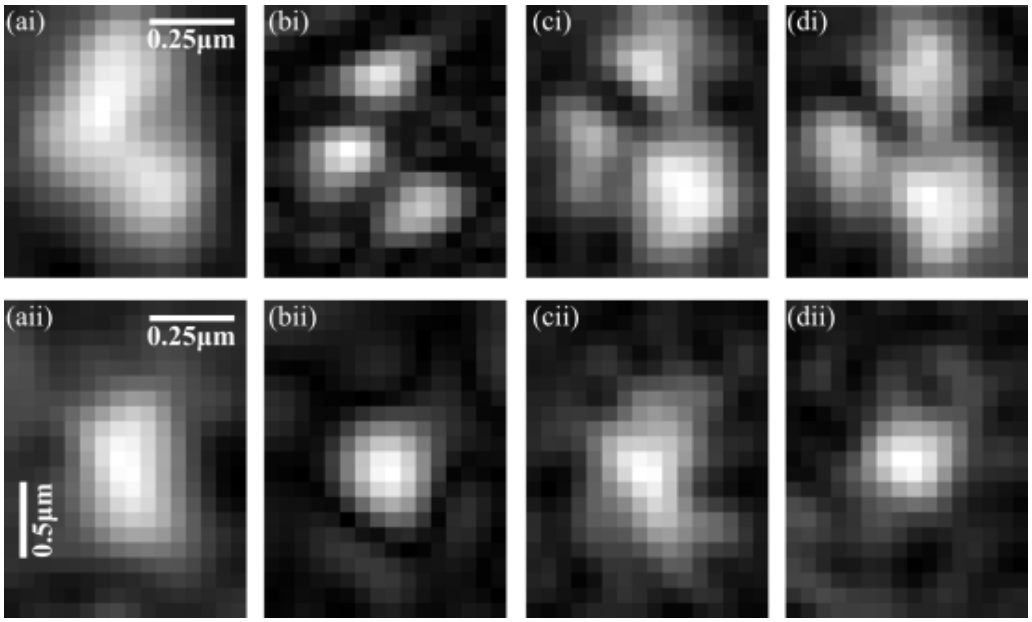

Figure 5.5: Images of 200nm diameter YG beads at low intensity. The images are from left to right (a) widefield, (b) LR-SI, (c) RMS-SI, and (d) Max-Min SI. The images on the top row (i) are lateral in-focus images, and the images on the bottom row (ii) are axial cross sections. For these images the exposure time is 10ms and the excitation intensity is 3.0 W/cm^2. Estimates of the SNR and Contrast for the images are (a) (12, 2.0), (b) (20, 4.7), (c) (18, 2.7), and (d) (22, 2.7).

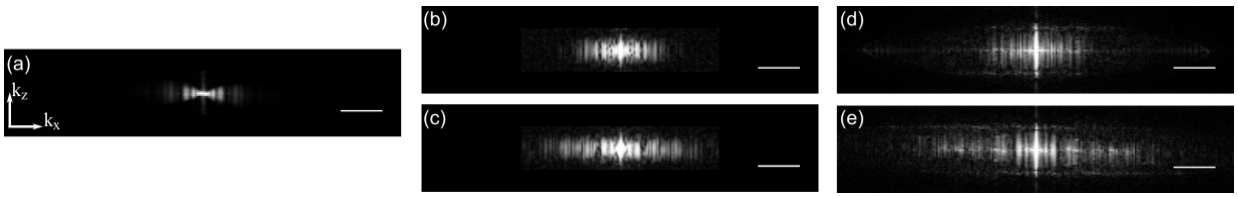

Figure 5.6: Cross-sections of three-dimensional Fourier transforms of data for images of 200nm YG beads. The vertical axis is and the horizontal axis is either (bottom) or (top). (a) widefield. (b) and (c) for RMS-SI. (d) and (e) for LR-SI. The scale bar has dimension . Each image is scaled using the formula $1 - e^{\left(-\frac{I(r)}{a}\right)}$ where a is 1% of the maximum intensity; the scaling is performed to highlight the extent of the OTF.

The signal to noise ratio (SNR) for an image (widefield or SIM) is calculated as follows. The noise is represented as the standard deviation of the intensity and the signal is calculated as the mean of the 10 highest intensity pixels. The calculations are done on the in-focus image plane, and the SNR is then the signal divided by the standard deviation. To estimate the SNR from a single image, the standard deviation is calculated in an area without signal. From multiple images of the same scene, the standard deviation is calculated by subtracting the images as in Figure 5.7, which shows an RMS-SI image and an LR-SI image along with the noise image for each. Calculating the SNR as the intensity from the image divided by the standard deviation of the noise image yields an SNR of 11.5 for the RMS-SI image and an SNR of 22.2 for the LR-SI image. The contrast is calculated as the difference in the maximum signal and minimum signal divided by the mean. The maximum and minimum are calculated as the mean of the 10 highest and lowest intensity pixels respectively from the in-focus image plane. The SNR comparison of the RMS-SI and LR-SI methods is shown as Figure 5.8.

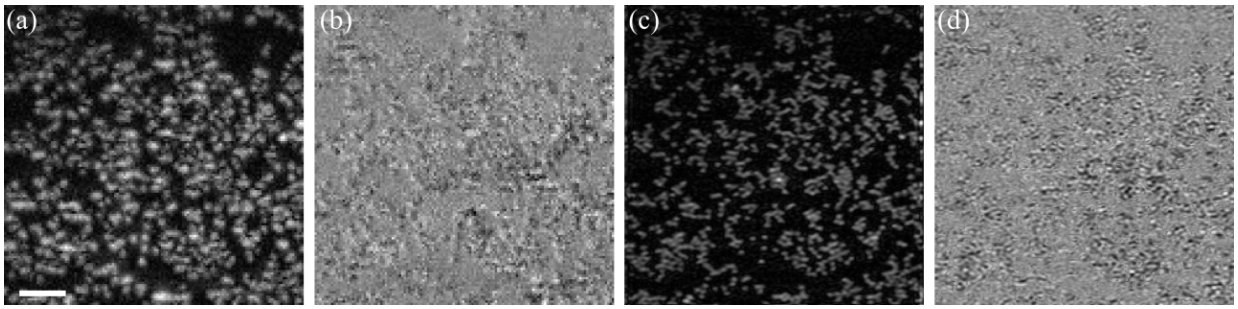

Figure 5.7: (a) RMS-SI image of 200nm YG beads. (b) Subtraction of the RMS-SI image in (a) from an image of the same scene. (c) LR-SI image. (d) Subtraction of two LR-SI images. The RMS-SI image and the LR-SI image were calculated from the same set of raw data. For these images the excitation intensity is 3.0W/cm2. The exposure time for the images in (a) and (c) was 10ms. A 15ms exposure image was used to create the second images for subtraction and was scaled by a factor of 2/3. To account for drift between capturing the two sets of data, the second images were shifted by sub-pixel amounts to yield a cross-correlation peak centered at the origin.

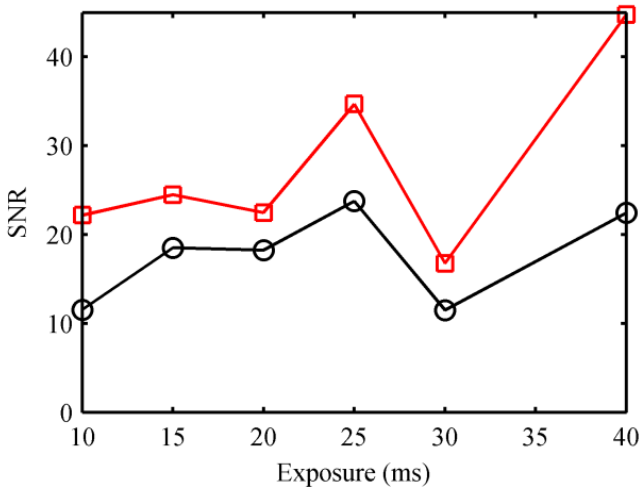

Figure 5.8: Comparison of the SNR for different exposures for RMS-SI (black line, circles) and LR-SI (red line, squares). The LR-SI SNR is 50% to 100% higher than the RMS-SI.

Three raw images are collected to generate RMS-SI and LR-SI images. These three sets of data can be used to generate three different sets of data: S_0, S_p, and S_{-p}. These are all complex but $S(-k) = S^*(k)$, because the images are real, so only 3 sets of real data are generated. The final image in RMS-SI is calculated from $|\tilde{S}_p|$, so it only uses two sets of information, whereas LR-SI makes use of all three sets of data. The extra information in LR-SI improves the quality of the image but does not directly translate to a 50% increase in SNR. The sets of data are not directly comparable because RMS-SI operates on each z-slice as a 2D image, and LR-SI treats the image stack as a 3D image. Furthermore, the Wiener filter, Equation. (5.1), boosts the amplitude of higher spatial frequencies increasing the noise in addition to signal at higher frequencies. Figure 5.9 shows lateral and axial cross-sections of the effective OTF for LR-SI.

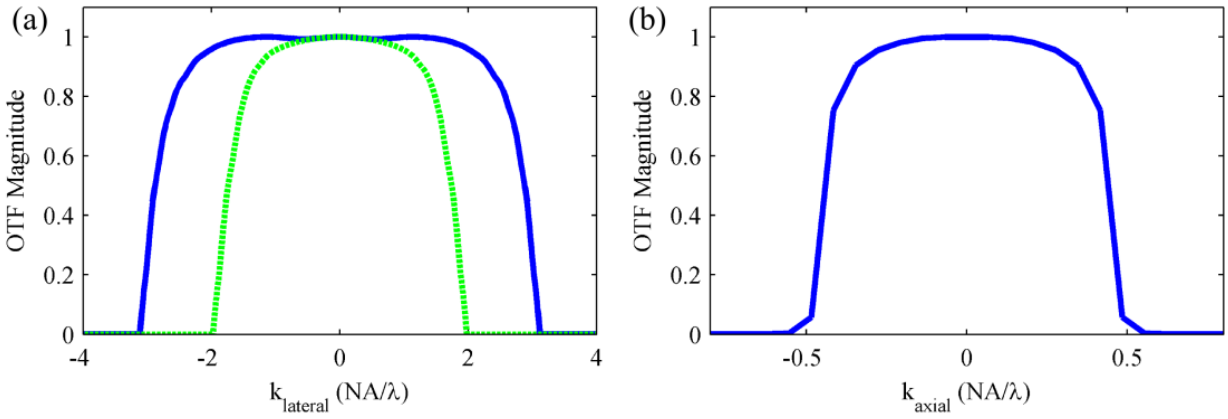

Figure 5.2: Cross sections of the effective OTF for LR-SI in the lateral direction (a) and the axial direction (b). In (a) the blue solid curve is along the x-direction and the green dashed curve is along y. All curves are through the origin. These curves were generated with the term *w* from Eq. (11) equal to 1% of the maximum value of the OTF.

As shown in Figure 5.7 and Figure 5.8, LR-SI yields a higher SNR, and provides a higher contrast more accurate image as shown in Figure 5.5. This is due to the flatter frequency response from the effective OTF of LR-SI and the additional information provided by including the term S_0 in the reconstruction. The Wiener filter included in the constructing of the final image in LR-SI, Equation 5.1, provides a flat frequency response which accounts for the higher resolution and contrast seen in the LR-SI images.

Comparison of LR-SIM and RMS-SI by Simulation

We have performed simulations to compare the two methods. We simulate raw images of a uniform fluorescent sheet by multiplying the sheet by the sinusoidal intensity pattern with a wavelength of λ / NA and multiplying in frequency space by the optical transfer function (OTF).

Each slice in a 3D image stack is generated by multiplying by the appropriate defocused OTF where the OTFs are generated using the Stokseth approximation [74]. Additive Gaussian noise is then added to each image. The results show that LR-SI produces an SNR roughly two times greater than RMS-SI for a uniform sheet. This is shown in Figure 5.10a, where the image SNR is plotted for the two methods. At high noise, the image SNR for RMS-SI appears to level off at ~2. This is an artifact due to the effect of RMS-SI on the noise. At low SNR, the algorithm will produce noise with a nonzero mean from zero-mean noise because the algorithm produces a positive result. Thus the ratio of the mean (of the fluorescent sheet) to the standard deviation will approach a value determined by the noise characteristics, not by the SNR.

Also shown in Figure 5.10 are cross-sectional images of the fluorescent sheet using the two methods for an input SNR of 10 (that is the standard deviation of noise of the raw images is 0.1 relative to the intensity of the fluorescent sheet). At these high noise levels, the image provided by LR-SI is clearly superior. Also evident in these images is the difference in the character of the noise from the two algorithms. The noise in the RMS-SI image remains white noise, while LR-SI produces correlated noise due to the filtering operations in Equation 5.1.

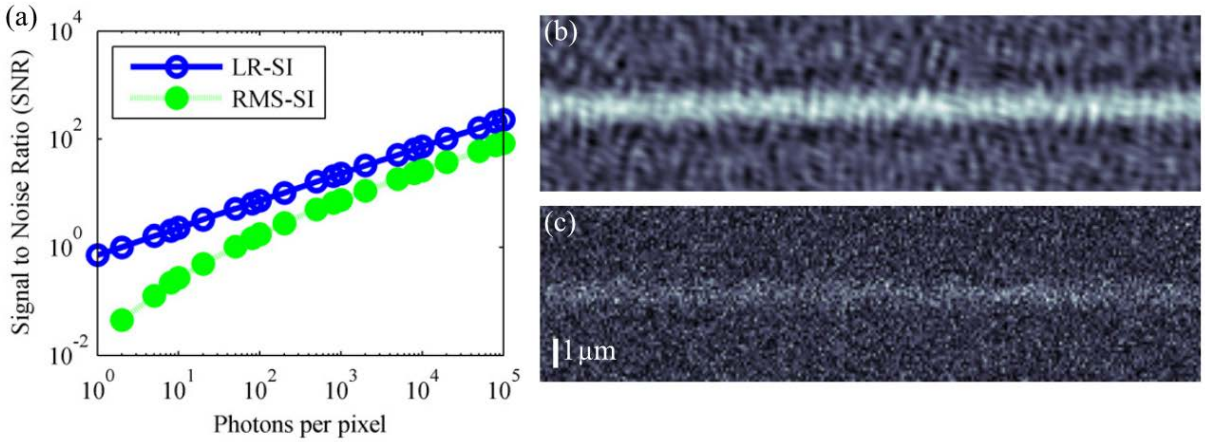

Figure 5.3: Simulations of RMS-SI and LR-SI applied to a uniform sheet. (a) Signal to Noise Ratio of final images for different photons per pixel. Each pixel is 50nm x 50nm. Axial cross-sections of the final images for 50 photons per pixel for LR-SI (b), and RMS-SI (c). This corresponds to an emission intensity of $8\frac{\mu W}{cm^2}$ for a 100ms exposure.

LR-SIM and RMS-SI biological sample comparison

LR-SIM and RMS-SI were further compared using a weakly fluorescent biological sample. To visualize AspB-GFP, Aspergillus nidulans strain AY50 (An-H1-chRFP::pyroAAf, aspB-GFP-pyrGAf) was constructed using standard genetic methods and prepared for microscopy as described in Hernandez-Rodriguez et al [75]. Briefly, spores were incubated in 10ml of minimal liquid medium in a Petri dish containing a glass cover slip at 30°C for 4-5 hours. Coverslips with adhering fungus were incubated for 15 min in 2% formaldehyde in phosphate buffered saline, pH 7.4. Coverslips were washed three times in phosphate buffered saline, pH 7.4 and inverted onto a microscope slide with mounting solution (50% glycerol, 49.9% phosphate buffer, pH 7.0, 0.1% n-propyl gallate). All Aspergillus samples were provided and prepared by Michelle Momany's lab in the Plant Biology Department at UGA.

Figure 5.11 shows images obtained using widefield, LR-SI and RMS-SI of the GFP labeled septin AspB expressed from the native *aspB* gene promoter in an *Aspergillus nidulans* spore soon after breaking dormancy. The septins form a cytoskeletal system in animal and fungal cells and play important roles in nuclear division, cellular organization and cytokinesis. Septins form a variety of higher order structures whose organization is only beginning to be understood [76]. The axial sectioning by both the RMS-SI and LR-SIM techniques is evident, but the structure of the septin ring is much clearer in the LR-SIM image.

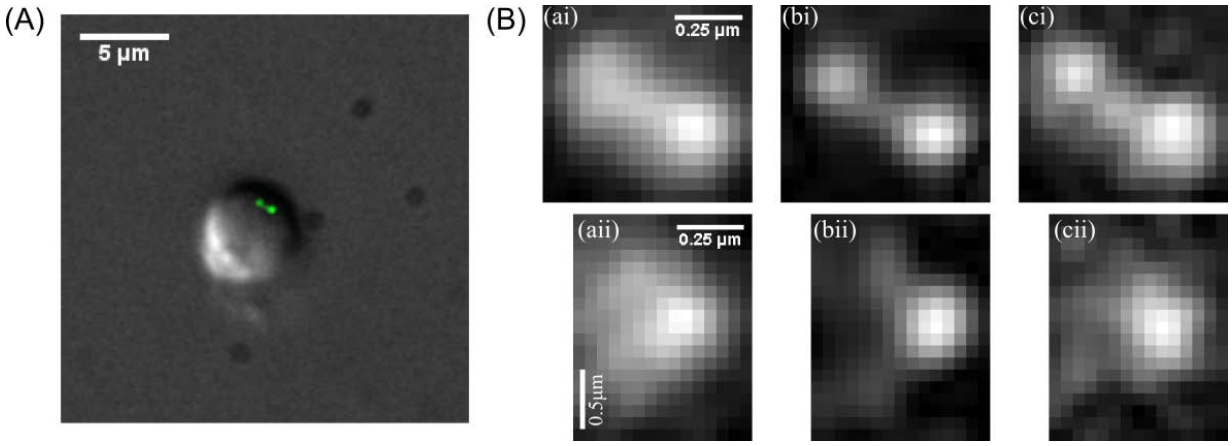

Figure 5.11: Images of GFP labeled septin AspB expressed from the native septin promoter in an *A. nidulans* AYR50 spore after 4 hours of incubation. (A) DIC image of an expanding spore with the fluorescence image (bi) super-imposed (green). (B) Lateral (i) and axial (ii) images using (a) widefield imaging, (b) LR-SI and (c) RMS-SI. For these images the exposure is 2s and the excitation intensity is 5W/cm^2.

The benefits of the LR-SI method are further demonstrated on *C. elegans* strain SJ4103, which expresses GFP in mitochondria. These samples were provided by Edward Kipreos' lab in the Department of Cellular Biology here at UGA. As shown in the Figure 5.12, out-of-focus light and conventional resolution makes the structure of the mitochondria impossible to distinguish. In the LR-SIM

reconstruction, the mitochondrial structure is apparent. The numbers of photons captured by the maximum intensity pixel for the raw images after background subtraction are relatively low. They are 570 and 1250 for the images on top and bottom row respectively. These low intensities result in noisy reconstructions with RMS-SI.

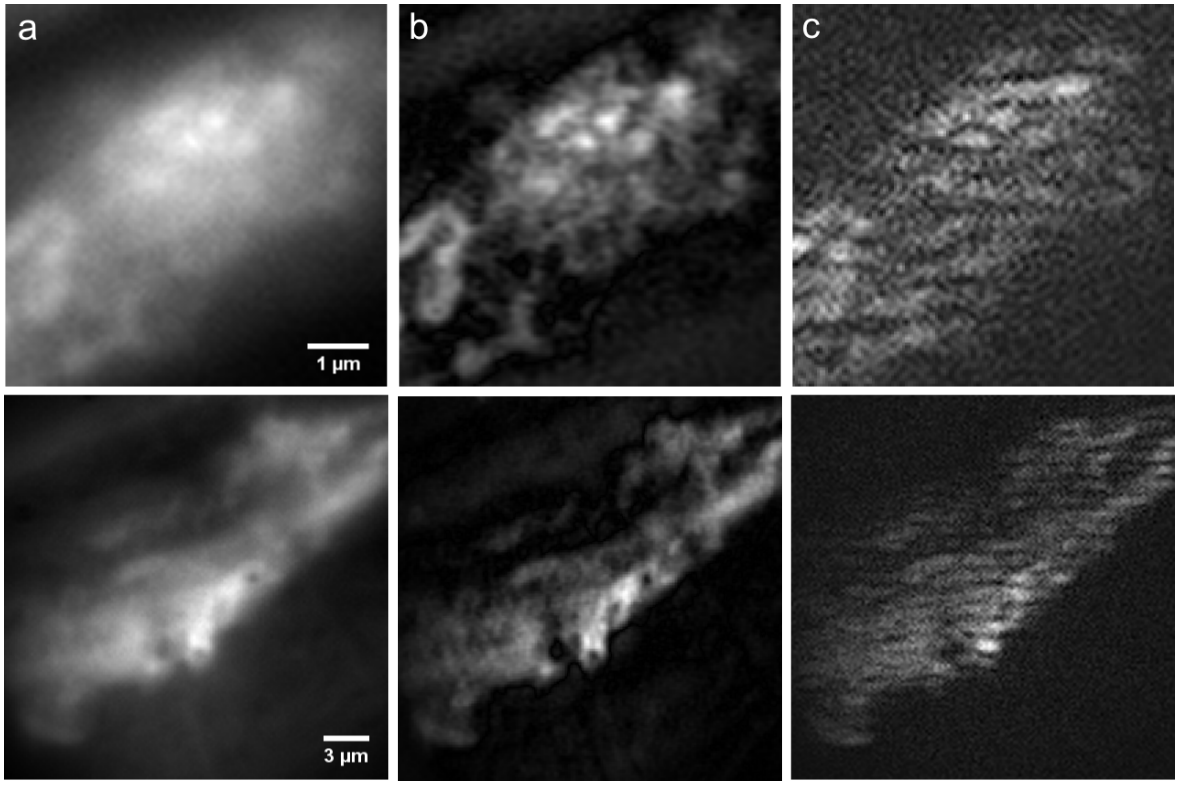

Figure 5.12: Widefield (Column a), LR-SIM (Column b), and RMS-SI (Column c) images of GFP labeled mitochondria in *C. elegans*.

Two-color LR-SIM

Two-color LR-SIM is demonstrated using AspB spores. The septin of the spore is tagged with GFP as described above. The membrane of the spore is stained with FM 4-64FX (Life Technologies). The excitation/emission spectrum for FM 4-64FX is shown as Figure 5.13. The large Stokes shift of the dye allows the 488nm laser to be used as the excitation source for both channels. To separate them, Semrock FF01-520/35-25 and FF01-515/588/700-25 filters are used at the Andor camera.

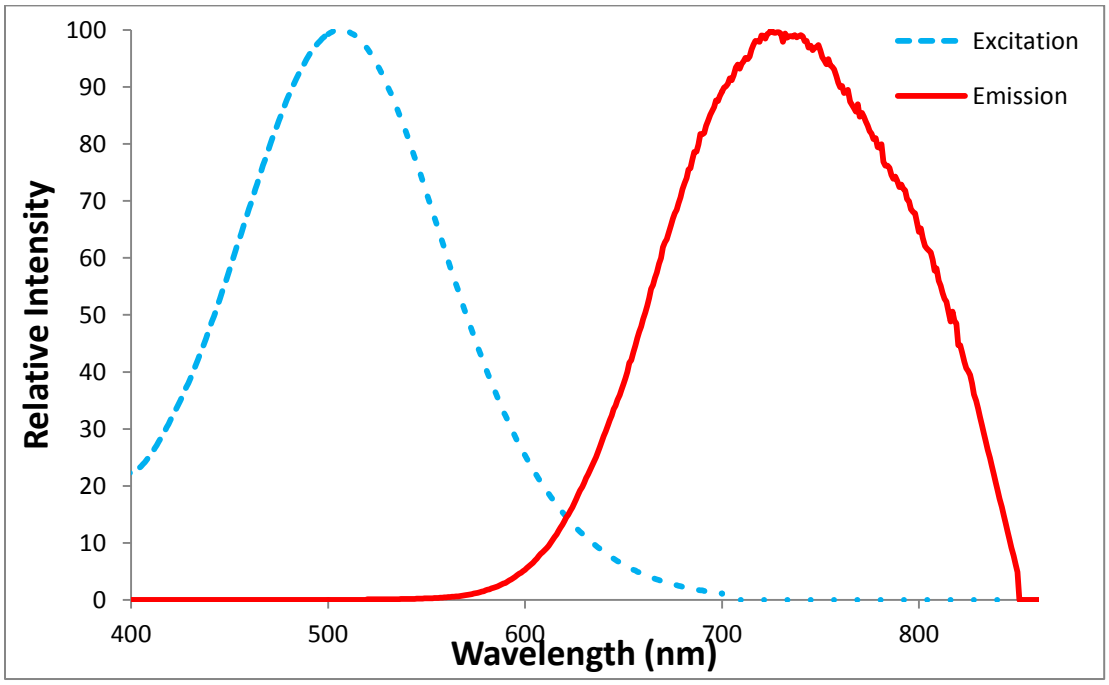

Figure 5.13: Excitation/emission spectrum for FM 4-64FX stain (Life Technologies).

A slice of the LR-SI reconstructed image images is shown in Figure 5.14 alongside the widefield version. To compensate for chromatic differences in focus for the two-color images, the green channel images are shifted by 200nm in the z direction. This difference in focus was found by imaging 100nm

diameter, multi-color, fluorescent microbeads (Life Technologies). As shown in the figures, the optical sectioning and resolution enhancement of the LR-SIM images greatly improves image quality. The irregular shape of the membrane is due to the fact that it is in the process of division. Although the role of the septin is generally understood, its role in cell division is unknown. Two-color LR-SI may help to determine its function.

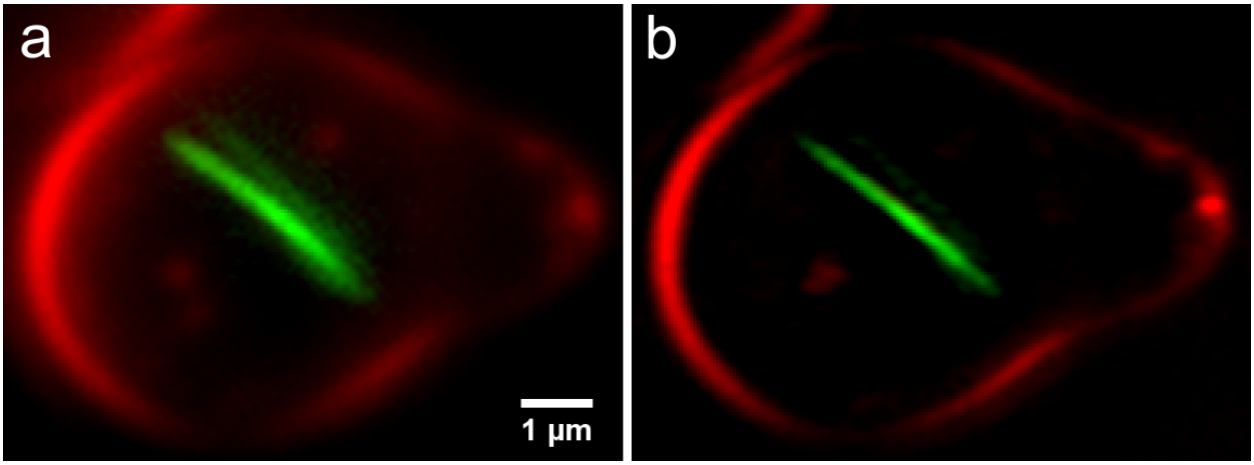

Figure 5.14: Two-color images of AspB spores where the septin (green) is labeled with GFP and the membrane (red) is stained with FM 6-46FX (Life Technolgies). The widefield image is shown as (a) and the LR-SI reconstruction is shown as (b).

Chapter conclusion

In this chapter, I presented an alternative processing strategy for optical-sectioning structured illumination microscopy with 3-phases and a grid wavelength of λ/NA. It was demonstrated that this method, linear-reconstruction SIM, provides a higher contrast and higher resolution image than the original Root Mean Square SI approach for a given set of raw data. This comes at the expense of a more complicated processing algorithm. Given the weak signal from many biological samples and the

importance in keeping the excitation intensity as low as possible, the improvement offered by this method can be significant. These improvements were demonstrated on a variety of biological samples. Finally, two-color LR-SIM was demonstrated.

CHAPTER 6: SUPER-RESOLUTION IMAGING THROUGH THICK TISSUE WITH AO AND SIM

In this chapter, I will present our system which combines the deep-tissue capabilities of AO and the enhanced resolution of SR-SIM (AO-SIM). I will begin with a discussion of the Adaptive Optics, including control of the deformable mirror and the correction algorithm. I will then introduce our 2D, super-resolution, structured illumination microscopy (SR-SIM) system. Finally, AO-SIM is demonstrated by producing super-resolution images of microbeads fixed beneath an aberrative sample.

AO Correction Algorithm

To image through thick tissue, sample aberrations must be corrected. I accomplished this task by implementing a sensorless Adaptive Optic system as per Booth et al. [21], with the Mirao 52e deformable mirror (DM) as the correction element. The system is intended for correction of large aberration magnitudes, and accomplishes this task through a two-step correction scheme. First, a single Zernike mode is induced through the DM at various magnitudes. The induced aberrations are commonly referred to as "guess" or "bias" aberrations The mirror commands (a 52x1 vector of voltages, A) that generate bias

aberrations for various modes and magnitudes are found through Equation 6.1, which assumes that the relationship between actuator command signals (voltages) and the wavefront is perfectly linear. The relationship between the wavefront vector (W), the influence function matrix (H), and the actuator voltage vector (A) is mathematically represented as

$$H * A = W. \qquad \textbf{Eq. (6.1)}$$

The influence function is stack of fifty-two images, where each image is 128x128 pixels. Reshaping the influence function to a 16384x52 vector and performing matrix multiplication with the 52x1 vector of actuator voltages results in a 16384x1 wavefront vector that can be reshaped into a 128x128 image.

To solve for the mirror commands needed to generate a specific bias aberration, the inverse of the influence function array is determined with singular value decomposition (SVD) [77]. SVD gives the least squares solution for over-determined inverse of H. Twenty one low order singular values are retained in the inverse calculation. The matrix multiplication of the inverse influence function and the Zernike aberration mode (wavefront) results in a 52x1 vector of voltage commands. The mirror commands which generate bias aberrations are only dependent on the influence functions, so they can be pre-calculated to reduce acquisition time. The mirror commands will not be zero when the bias aberrations are applied, as the mirror has been set to compensate for system aberrations (as described in Chapter 4). The DM commands which remove the system aberrations will be referred to as the "flat file". The bias commands must be added to the flat file.

The search range for each Zernike mode is over a magnitude range of $M = \pm 10$, where M is defined in Equation 2.9, at integer step sizes for a total of 21 bias images. Initially, the intensity of a single point source is used as a correction metric, and is measured from a user defined 20x20 pixel region of interest. To test the response of this metric, astigmatism (Zernike mode 5) was induced into the optical path at the DM at a magnitude of 3 radians. Figure 6.1 shows the maximum intensity of a

single 200nm fluorescent microbead under bias aberrations for this mode. As shown, the intensity of a bright point source behaves well as a metric, with a definite peak around -3 radians, the appropriate correction. After the correction algorithm determines the best bias aberration magnitude for a given metric, correction is applied and the "flat file" is updated.

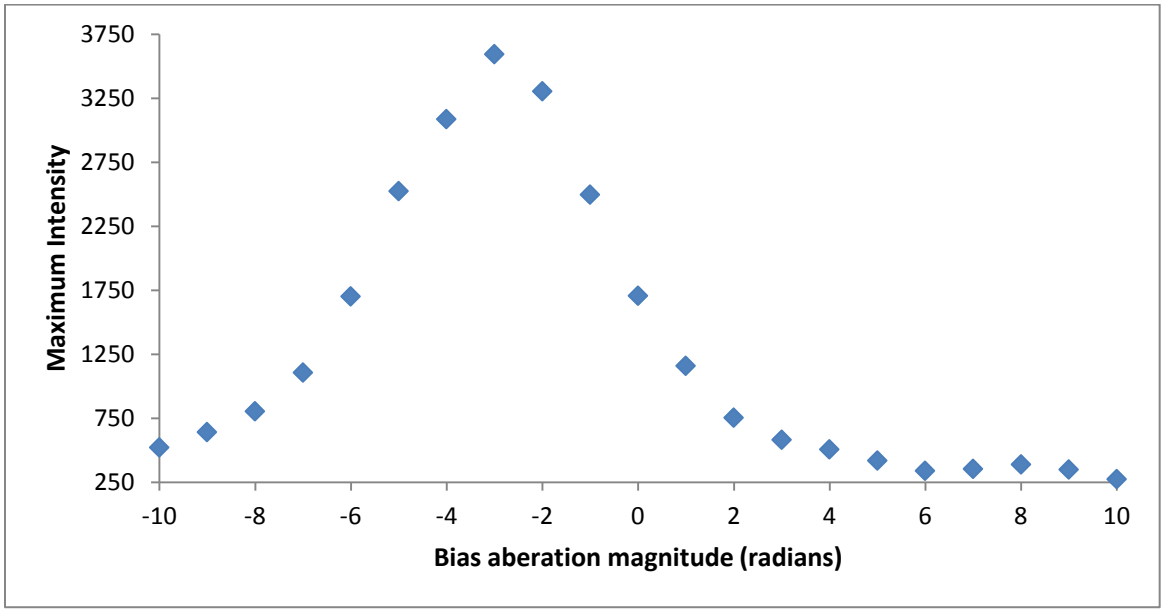

Figure 6.1: Maximum intensity of a single 200nm microbead. 3 radians of astigmatism (Zernike mode 5) are added to the wavefront to aberrate the image. Various magnitudes of astigmatism are then applied and to detect the induced aberration

The second step of the correction algorithm is to optimize the shape of the mirror. A parabolic fit using five of the correction metric values is performed to determine the optimal magnitude of aberration to remove. An example is shown in Figure 6.2. The aberration magnitudes used for the parabolic fit are 0 (no aberration), ±2, and ±1 radians. To ensure that the parabolic fit did not detect a valley and thus minimize the metric, no corrections are applied if the slope of the parabolic coefficient found by the fitting

procedure is positive. Zernike modes 5, 6, 7, 8, and 11, corresponding to astigmatism, coma, and spherical aberration, are corrected sequentially by applying an initial correction based on the bias aberrations, then optimizing the correction with a parabolic fit.

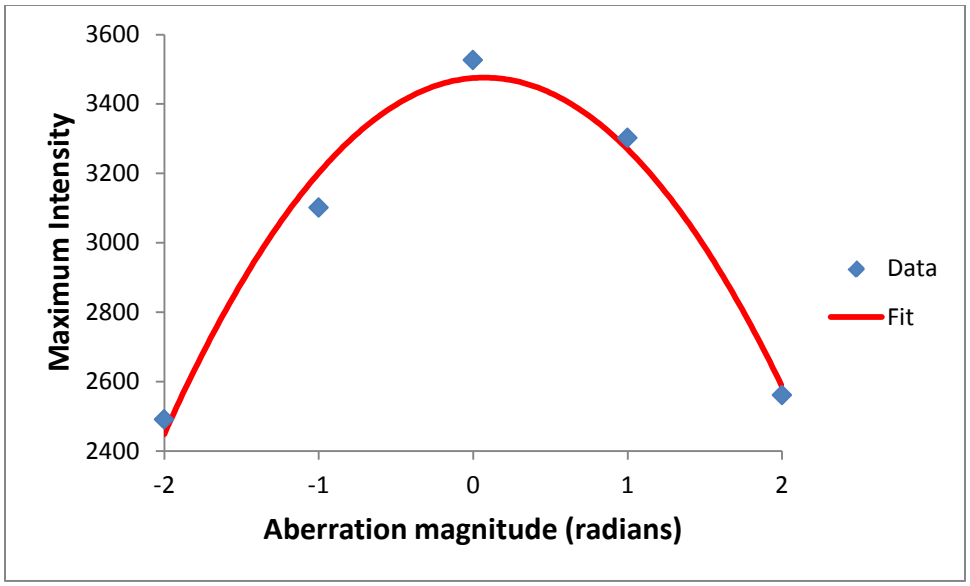

Figure 6.2: Parabolic fit example with intensity as the correction metric.

Maximum Intensity as a Correction Metric

Initial experiments were performed using 200nm microbeads fixed beneath *C. elegans* samples. Invitrogen yellow/green flourescent microbeads were diluted by a factor of 10^4 from their initial concentration and dried to the slide. Figure 6.3 shows one iteration of correction. All bead images are scaled to the intensity of the corrected bead (bottom right). As shown, the majority of aberration is due to astigmatism (Zernike modes 4 and 5). A 50% increase in the intensity is achieved through a single iteration of correction of the low order Zernike modes.

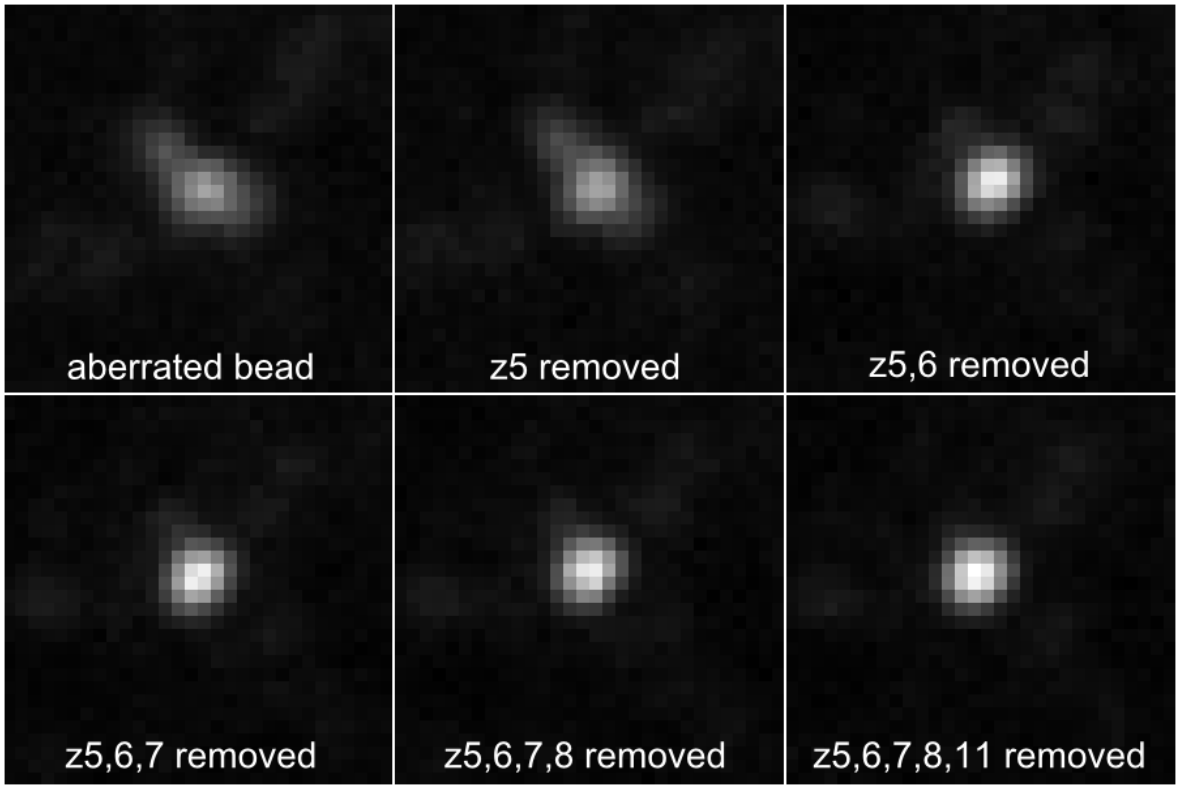

Figure 6.3: One iteration of AO correction of a 200nm fluorescent microbead fixed beneath a *C. elegans* sample.

In Figure 6.4 large field-of-view images of a mixture of 100nm and 200nm diameter microbeads fixed beneath a single worm are shown. A Differential Interference Contrast (DIC) image through the center of the worm is shown as Figure 6.4a. (DIC imaging will be discussed in depth in Chapter 7.) The edges of the worm can be seen in the bottom left and top right of the Figure 6.4. The worms axis runs vertically through the image. The measured diameter of the worm is 41µm. Figures 6.4b and 6.4c show widefield fluorescence images before and after four iterations of correction. As shown in the figures, AO

correction using the intensity of single 200nm bead near the center of the worm greatly improves a fairly large field of view of the beads.

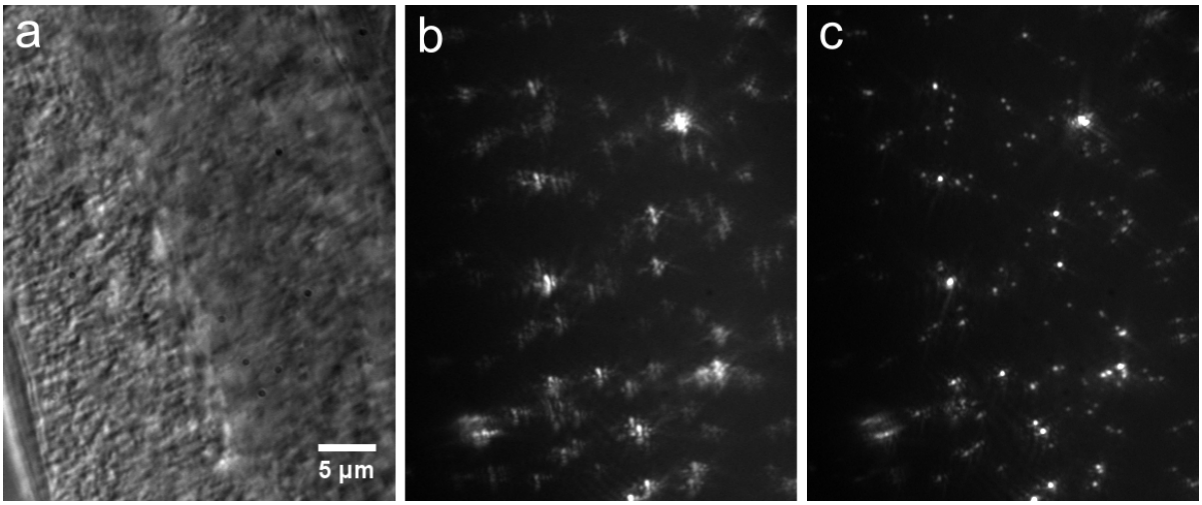

Figure 6.4: Correction of fluorescent microbeads fixed beneath a *C. elegans* sample. The worm orientation is shown in (a). The intensity of a single 200nm microbead is used as the correction metric. The microbeads before and after correction are shown as (b) and (c) respectively.

A concern with using AO with widefield microscopy techniques is that the correction will only apply to a small field of view. In Figure 6.5, the average bead intensity along the axis of the worm body is shown. The image slices run the entire width of the image in the horizontal direction and are 4.3µm thick in the vertical direction for Figure 6.5. The average bead intensity was calculated as the average of the top 5 pixel intensities for each slice. The average intensity increase is 120% along the axis of the worm, a distance of 42µm. The lateral improvement (relative to the worm axis) is investigated in a similar manner. Vertical slices run the entire vertical length of the image and are 3.4µm horizontally. The lateral improvement in bead intensity is shown as Figure 6.6. The average intensity improvement is 61%. Near the edge of the worm, beads become less aberrated, and thus are not improved by the centrally located correction.

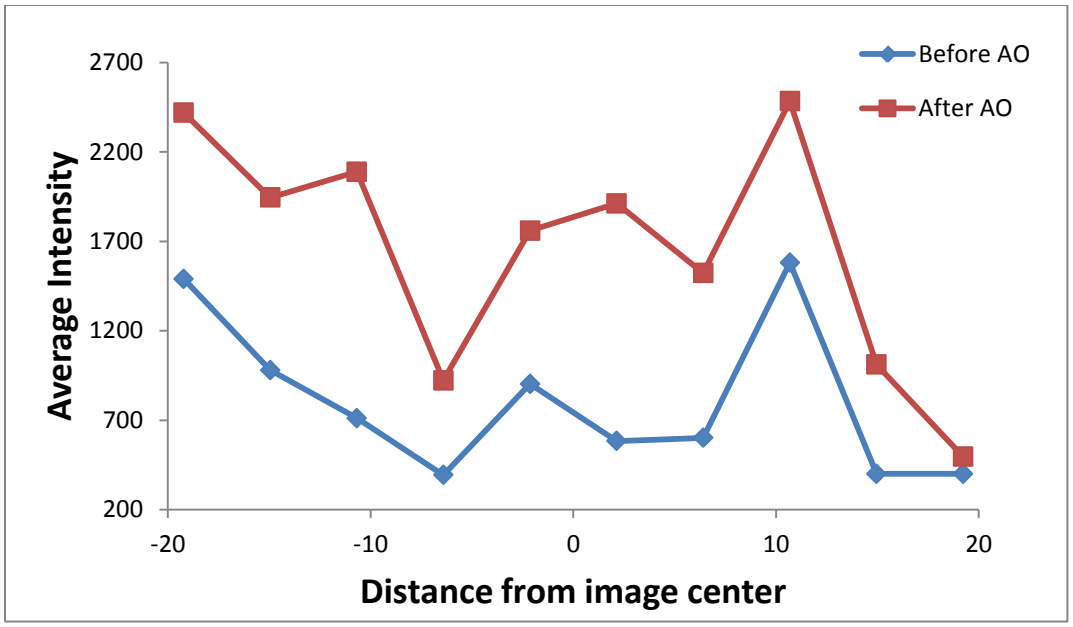

Figure 6.5: Intensity improvement along the axis of the worm with a single wavefront correction under the center of the worm.

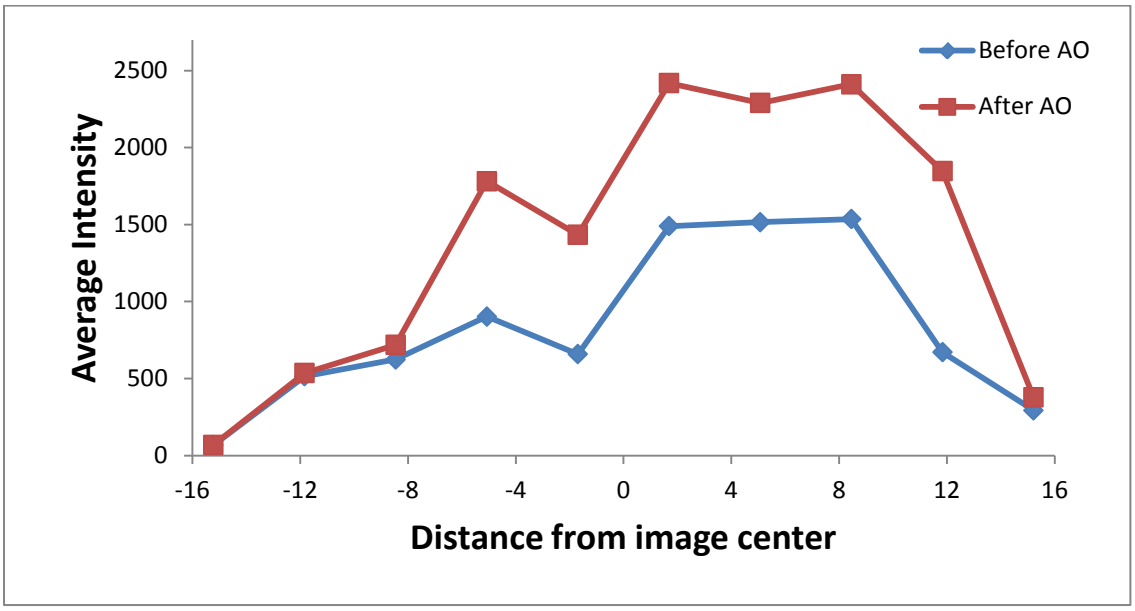

Figure 6.6: The lateral (relative to the worm axis) intensity improvement with a single correction under the center of the worm

Recording the magnitude of each Zernike represented aberration added to the system during correction allows total aberrations caused by the sample to be measured. This indirect form of wavefront measurement is demonstrated in Figure 6.7 which gives the aberrations added to the system to create Figure 6.4c. The specific magnitude of each Zernike mode is given as Table 6.1. As shown, the majority of aberration is astigmatism, which makes sense given the cylindrical shape of the worm body.

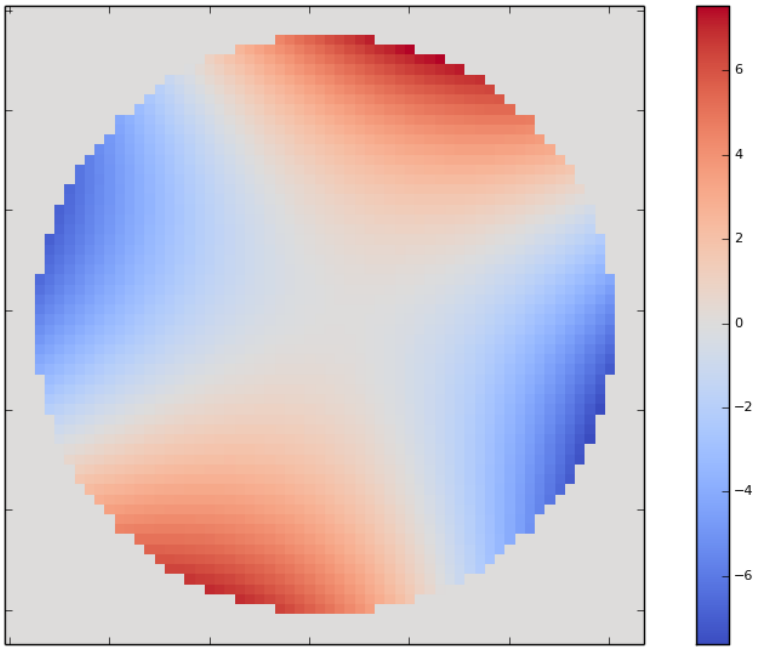

Figure 6.7: Wavefront compensation (in radians) applied to the system to correct for aberrations caused by the *C. elegans* sample in Figure 6.4.

Table 6.1: Magnitude of Zernike modes removed by the AO correction for Figure 6.7.

	z5	**z6**	**z7**	**z8**	**z11**
Magnitude	-5.74	-4.62	-.26	-.21	.17

SR-SIM system implementation

The implementation of super-resolution 2D SIM (SR-SIM), as presented by Gustafsson et al. [48], is presented here. Initially, an illumination pattern with a 6 pixel wavelength at the DMD was used. This resulted in a separation of the two beams of 3.6 mm at the mask and 12.6mm at the DM. With a reflecting surface diameter of 15mm, the illumination beams fit onto the DM, but are very close to its edge. The wavelength of the illumination pattern at the sample is 220 nm, which is very close to the diffraction limit of the system. As described by Gustafsson et al., the result will give near two-fold increase in the lateral resolution with SIM.

SR-SIM images were generated by illuminating the sample with the striped pattern rotated by 0, 120, and 240 degrees so that the resolution enhancement will be nearly isotropic. At each rotation, three images were taken at phase shifts of 0, $2\pi/3$, and $4\pi/3$ for a total of 9 images. SIM reconstruction is performed as described by Gustafsson and in Chapter 7. The separated frequency components are recombined with the generalized Wiener filter from Equation 3.13 [50]. The Wiener filter parameter is chosen to be 0.04% of the maximum frequency value so that noise is reduced, but resolution is not sacrificed. A cosine apodization function was used to help reduce ringing artifacts caused by the sudden drop off of the OTF at the extended resolution limit.

Initially, SR-SIM images of 200nm microbeads beneath a *C. elegans* sample were produced by removing aberrations with AO. Figure 6.8a shows a Differential Interference Contrast (DIC) image through the center of the worm. The bright feature on the left side of the image is the pharynx. Figure 6.8b and 6.8c show the widefield images of the microbeads before and after AO correction. The last to images, Figure 6.8d and 6.8e show the SR-SIM reconstructions with and without AO. As shown, the SR-SIM reconstructions show the intended enhanced resolutions. Without AO, the images of the beads are noisy and distorted, as shown in Figure 6.9, which gives an exploded view microbeads near the center of

the worm. A vertical profile through the beads in Figure 6.9 is given as Figure 6.10, and demonstrates a two-fold increase in the maximum intensity with AO, and a three-fold increase with AO-SIM. The full-width-half-maximum of the beads are 120nm. This data was submitted for publication, but ultimately rejected. The reported FWHM below the optimal diameter of the microbeads was found to be a problem with the reviewers. We attribute this discrepancy to fixing the microbeads with ethanol, which could damage the fluorophores on the surface of the microbead and thus reduce their fluorescing diameter. We also determined that the aberrations removed were not truly representative of the sample. The worms were mounted in glycerol, which leaches into the sample overtime and effectively reduces the aberrations (as glycerol has an index of refraction very close to the oil objective lens).

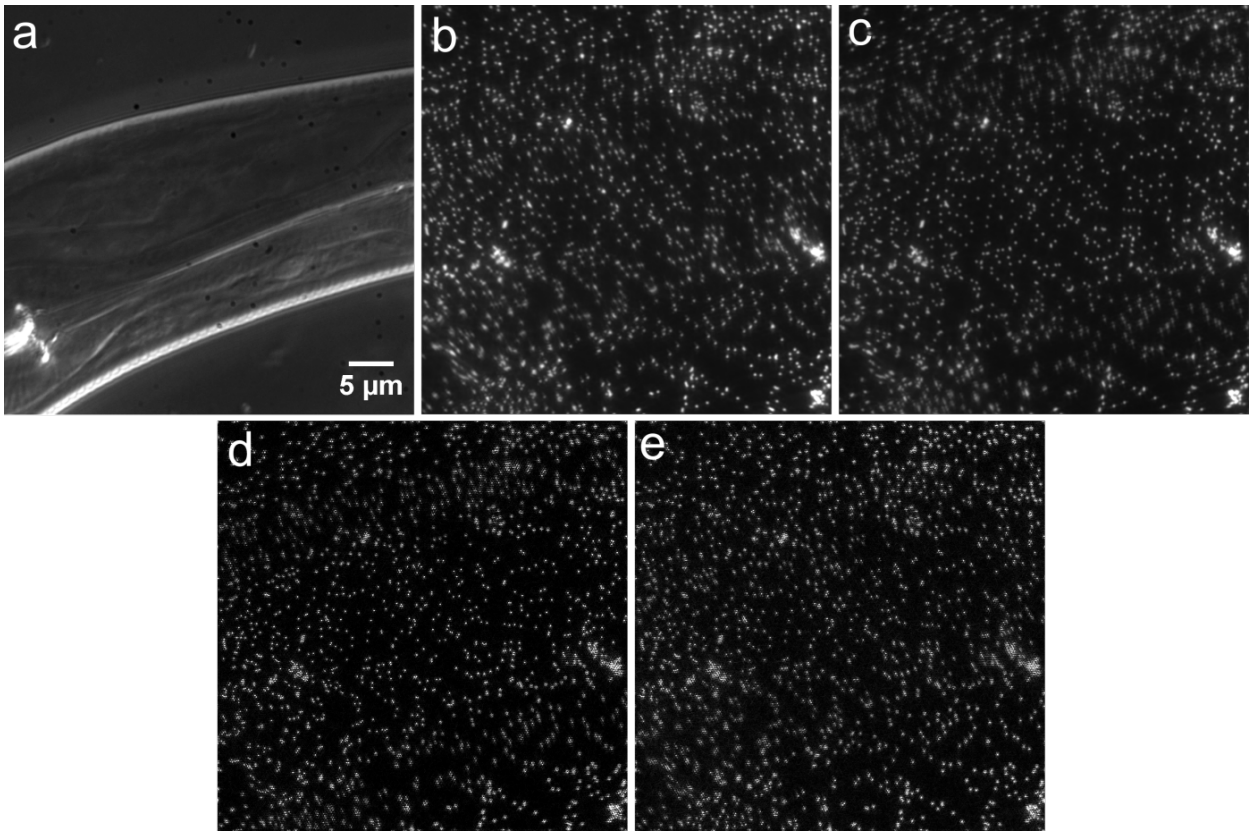

Figure 6.8: AO-SIM data with an old *C. elegans* sample. (a) Differential Interference Contrast image through the middle of a *C. elegans* sample. (b) 200nm microbeads fixed beneath the sample. (c) microbeads after correction. (d) SR-SIM reconstruction after correction with AO. (e) SR-SIM reconstruction without correction with AO.

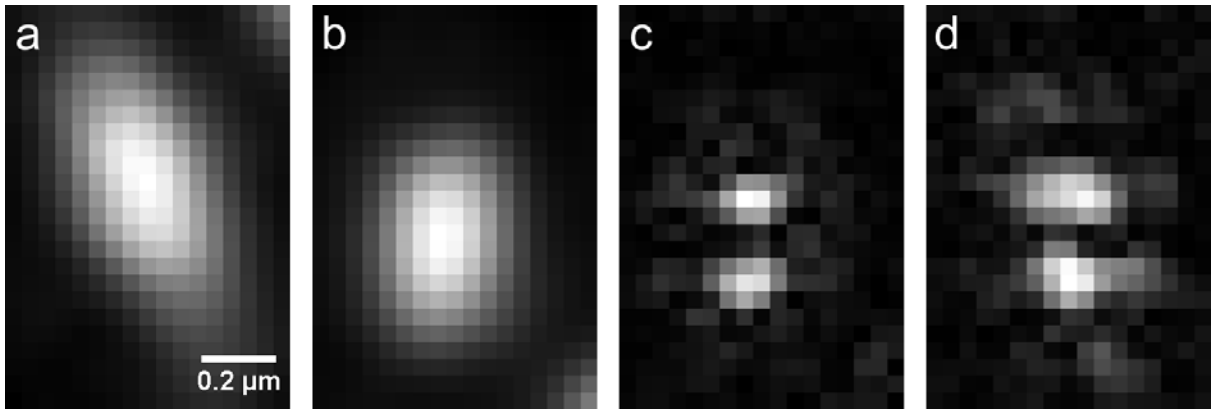

Figure 6.9: 200nm microbeads fixed beneath the center of the *C. elegans* sample (a) before correction with AO, (b) after correction, (c) SR-SIM reconstruction with AO and (d) without AO.

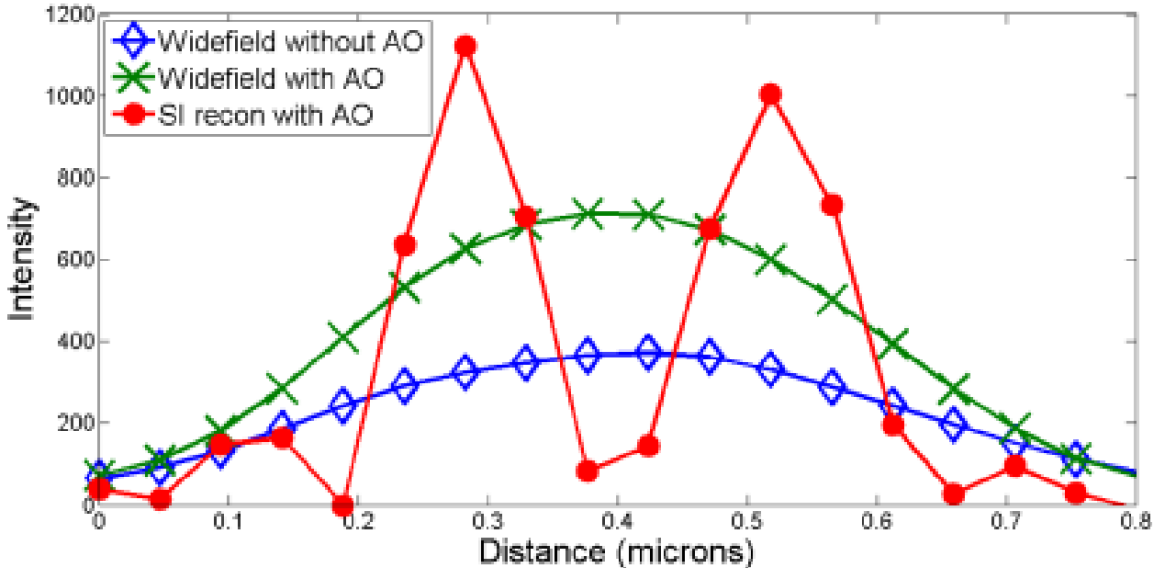

Figure 6.10: Profile comparison of the microbeads in Figure 6.9.

Through multiple trials of attempting SR-SIM on aberrative samples after correction with AO, it was determined that the majority of error in the shape of the DM occurs at its edges (this is apparent in Figure 8.7). Small amounts of aberrations to the illumination beams distort the illumination pattern and make SIM image reconstruction impossible. To address this issue, we initially replaced l4 with a 270mm focal length lens pair. This essentially magnifies the pattern, increasing its wavelength to 250nm at the sample. The separation of the illumination beams at the DM is thus decreased. Figure 6.11 compares the widefield and SR-SIM reconstructions with a 6 pixel pattern and l4=270mm. The FWHM of a microbead near the center of the image is 115 nm.

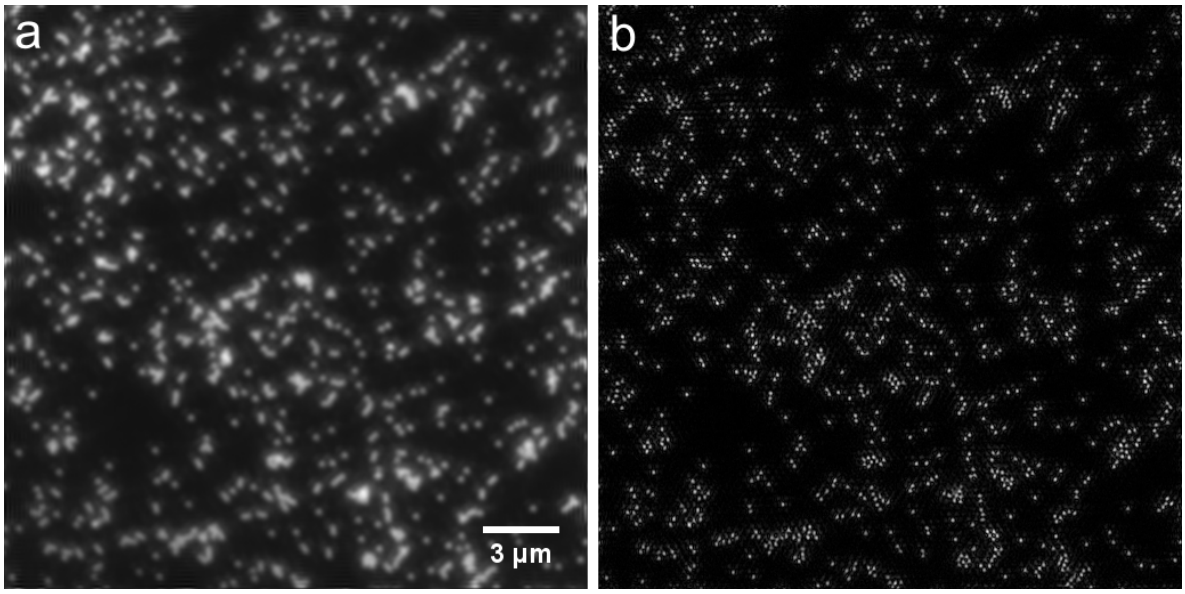

Figure 6.11: Widefield (a) and SR-SIM (b) images of 100nm diameter microbeads fixed to the coverslip. The wavelength of the illumination pattern is 250nm at the sample.

Further attempts to reconstruction SR-SIM data under aberrative samples were unsuccessful. An example of the problem is shown in Figure 6.12. In Figure 6.12a and 6.12b, the widefield images of 100nm microbeads fixed beneath a *C. elegans* sample are shown before (a) correction and after correction (b) with AO using the intensity of a single microbead near the center of the image as the correction metric. The attempted SR-SIM reconstruction of the beads after AO correction is shown as Figure 6.9c. The highly distorted reconstruction is due a loss of fidelity of the illumination pattern due to aberrations at the edges of the DM. This is apparent in Figure 6.13, which shows the angle (in radians) between the shifted and extended SIM frequency components (ϕ_i from Equation 3.14) for the 100nm microbeads fixed to the coverslip (Figure 6.11) and the microbeads under the *C. elegans* sample from Figure 6.12. As shown in Figure 6.13a, the distortion of the illumination pattern results in an inconsistent phase between the shifted and widefield components.

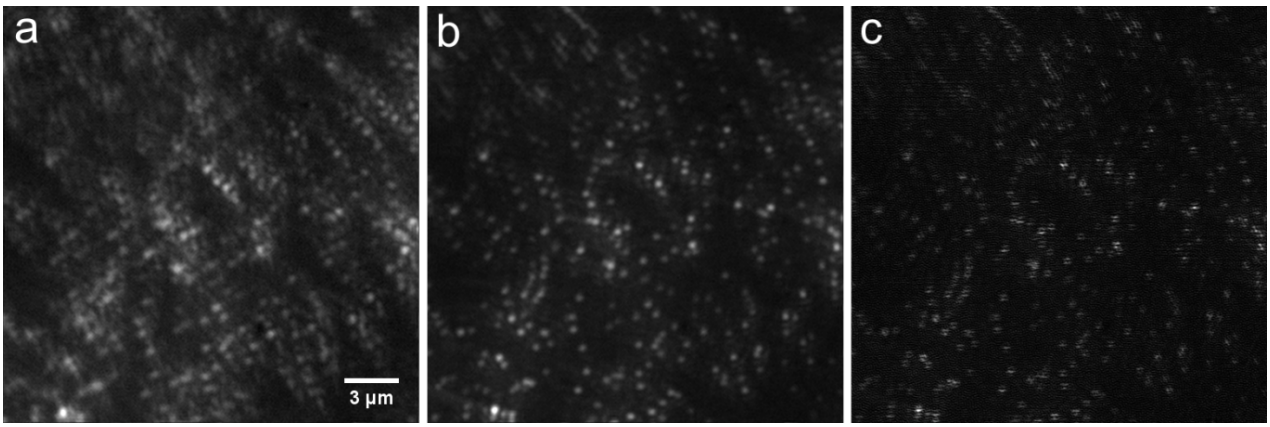

Figure 6.12: Widefield comparison of 100nm beads fixed beneath a *C. elegans* sample before (a) and after (b) AO correction with the intensity of a single bead as the correction metric. (c) shows the attempted SR-SIM reconstruction after AO. The distorted illumination pattern results in a distorted reconstruction.

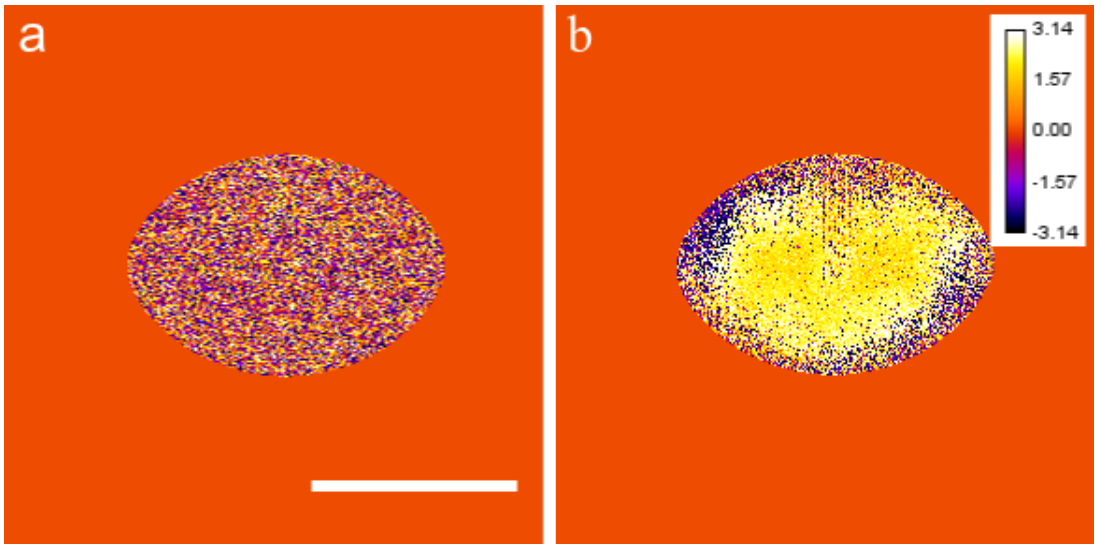

Figure 6.13: Angle (in radians) between the shifted and widefield SIM components, for the 100nm microbeads beneath a *C. elegans* sample (a) from Figure 6.9, and the microbeads attached to the coverslip from Figure 6.8. The horizontal and vertical axes are the k_x and k_y vectors in frequency space. The scale bar has a length of 2NA/λ.

After several attempts unsuccessful attempts for obtaining super-resolution images beneath an aberrative sample, we once again increased the pattern wavelength. An illumination wavelength consisting of 9 pixels at the DMD was used. Lens f4 was replaced by a 350mm lens. This resulted in a 2.8mm distance between the illumination beams at the mask and 9.8mm separation at the DM. The resulting wavelength of the pattern in image space is 290nm.

As an example of the 9 pixel pattern SR-SIM, the widefield and SR-SIM images of a mixture of 200nm and 100nm diameter microbeads fixed to the coverslip are shown in Figure 6.14. The widefield images were generated from the same data set as described by Equation 7.2 [73]. The 2D Fourier transforms of the widefield and SR-SIM images are shown in Figure 6.15. No apodization was applied so that the edges of the OTF support region could be easily visualized. As shown, the region of support of the frequency content has been greatly extended with SR-SIM. The OTFs have been scaled to enhance visualization of their boundaries.

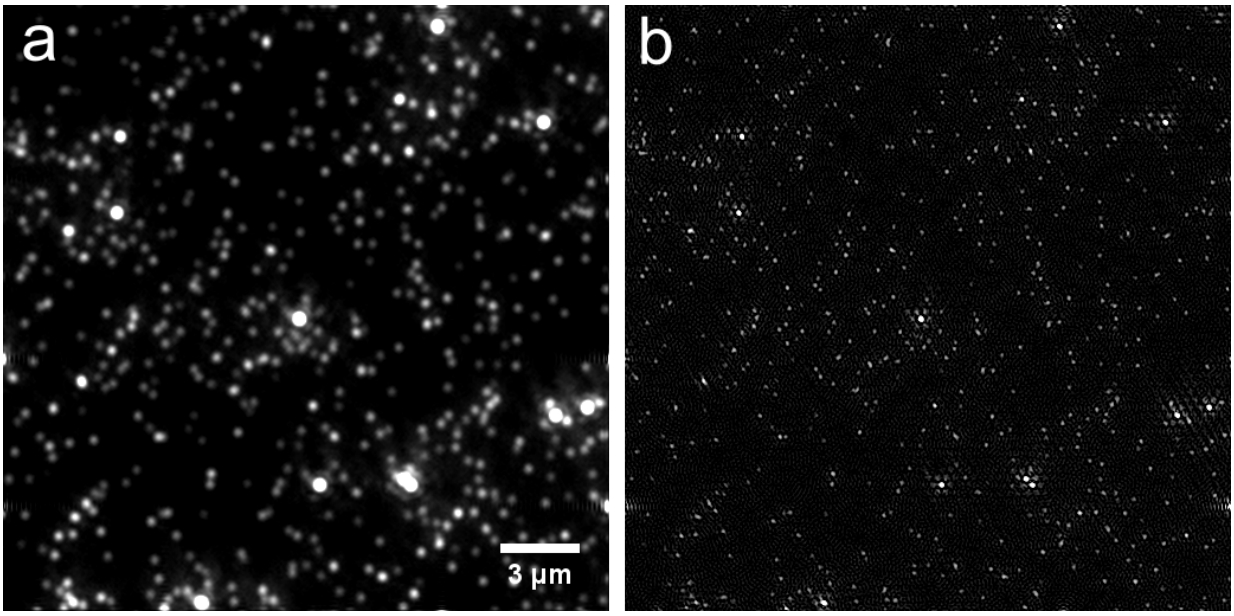

Figure 6.14: Widefield (a) and SR-SIM reconstructions of 100nm and 200nm microbeads.

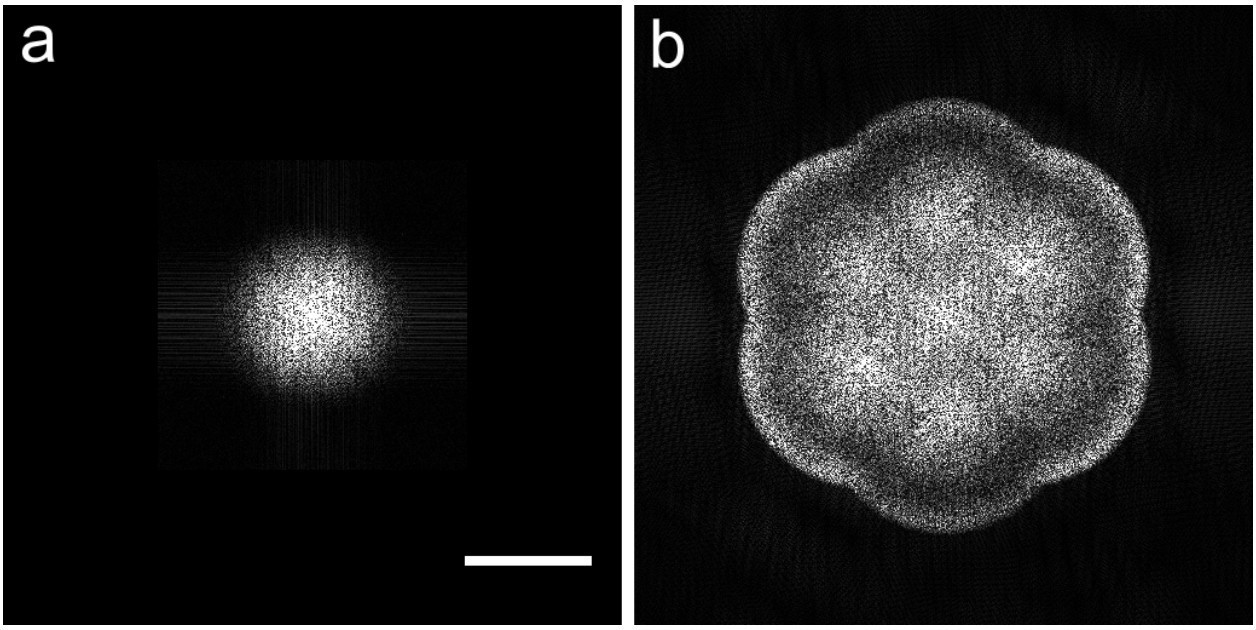

Figure 6.15: Fourier transform of the widefield (a) and SR-SIM images (b) in Figure 6.7. The scale bar has a length of 2NA/λ.

The vertical profile through a single 100nm diameter bead from Figures 6.14a and 6.14b is shown as Figure 6.16. To compare image intensities, the average background was first calculated and removed by subtracting the average intensity value from a dark area of the image. The bead under SR-SIM has a FWHM of 140nm and the intensity is nearly tripled.

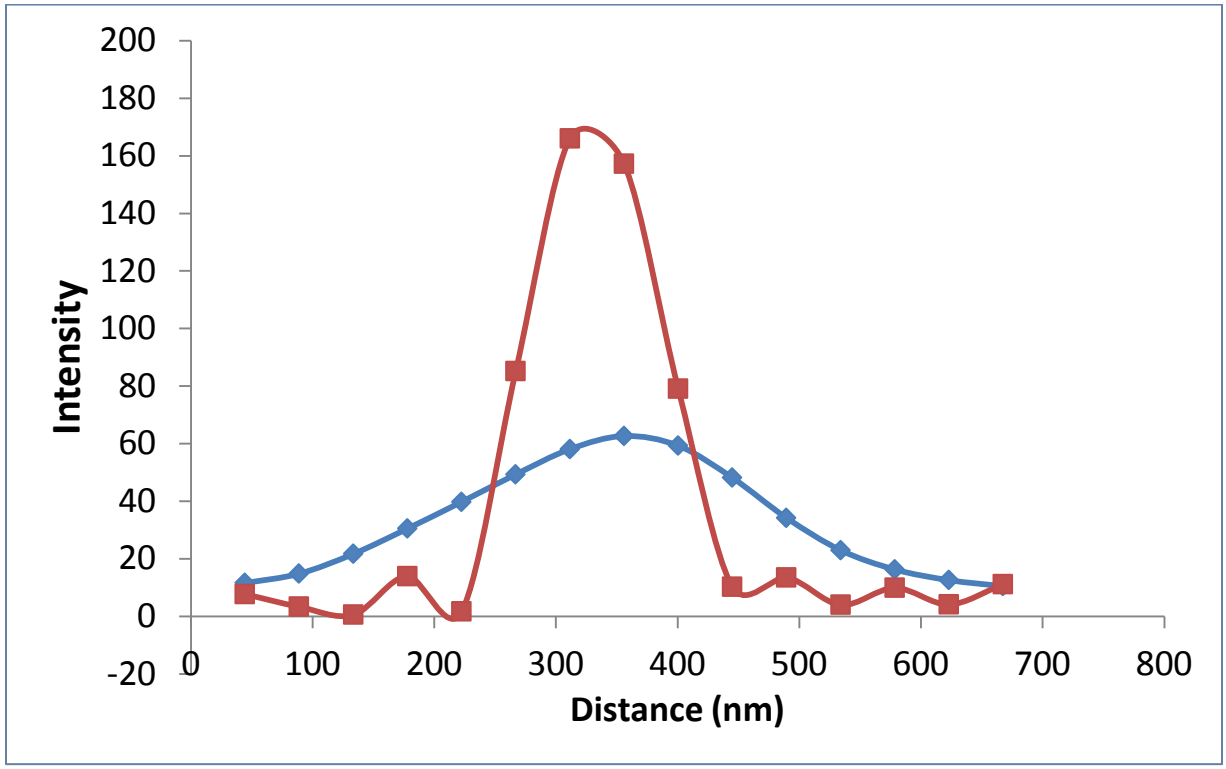

Figure 6.16: Vertical profile through a 100nm diameter fluorescent bead under widefield conditions (blue) and with SR-SIM (red).

AO-SIM

The AO-SIM system is demonstrated by producing sub diffraction limited images of fluorescent microbeads fixed beneath a *Caenorhabditis elegans* sample that is approximately 35µm in diameter. The super-resolution AO-SIM system produces 140nm resolution over a large field of view through thick tissue with only four iterations of aberration correction and SIM. To obtain deep-tissue, super-resolution images, AO correction is first performed as described at the beginning of the chapter. After removing the low order Zernike aberrations, SR-SIM is used to obtain images with extended resolution.

The results of the AO-SIM system were compared to widefield images before and after correction with AO as well as SR-SIM images without correction. In Figure 6.17, the images of fluorescent beads below a *C. elegans* are displayed. A DIC image through the center of the *C. elegans* that is approximately 35µm wide is shown in Figure 6.17a. Figures 6.17b and 6.17c show widefield images before and after correction. The last two images, Fig. 6.17d and 6.17e, show the SR-SIM reconstructed images with and without correction. As shown in the images, the SR-SIM reconstructions show an increased resolution. However, performing SR-SIM reconstruction without AO correction results in a highly distorted image of the microbeads with increased imaging artifacts. This is apparent in Figure 6.18, which shows an exploded view of 100nm diameter microbeads near the center of the image.

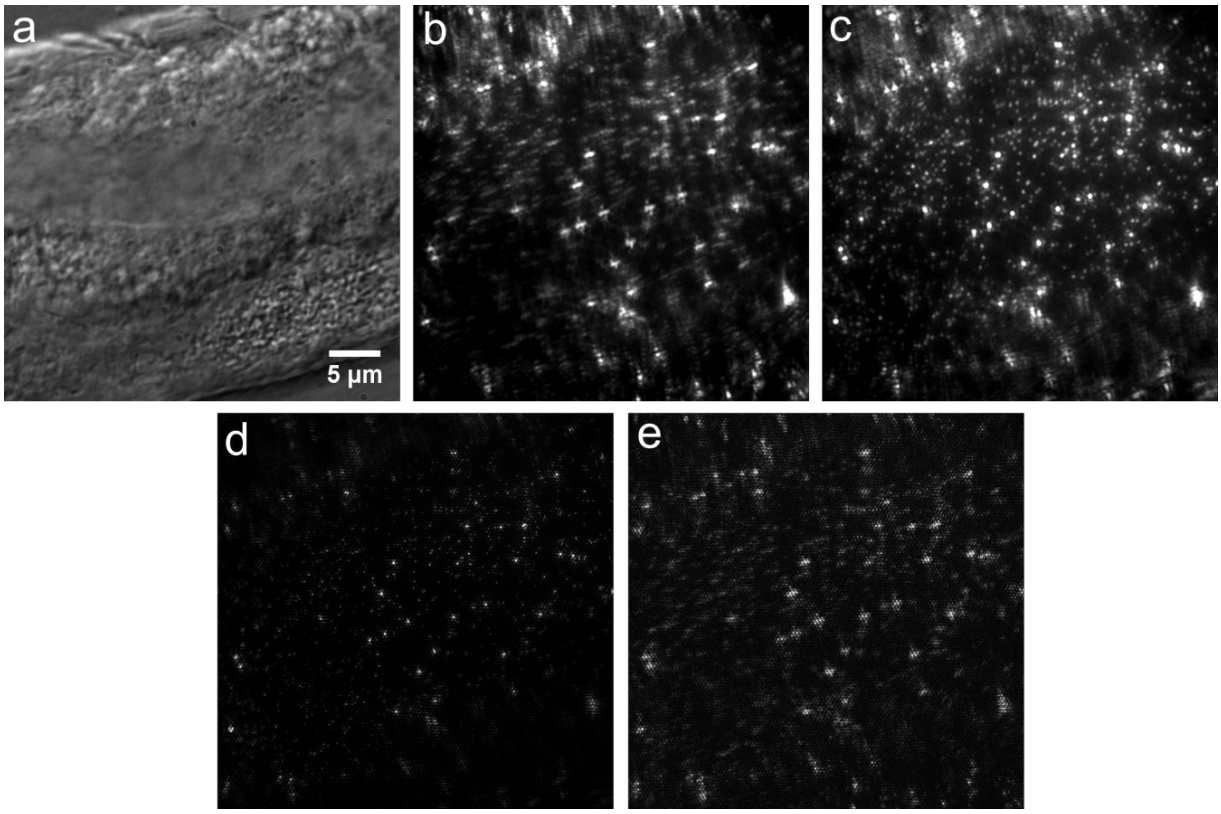

Figure 6.17: (a) Differential Interference Contrast Image near the anterior end of a *C. elegans* sample. (b) A mixture of 100nm and 200nm fluorescent microbeads fixed beneath the sample. (c) microbeads after correction. (d) SI reconstruction after correction with Adaptive Optics. (e) SI reconstruction without correction with Adaptive Optics

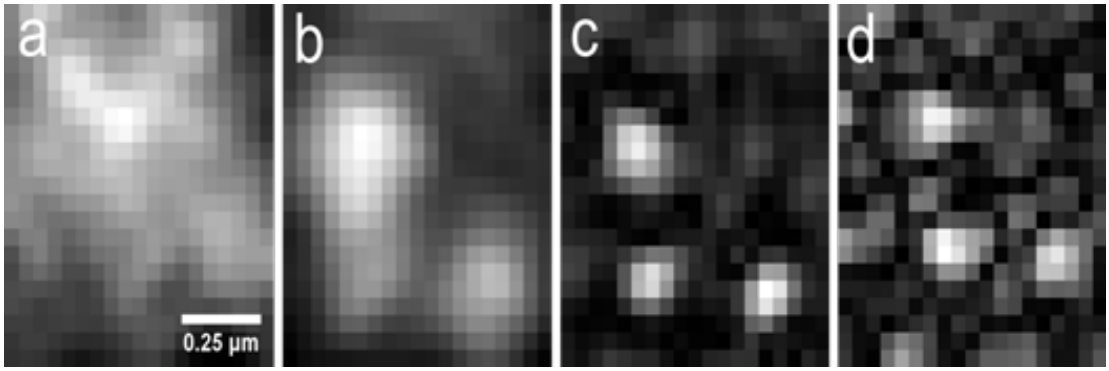

Figure 6.18: Invitrogen microbeads (100nm diameter) fixed beneath a *C. elegans* sample (a) before AO correction, (b) after correction, (c) SI reconstruction with and (d) without Adaptive Optics.

Without AO correction, the SR-SIM reconstruction of the beads is highly aberrated with increased noise around the beads. The increased noise is apparent in the frequency content of the bead images from Figure 6.17, shown in Figure 6.19. Without AO, the frequency content of the widefield image is highly distorted as the circular beads should have nearly uniform frequency content in both directions (as shown in the corrected widefield image, 6.19b). The frequency content of the SR-SIM images before and after correction are shown as 6.19c and 6.19d respectively. The widefield frequency contents are scaled to the same value for comparison, as are the SIM frequency images. As shown in Figure 6.19d, large amounts of high frequency noise exist in the reconstructed image without AO intervention. The aberration removed by the AO system to generate the corrected images is shown as Figure 6.20.

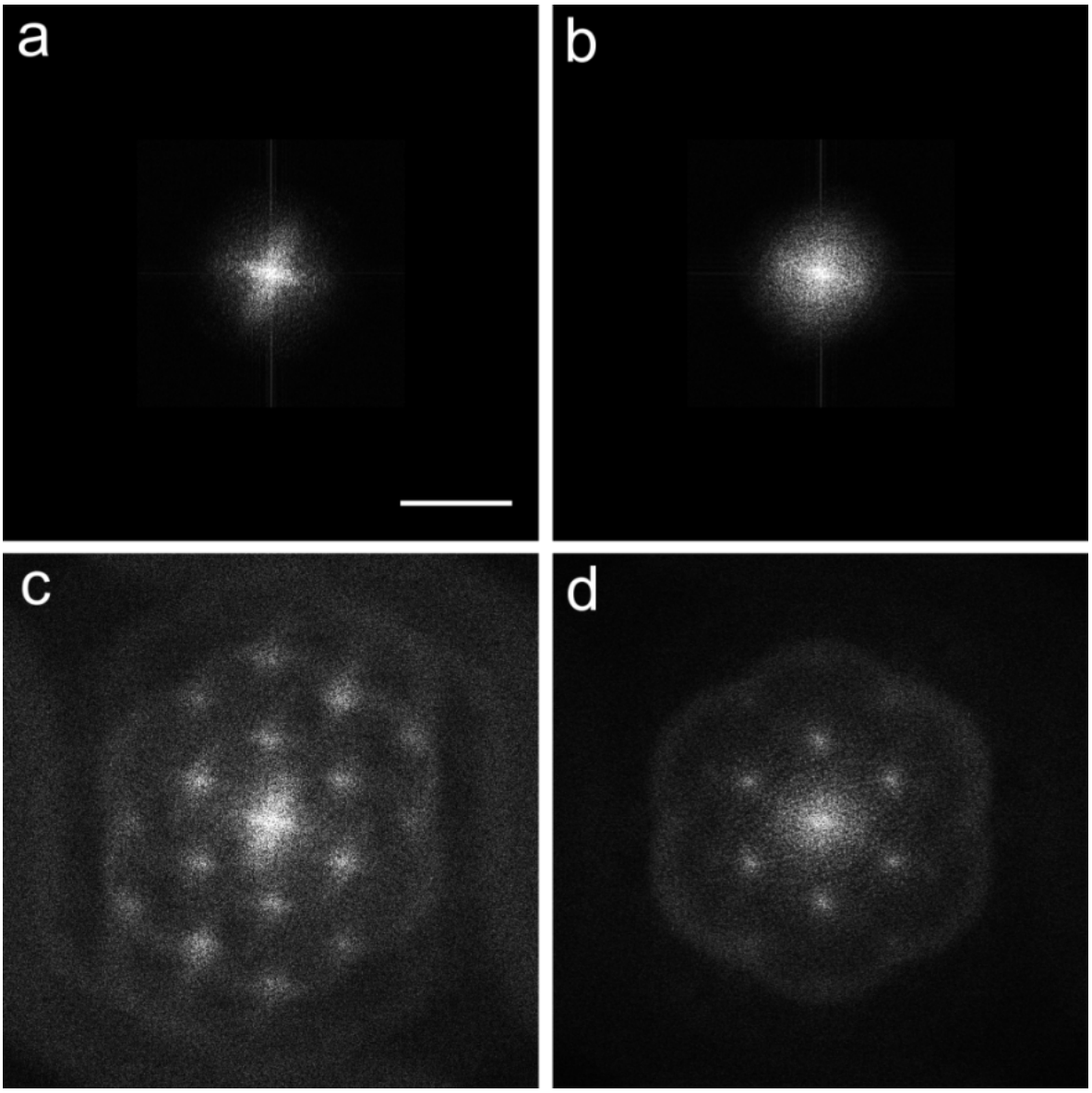

Figure 6.19: Fourier transform of the bead images in Figure 6.10. The frequency content of the widefield images without (a) and with (b) AO correction. The frequency content of the SIM images without (c) and with (d) correction. The scale bar in (a) has a length of $2NA/\lambda$.

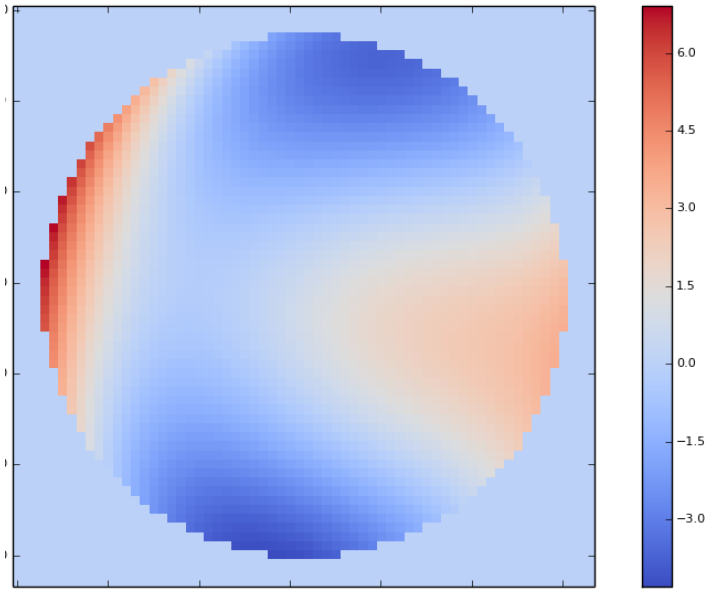

Figure 6.20: Aberrations removed by intensity based AO of microbeads under a *C. elegans* sample.

The SNRs of the SR-SIM images were calculated by taking the top five pixel intensities from a 128x128 area in the center of the image and the standard deviation of a 30x30 pixel background area. The SNR without AO correction is 100, with AO correction the SNR is 257. The graph in Figure 6.21 is a horizontal profile through the bottom two beads in Figure 6.18. The peak intensity is doubled by removing the aberrations with AO and quadrupled with SR-SIM when compared to the corrected widefield image. With AO and SR-SIM the measured full width at half maximum of the beads are 140nm and 130nm.

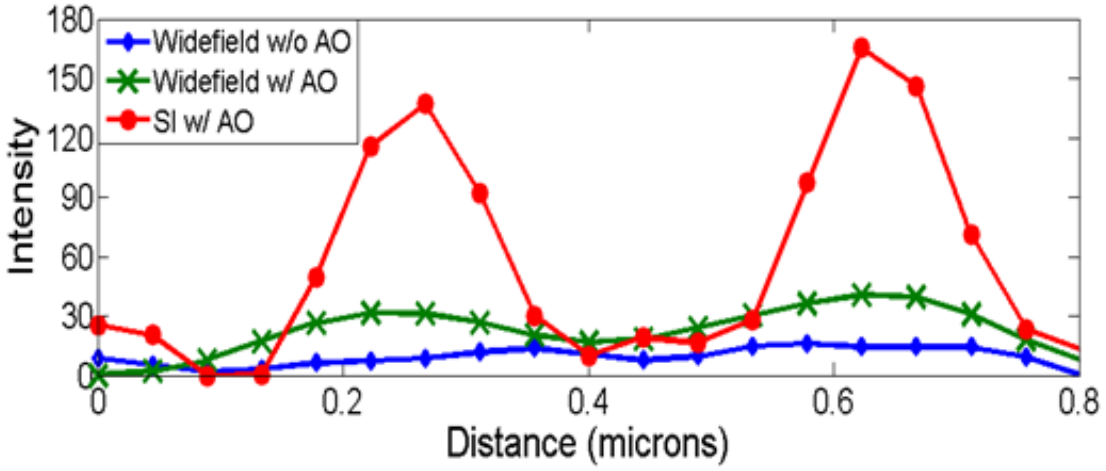

Figure 6.21: Profile comparison of two close microbeads (200nm diameter) fixed beneath a *C. elegans* sample.

To demonstrate the field of view obtained with a single correction, the average bead intensity laterally across the worm body is plotted. The average of the top 5 pixel intensities for each slice, which were 4.3µm x 22µm in this case, were recorded and plotted (shown as Figure 6.22). The average intensity increase is approximately 60% across the width of the worm. This average includes the top and bottom of horizontal slices of the image in which many microbeads are not under the worm. Along the worm axis, the improvement extends over 35 µm, near the entire range captured by the imaging camera. In Figure 6.23, we show images of 100nm diameter beads near the edge of the worm (about 10µm from the worm center) before and after correction with AO as well as the corresponding SR-SIM reconstructions.

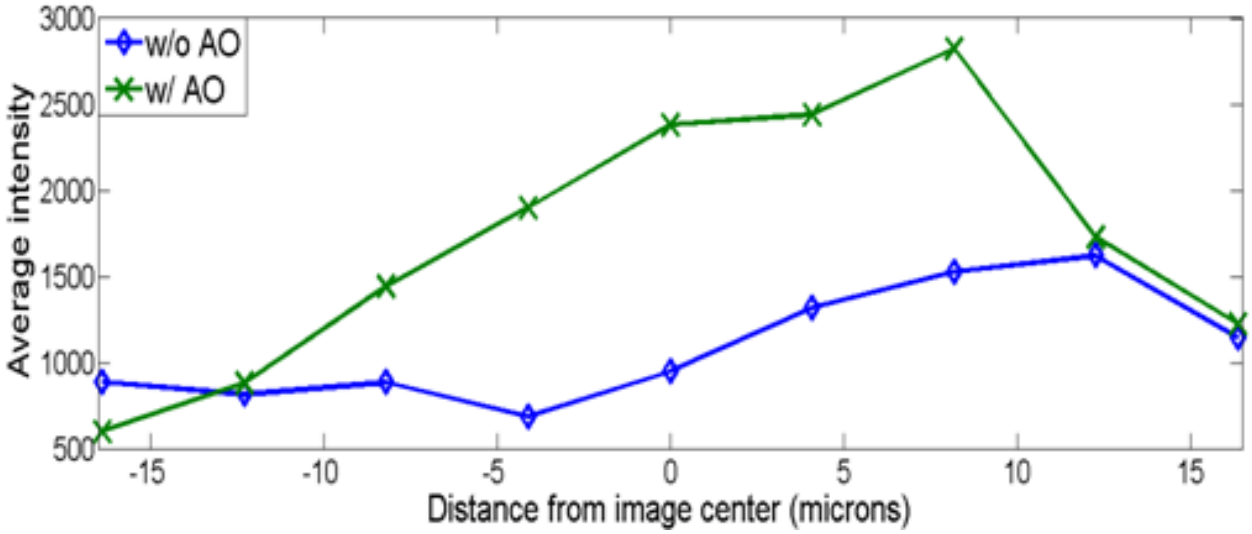

Figure 6.22: Average bead intensity across the C. elegans sample

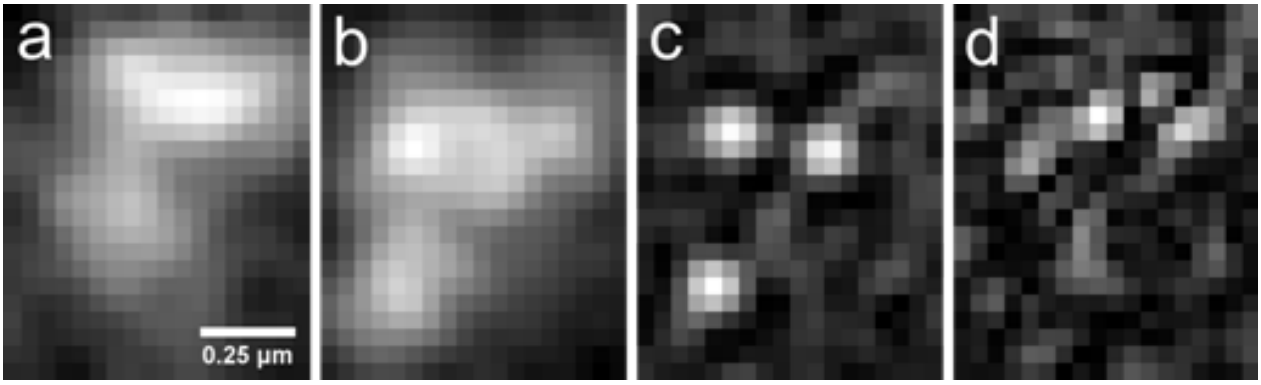

Figure 6.23: Microbeads near edge of *C. elegans* body (a) before AO correction, (b) after correction, (c) SR-SIM reconstruction with AO, and (d) SR-SIM reconstruction without AO.

Chapter Conclusion

In conclusion, AO-SIM is a powerful combination that is capable of producing super-resolution images through thick tissue. These experiments have demonstrated a microscope system that provides resolution beyond the diffraction limit through thick tissue by combining Adaptive Optics and Structured Illumination Microscopy. A resolution of 140nm through 35µm of tissue can be achieved. AO-SIM increases the peak intensity and AO increases the SNR of SIM by 150%. One criticism of the combination of AO and widefield microscopy techniques is that the field of view over which the image can be corrected will be small compared to the size of the captured images. Whereas, with scanning microscopy techniques, the aberrations can be corrected, at least in principle, on a point by point basis. The figures in this chapter show that four iterative corrections at a central location greatly improves the image quality of the SR-SIM image over a 35µm by 20µm field-of-view. In the event that the corrected field of view is not large enough, different corrections can be applied for different areas of the image, and the images could be combined by image fusion [78]. Multi-conjugate AO can also be used to increase the corrected field of view [15]. This work is an important step towards super-resolution *in-vivo* imaging using AO and SR-SIM.

To validate the usefulness of wavefront correction using the intensity of a fluorescent microbead, the improvement of DIC images of *C. elegans* is also demonstrated. Samples are prepared and corrected as describe above. After removal of aberrations using intensity based AO, DIC images at the bottom of the worm were acquired and compared before and after correction. The images of the aberrated bead before correction and after correction of the low order Zernike modes are shown as Figures 6.24a and 6.24b respectively. The increase in maximum intensity after a single iteration is 135%. Figure 6.24c and 6.24d show DIC images of dense bodies located on the bottom surface of the worm before and after correction. Dense bodies anchor the bands of striated muscle that run along the body of the worm. They

not only provide a necessary mechanical linkage, they are also involved in the complex signaling process that coordinates movement between different muscle bands. The striated muscle function is similar in vertebrates and invertebrates. Specifically, striated muscle function in *C. elegans* is similar to skeletal muscle function in humans. As shown in the Figure 6.24c, aberrations degrade and elongate the image of the dense bodies.

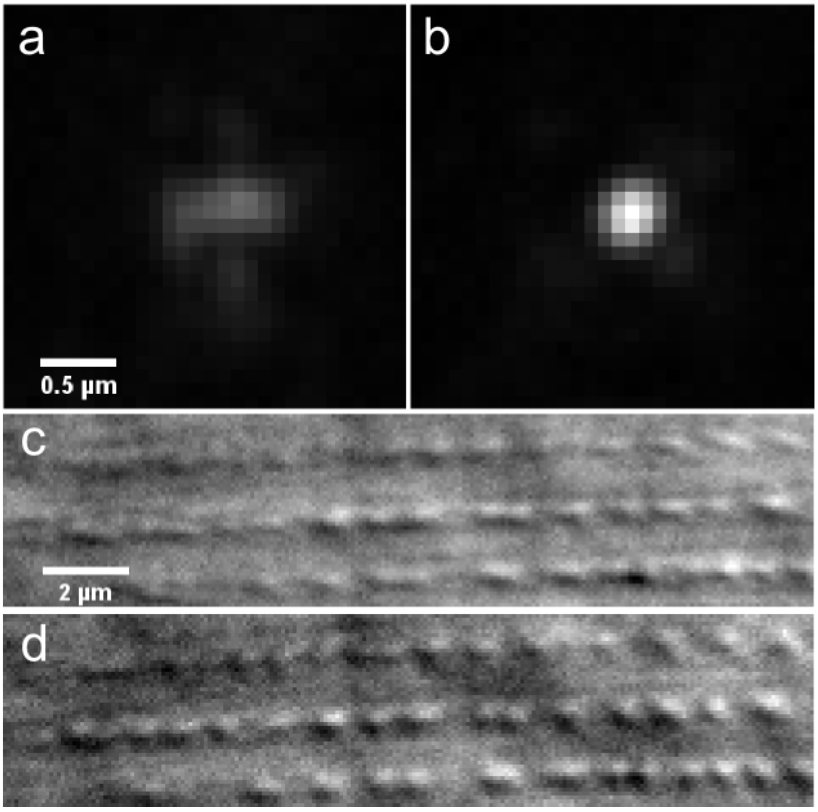

Figure 6.24: Improvement of DIC images of dense bodies at the bottom of a *C. elegans* using the intensity of a 200nm fluorescent microbead fixed beneath the sample as the correction metric. The widefield images of the bead before and after correction are shown as a and b respectively. The DIC images before and after correction are shown in c and d.

Chapter 7: Adaptive Optics for Differential Interference Contrast microscopy

Producing corrected DIC images is an important, and to our knowledge unreported, application of Adaptive Optics. DIC microscopy is an important biological imaging technique which images the refractive gradient in the sample. Because most biological samples are transparent, DIC is a powerful technique for imaging that does not require special sample preparation. DIC also requires a much lower light exposure than fluorescence microscopy. DIC has been used in developmental biology to image developing *C. elegans* [79] and zebrafish embryos [80], but the loss of resolution that occurs as the embryo grows larger has limited its utility.

In the previous chapter, the improvement of DIC images using fluorescence microbeads and intensity based AO was demonstrated. Here we take the opposite route and show that image based correction using DIC microscopy can be used to effectively optimize the wavefront with sensorless AO using a much lower overall light exposure than sensorless AO with fluorescence images. The shape of the DM is optimized using sensorless AO with low frequency content of the image as the correction metric as described by Debarre et al. [43]. This significantly reduces the photobleaching and sample

damage during wavefront optimization. After the wavefront is optimized, either fluorescence or DIC images of the sample can be captured.

The effect of aberrations on DIC microscopy has been explored by Preza and Conchello [81]. They compared DIC microscopy images of latex beads with simulations and were able to reproduce spherical aberrations in the experimental results with a phase mask introduced into the back pupil plane of the objective in the simulations. Thus, aberrations will affect DIC images in a similar manner to fluorescence microscopy and can be corrected in the back pupil plane.

Aberrations and DIC Microscopy

In Fig. 7.1, we simulate the effects of different aberrations on the DIC point spread function (PSF). In Nomarski DIC, the Fourier spectrum of the sample transmission function, $t(x, y)$, is modulated by $2j\sin(2\pi\bar{k} \cdot \bar{\Delta} - \phi)$ where $\bar{\Delta}$ is the shear which is typically chosen to have a magnitude of $\sim\lambda/4\text{NA}$ [82]. For the case of perfectly incoherent imaging, the modulated transmission is then filtered by the incoherent OTF. The incoherent OTF is the autocorrelation of the back pupil plane, and the aberrations are represented as phase distortions in the back pupil plane. Figure 7.1 shows the aberrated back pupil planes in the first row. The second row shows the DIC image of a point phase object, and the third row shows the Fourier Transform of the point object which is the effective OTF of the aberrated DIC system.

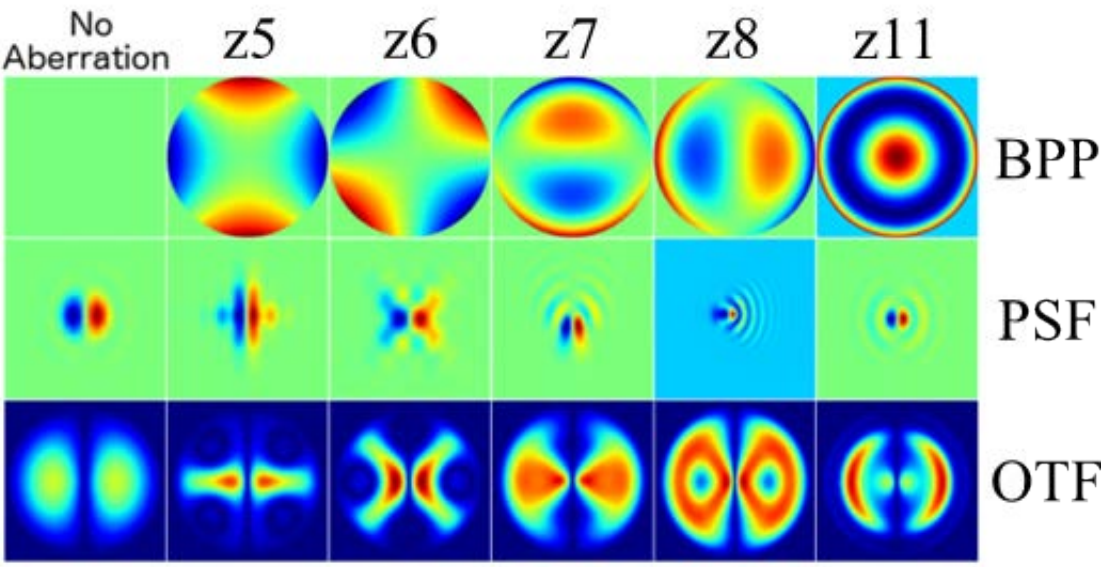

Figure 7.1: Effect of aberrations of DIC imaging. (a) top row. Aberrations applied to the phase of the back pupil plane of the imaging system. Z5 and Z6 are astigmatism. Z7 and Z8 are coma, and Z11 is spherical aberration. (b) Second row. Corresponding DIC images of a 0.1 radian point phase object. (c) Fourier Transform of row (b), the effective OTF. The Zernike modes are labeled according to the Noll ordering, and the magnitude of each aberration is 1 radian RMS.

Image based AO – the Fourier ring metric

As can be seen in Figure 7.1, all the aberrations have a marked effect on the PSF and OTF regardless of shear direction. As a metric for sensorless AO, we choose a Fourier ring filter as shown in Figure 7.2 which will probe the change in the OTF with the aberrations [83][83][83][82]. The metric, which will be referred to as the Fourier ring metric, is defined as $g = \iint R\left|\tilde{I}(u,v)\right|dudv$ where R is the filter shown in Figure 6.9. The radius and width of the ring are chosen experimentally to maximize the change in metric with change in aberration at high signal level. If the filter radius is too close to 2NA/λ, the signal is too low and if it is too close to 0, the change with aberrations is too small. Using inner

diameter of 0.49 NA/λ and outer diameter 0.68 NA/λ for the Fourier ring metric provides a well behaved response for the Zernike modes shown in Fig. 7.1, as shown in the simulations in Figure 7.3.

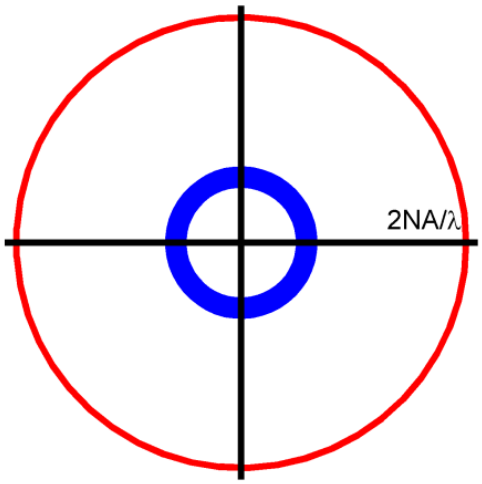

Figure 7.2.: Fourier ring filter. The blue area represents the band passed region. The red ring represents the edge of the conventional OTF region of support

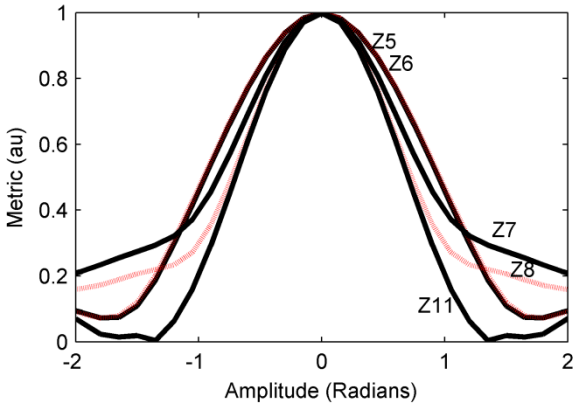

Figure 7.3: Simulated response of the image frequency content metric to bias aberrations.

Aberrations are removed as described in Chapter 6, by applying an initial correction based on bias Zernike aberrations, and then performing a parabolic fit to refine the correction. A 128x128 pixel area (11.3x11.3μm) area of the image is chosen for correction, this allows a specific feature to be studied. The Fourier transform of the 128x128 area of interest is filtered by the Fourier ring and the sum is used as the correction metric.

Initial testing of this correction scheme was performed by inducing aberrations with the DM when imaging 500nm latex microbeads fixed to the coverslip. An image of a latex bead aberrated by a magnitude of 3 radians of astigmatism (z5) is shown before and after correction in Fig. 7.4. While the background noise level is the same in these images, the contrast of the bead image increases by a factor of 6.75 after correction. The correction shown in Fig. 7.4, requires 25 images. Each DIC image illuminates the sample with an intensity of 0.12 W/cm2 over a 100ms exposure time. Figure 7.5 shows the frequency content metric of the aberrated bead under bias aberrations for z5. As shown in the figure, the metric value increases from 9.5 to 18 near -3 radians, the expected correction value.

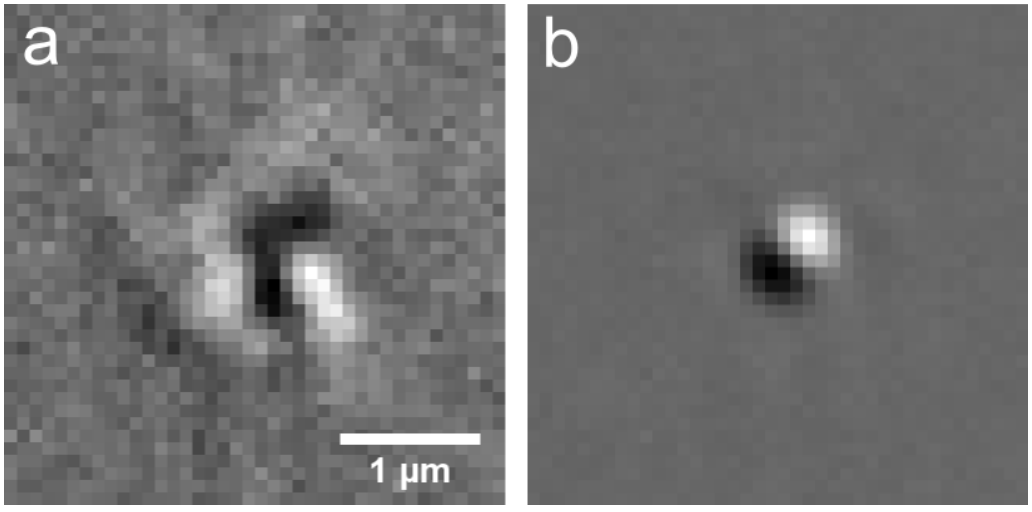

Figure 7.4: A single 500nm diameter latex microbead with induced astigmatism (a) and after correction (b) using the Fourier ring metric

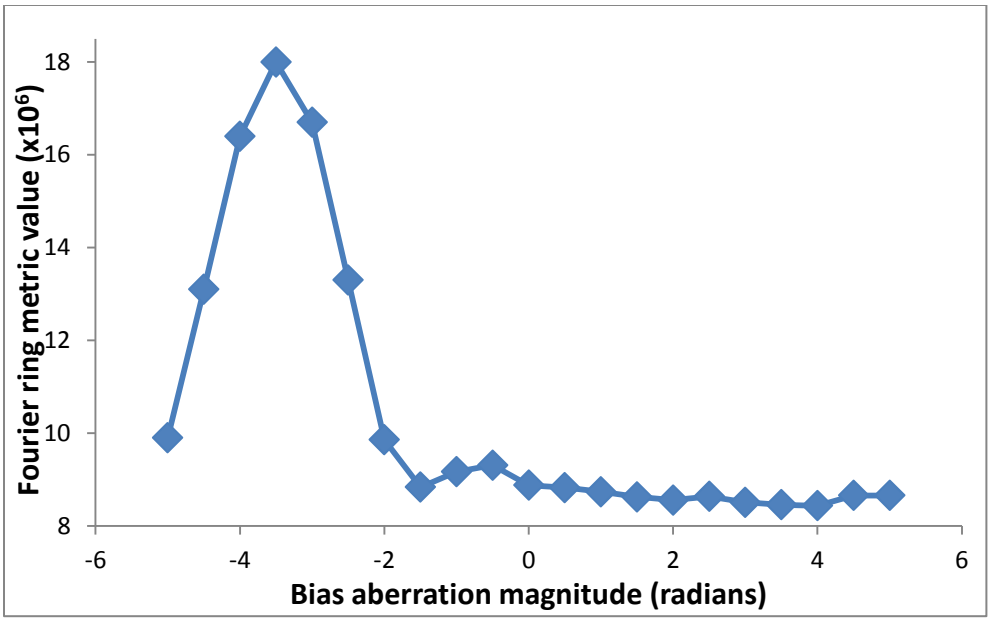

Figure 7.5: Response of the Fourier ring metric for a latex microbead under bias aberrations. A 3 radian magnitude astigmatism aberration was induced by the DM prior to acquisition.

Image based AO correction of sample induced aberrations

To demonstrate correction using DIC image based AO for wavefront correction and improvement of fluorescence intensity, a 15µl mixture of 500nm diameter latex microbeads diluted by 10^4 and 200nm diameter yg microbeads diluted by 10^3 in ethanol was dried on a slide. Worms were then applied on top of the microbeads as described in Chapter 4. Figure 7.6 shows an increase in intensity for fluorescence microbeads fixed beneath a *C. elegans* sample after correction using the Fourier ring metric with sensorless AO on latex microbeads. Figures 7.6a and 7.6b show the latex microbeads before and after correction. A total of two correction iterations were performed. The images of the fluorescent microbeads before and after correction are shown as Figures 7.6c and 7.6d respectively. Figure 7.7 shows a vertical profile through a single bead near the center of the image before and after correction. A 4x

increase in intensity of the fluorescence microbeads was achieved with the Fourier ring metric on DIC images of latex microbeads.

The wavefront compensation applied to the latex microbeads fixed beneath the worm over two iterations is shown as Figure 7.8. The wavefront aberration measurement looks strikingly similar to the results obtained using intensity based correction, in that it is dominated by astigmatism.

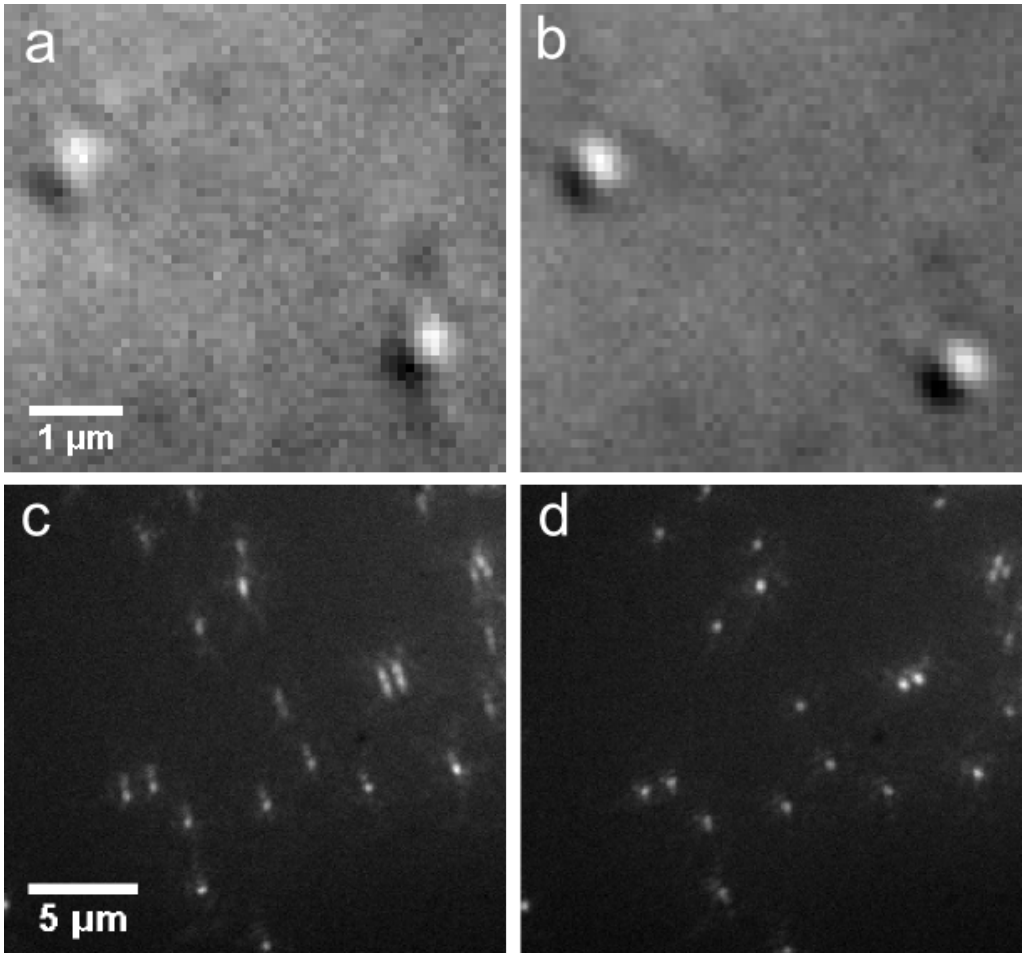

Figure 7.6: Intensity enhancement of fluorescence microbeads fixed beneath a worm by using Fourier ring metric AO on DIC images of latex beads. The 500nm latex beads before and after correction are shown as (a) and (b) respectively. Images of 200nm yg fluorescent beads before and after correction are shown as (c) and (d).

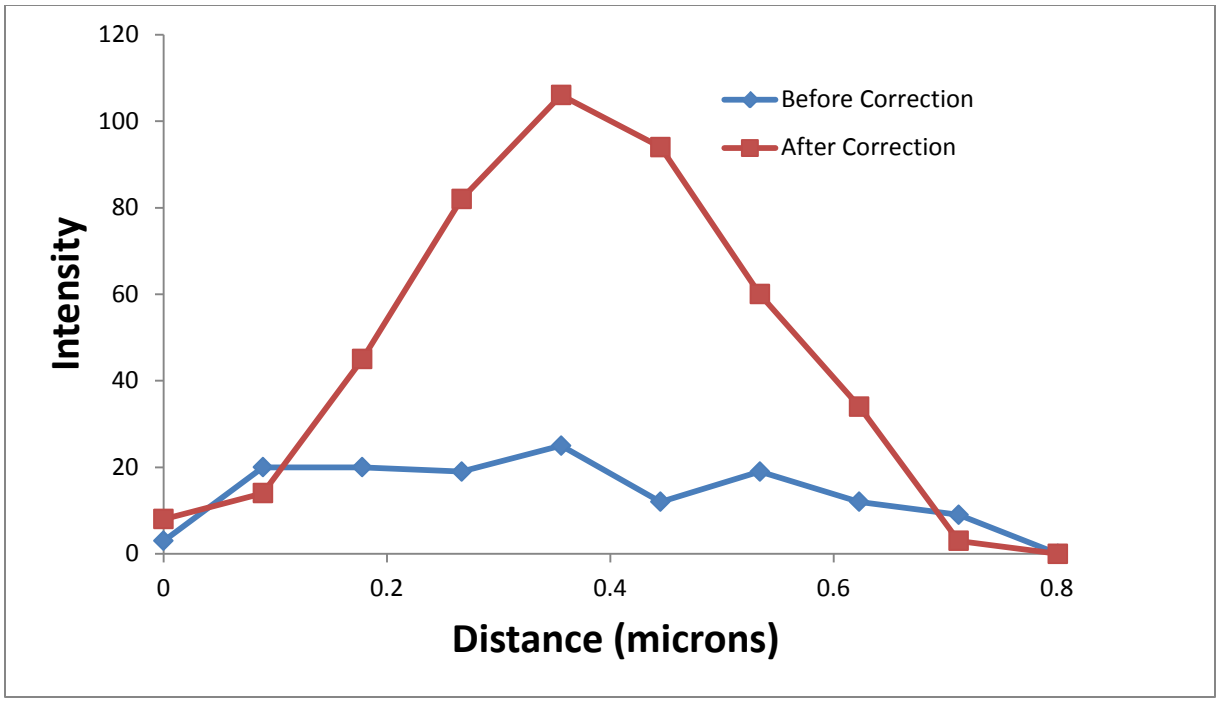

Figure 7.7: Vertical profile through a centrally located 200nm fluorescence microbead before and after correction with Fourier ring AO.

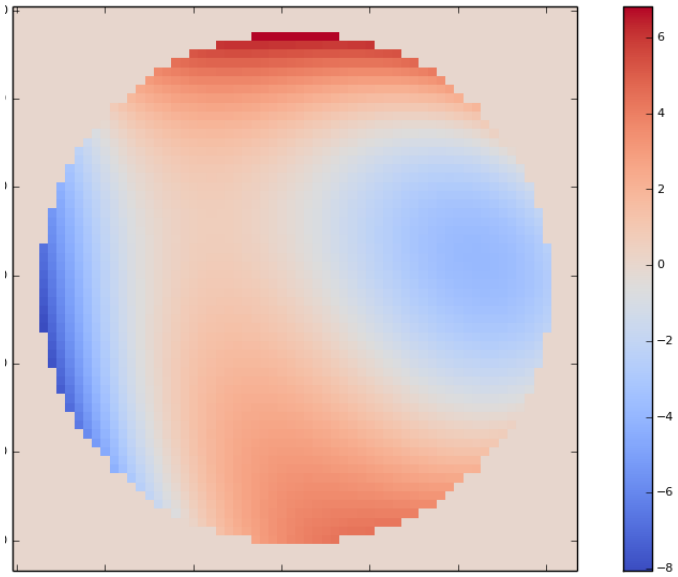

Figure 7.8: Aberrations (radians) caused by a *C. elegans* sample which were removed to create Figures 6.12b and 6.12d.

Although latex microbeads could be injected into a sample to act as the "guide stars" images for AO correction, a simpler setup would be to use the image content of the sample for correction. In Figures 7.9, 7.10, and 7.11 we demonstrate image based AO correction of biological specimens. Figure 7.10 shows dense bodies (top left) midway through a *C. elegans* sample before and after correction. As shown in the Figure, aberrations degrade the image of the dense bodies, making them indistinguishable without AO. Figures 7.10 and 7.11 show unknown features from *Drosophila melanogaster,* or fruit fly, embryos. These samples were provided by Cordula Shultz's Lab in the Department of Cellular Biology at UGA. As shown in the figures, the images are improved with AO correction.

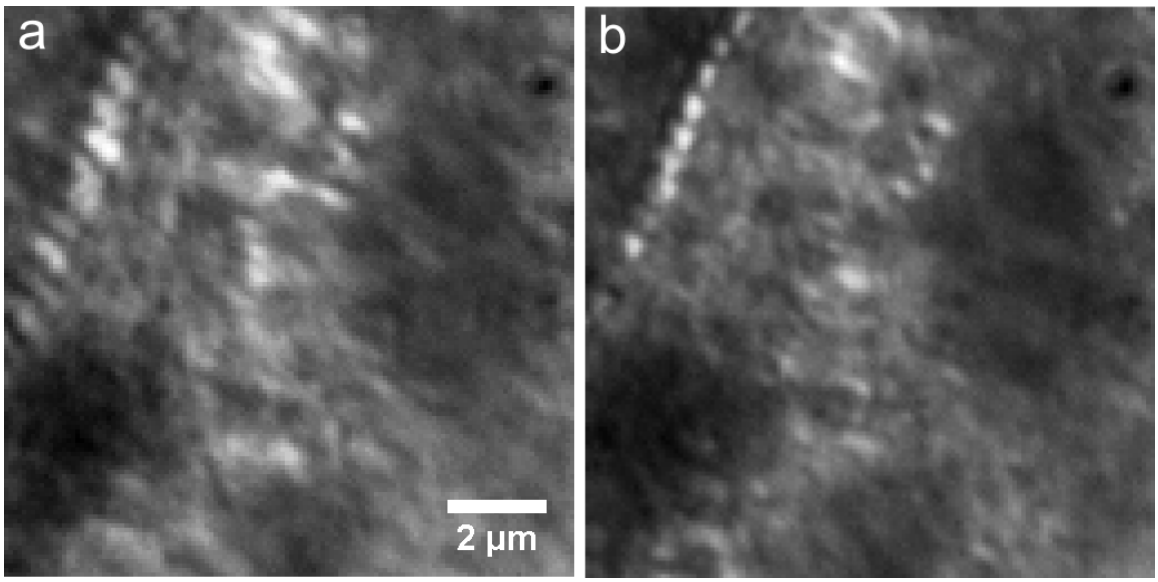

Figure 7.9: Image based Adaptive Optic correction of *C. elegans* muscle tissue. The features at the top left of the before (a) and after (b) correction images are dense bodies.

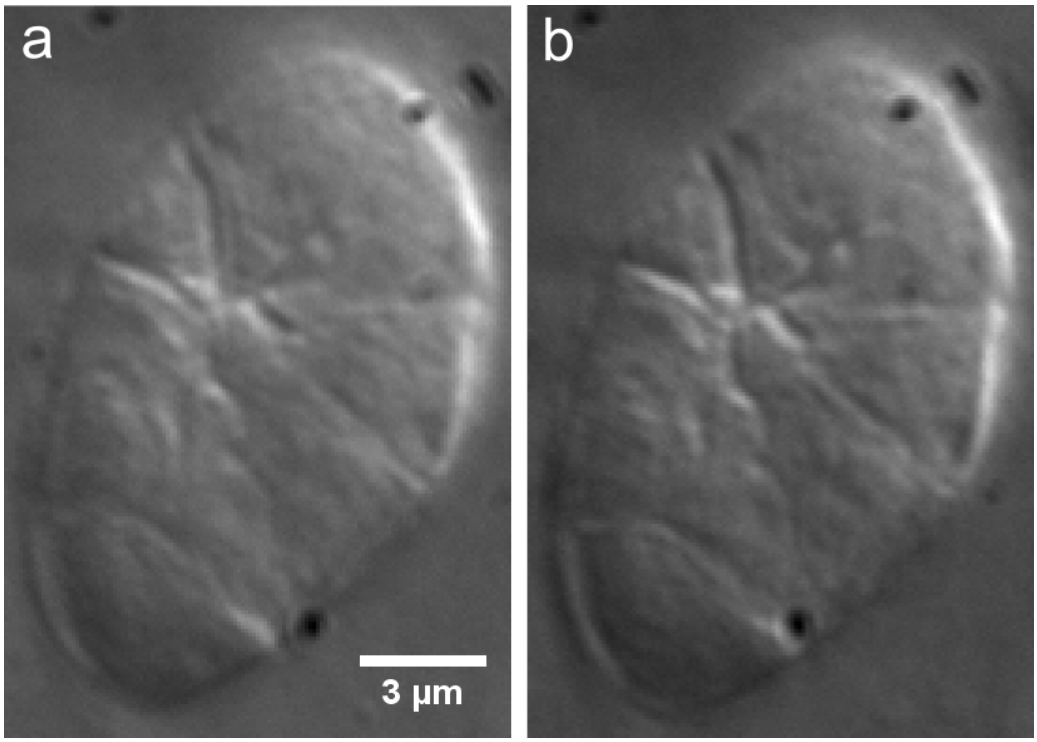

Figure 7.10: DIC images of an unknown feature inside a fruit fly sample before (a) and after (b) image based AO correction.

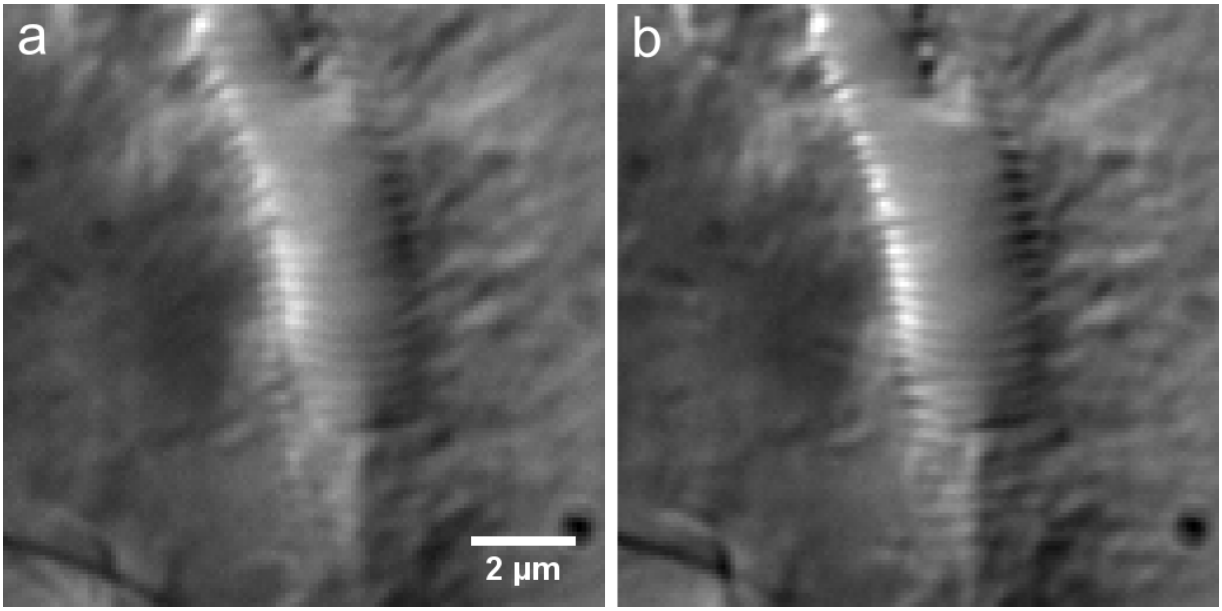

Figure 7.11: DIC images of an unknown feature inside a fruit fly sample before (a) and after (b) image based AO correction.

Aberrations Induced by the DIC Polarizer

Although it blocks 50% of the sample fluorescence, the prism and polarizer required to produce DIC images were not removed to acquire the fluorescence images in the previous experiment. When image based correction with DIC microscopy, aberrations caused by inserting the prism needed for DIC imaging are also removed. If it is then removed to acquire fluorescence images, aberrations will be introduced back into the system. To determine to amount of aberration caused by the polarizer, the wavefronts with and without the filter were calculated and compared using phase retrieval. Ideally, the aberration introduced by the DIC prism could be compensated for so that the maximum amount of fluorescence can be captured after correction with DIC images. Unfortunately, multiple wavefront measurements showed that the aberrations caused by inserting the polarizer are inconsistent. A horizontal profile through three independent wavefront measurements is shown in Figure 7.12. The variation in the aberration is attributed to the loose mounting of the prism inside its mount within the IX71 scope.

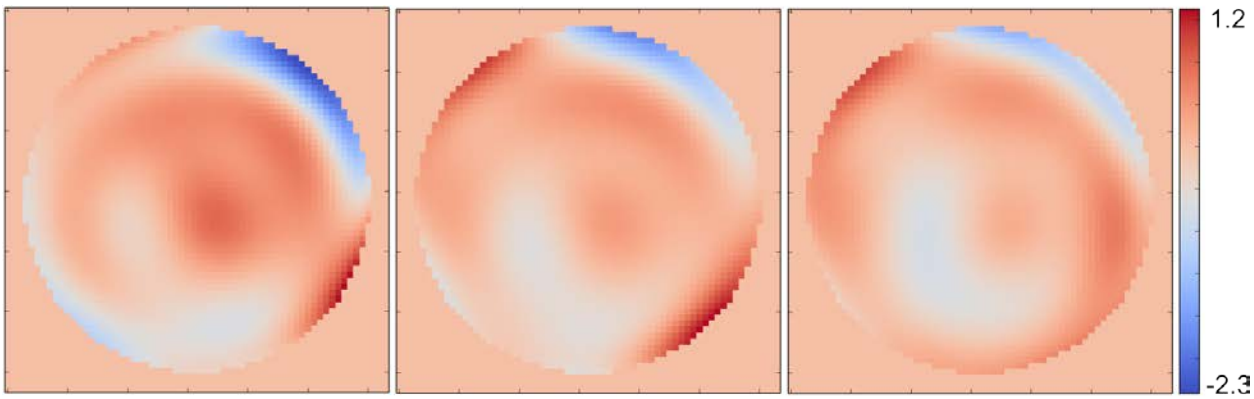

Figure 7.12: Three independent measurements of the wavefront aberrations (in radians) caused by inserting the DIC prism into the optical path.

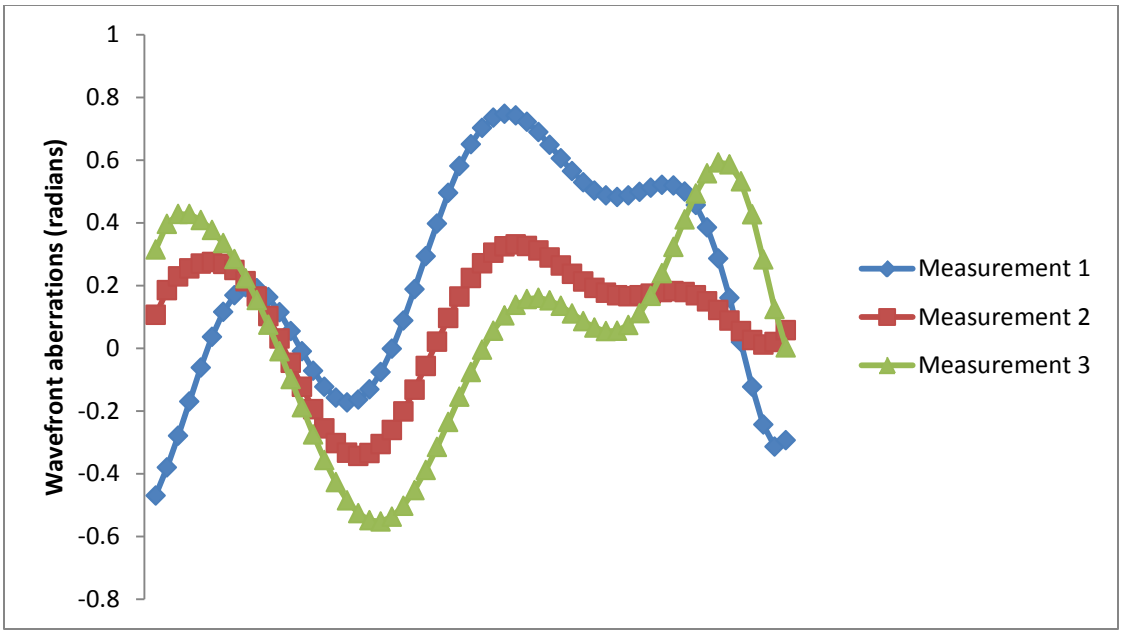

Figure: 7.13: Horizontal profile across the wavefronts aberration caused by inserting the DIC prism into the optical path (Figure 7.12).

Multiple iterations of correction

When multiple modes of aberration exist in an image, multiple iterations are needed to remove as much aberration as possible. To visualize this idea, 0.5nm latex microbeads were fixed to the coverslip. Aberrations were induced at a magnitude of 3 radians for modes 5, 6, 7, 8, and 11. Fourier AO correction was performed as described above. For each iteration and mode, the frequency content was recorded. Figure 7.14 below shows the guess magnitudes for Zernike mode 5, astigmatism. As shown in the Figure, the initial guess for the amount of astigmatism is distorted by other modes of aberration in the system. As other modes are corrected, the estimation of astigmatism becomes clearer, allowing the mirror to converge and eventually apply no more astigmatism correction (as shown by the centrally located peak in

iteration 4). In general, the correction algorithm is allowed to iterate until the total needed correction magnitude for each Zernike aberration falls below 0.5 radians, which typically requires 2-4 iterations.

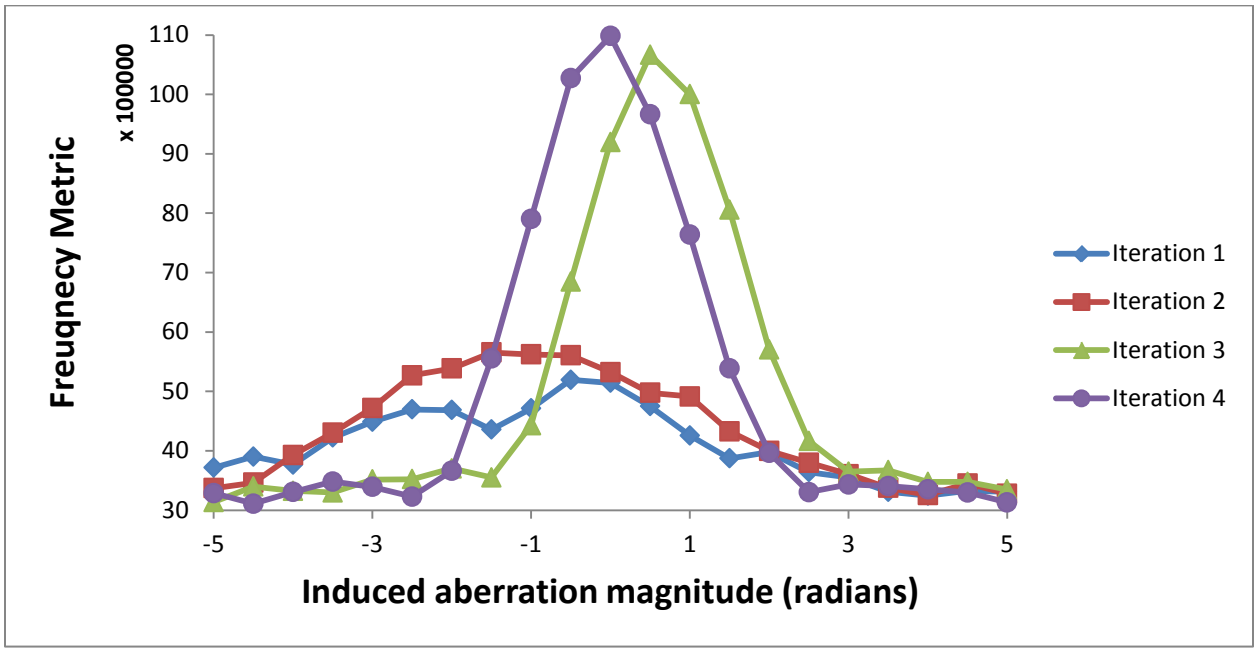

Figure 7.14: Correction of Zernike mode 5 (astigmatism) over four iterations for a latex microbead with induced aberrations of all low order modes.

Chapter Conclusion

In this chapter, wavefront correction using sensorless Adaptive Optics was demonstrated using the frequency content of DIC images. I showed that latex microbeads injected into the sample, or the image of the sample itself could be used to correct sample induced aberrations. This alternate to intensity based metrics allows photosensitive fluorescent targets to be corrected without exciting fluorophores, thus reducing photobleaching. To our knowledge, this is the first reported application of AO to DIC imaging.

Chapter 8 – Conclusion

In this dissertation, I have reviewed my contributions to the fields of Adaptive Optics (AO) and structured illumination microscopy during my graduate career under Dr. Peter Kner. Super-resolution structured illumination microscopy (SR-SIM) is an important method for breaking the diffraction barrier in light microscopy, as extended resolution images can be obtained with a relatively small number of images when compared to other super-resolution techniques. With the addition of an AO system, we have shown that SR-SIM can be extended to thick tissue samples by producing 140nm lateral resolution images of fluorescent microbeads beneath 35μm of *C. elegans* tissue. This is an important step towards super-resolution imaging of biological targets in their natural environments. Portions of this work will be submitted to the Journal of Optical Society of America for publication in January of 2015.

In addition to the combination of AO and SIM, I have also presented our contributions to these individual fields of research. Chapter 5 presented a new method for obtaining optically sectioned images using linear-reconstruction SIM (LR-SIM). This method produces a higher resolution and SNR than the RMS-SI method proposed by Neil et al., which is commonly used. The superiority of LR-SIM over RMS-SI was demonstrated on numerous biological samples. Portions of the data presented in Chapter 5 have been published in the Journal of Optics [84].

In Chapter 7, we demonstrated that image frequency content could be used as a sensorless AO correction metric in Differential Interference Contrast (DIC) microscopy. Although image based correction was proposed by Debarre et al. [43], this study is to our knowledge the first report of its

application to DIC microscopy. This is an important development, as AO correction with DIC requires lower light exposure than fluorescence based corrections and therefore may be useful for photosensitive samples. Portions of this chapter will be submitted for publication in the Journal of Optics in 2015.

Future research will concentrate on the further development of AO and SIM applications to fluorescence microscopy. The combination of DIC AO and full 3D SR-SIM as proposed by Gustafsson [50] may allow photosensitive samples to be imaged at super-resolution in their natural environments. We are also interested in investigating more user friendly methods for SIM image reconstruction, as experience is typically necessary to determine all variables needed for accurate reconstruction.

Bibliography

1. Shimomura, O., F.H. Johnson, and Y. Saiga, *Extraction, Purification and Properties of Aequorin, a Bioluminescent Protein from the Luminous Hydromedusan, Aequorea.* Journal of Cellular and Comparative Physiology, 1962. **59**(3): p. 223-239.
2. Prasher, D.C., et al., *Primary structure of the Aequorea victoria green-fluorescent protein.* Gene, 1992. **111**(2): p. 229-233.
3. Gustafsson, M.G.L., D.A. Agard, and J.W. Sedat. *Doubling the lateral resolution of wide-field fluorescence microscopy using structured illumination*. in *Three-Dimensional and Multidimensional Microscopy: Image Acquisition Processing VII. San Jose, CA.* 2000.
4. Booth, M.J., *Adaptive optics in microscopy.* Philos Transact A Math Phys Eng Sci, 2007. **365**(1861): p. 2829-43.
5. Lakowicz, J.R., *Principles of Fluorescence Spectroscopy*. 2004: Springer.
6. Katz, M., *Introduction to Geometrical Optics*. 2002: World Scientific Publishing Company, Incorporated.
7. Tyson, R.K., *Principles of adaptive optics*. 1998: Academic Press.
8. Hardy, J.W., *Adaptive optics for astronomical telescopes*. Oxford series in optical and imaging sciences ; 16. 1998, New York: Oxford University Press. 438.

9. Goodman, J.W., *Introduction to Fourier Optics*. 2 ed. McGraw-Hill Series in Electrical and Computer Engineering, ed. S.W. Director. 1996, Boston, Massachusetts: McGraw-Hill.

10. Kaletta, T. and M.O. Hengartner, *Finding function in novel targets: C. elegans as a model organism.* Nature reviews. Drug discovery, 2006. **5**(5): p. 387-98.

11. Born, M. and E. Wolf, *Principles of optics : electromagnetic theory of propagation interference and diffraction of light*. 1970: Oxford [etc.] : Pergamon Press.

12. Noll, R.J., *Zernike polynomials and atmospheric turbulence.* J. Opt. Soc. Am., 1976. **66**(3): p. 207-211.

13. Marsh, P.N., D. Burns, and J.M. Girkin, *Practical implementation of adaptive optics in multiphoton microscopy.* Optics Express, 2003. **11**(10): p. 1123 - 1130.

14. Kner, P., et al., *High-resolution wide-field microscopy with adaptive optics for spherical aberration correction and motionless focusing.* Journal of Microscopy, 2010. **237**(2): p. 136-147.

15. Kam, Z., et al., *Modelling the application of adaptive optics to wide-field microscope live imaging.* J Microsc, 2007. **226**(Pt 1): p. 33-42.

16. Azucena, O., et al., *Wavefront aberration measurements and corrections through thick tissue using fluorescent microsphere reference beacons.* Opt. Express, 2010. **18**(16): p. 17521-17532.

17. Babcock, H.W., *The possibility of compensating astronomical seeing.* Publications of the Astronomical Society of the Pacific, 1953: p. 229-236.

18. Max, C. *Astronomy 289C --Adaptive Optics*. 2006; Available from: http://www.ucolick.org/~max/289C/.

19. Foucault, L., *Description des procedes employes pour reconnaitre la configuration des surfaces optiques.* Comptes rendus hebdomadiares des seances de l'Academie des Scineces **47**: p. 958-959.

20. Roddier, F., *Curvature sensing and compensation: a new concept in adaptive optics.* Applied Optics, 1988. **27**(7): p. 1223-1225.

21. Booth, M.J., *Wavefront sensorless adaptive optics for large aberrations.* Opt Lett, 2007. **32**(1): p. 5-7.

22. Booth, M.J., et al., *Adaptive aberration correction in a confocal microscope.* Proc Natl Acad Sci U S A, 2002. **99**(9): p. 5788-92.

23. Sherman, L., et al., *Adaptive correction of depth-induced aberrations in multiphoton scanning microscopy using a deformable mirror.* J Microsc, 2002. **206**(Pt 1): p. 65-71.

24. Neil, M.A.A., et al., *Adaptive aberration correction in a two-photon microscope.* Journal of Microscopy, 2000. **200**(2): p. 105-108.

25. Neil, M.A.A., M.J. Booth, and T. Wilson, *Closed-loop aberration correction by use of a modal Zernike wave-front sensor.* Optics Letters, 2000. **25**(15): p. 1083-1085.

26. Freeman, R.H. and J.E. Pearson, *Deformable mirrors for all seasons and reasons.* Applied Optics, 1982. **21**(4): p. 580-588.

27. Kam, Z., et al., *Modelling the application of adaptive optics to wide-field microscope live imaging.* Journal of microscopy, 2007. **226**(1): p. 33-42.

28. Albert, O., et al., *Smart microscope: an adaptive optics learning system for aberration correction in multiphoton confocal microscopy.* Opt. Lett., 2000. **25**(1): p. 52-54.

29. Rueckel, M., J.A. Mack-Bucher, and W. Denk, *Adaptive wavefront correction in two-photon microscopy using coherence-gated wavefront sensing.* Proceedings of the National Academy of Sciences, 2006. **103**(46): p. 17137-17142.

30. Jesacher, A., et al., *Adaptive harmonic generation microscopy of mammalian embryos.* Optics Letters, 2009. **34**(20): p. 3154-3156.

31. Débarre, D., et al., *Adaptive optics for structured illumination microscopy.* Optics Express, 2008. **16**(13): p. 9290-9305.

32. Denk, W., J.H. Strickler, and W.W. Webb, *Two-photon laser scanning fluorescence microscopy.* Science, 1990. **248**(4951): p. 73-76.

33. Göppert-Mayer, M., *Über elementarakte mit zwei quantensprüngen.* Annalen der Physik, 1931. **401**(3): p. 273-294.

34. So, P.T., *Two-photon Fluorescence Light Microscopy.* eLS, 2001.

35. Chang, C.Y., et al. *Widefield multiphoton microscopy with image-based adaptive optics*. 2012.

36. Ji, N., D.E. Milkie, and E. Betzig, *Adaptive optics via pupil segmentation for high-resolution imaging in biological tissues.* Nat Methods, 2010. **7**(2): p. 141-7.

37. Pawley, J., *Handbook of biological confocal microscopy*. 2010: Springer.

38. Tao, X., et al., *Adaptive optics confocal microscopy using direct wavefront sensing.* Opt. Lett., 2011. **36**(7): p. 1062-1064.

39. Tao, X., et al., *Adaptive optics microscopy with direct wavefront sensing using fluorescent protein guide stars.* Optics letters, 2011. **36**(17): p. 3389-3391.

40. Franken, P., et al., *Generation of optical harmonics.* Physical Review Letters, 1961. **7**(4): p. 118-119.

41. Schwertner, M., M. Booth, and T. Wilson, *Characterizing specimen induced aberrations for high NA adaptive optical microscopy.* Opt Express, 2004. **12**(26): p. 6540-52.

42. Vermeulen, P., et al., *Adaptive optics for fluorescence wide-field microscopy using spectrally independent guide star and markers.* Journal of Biomedical Optics, 2011. **16**(7): p. 076019-076019-8.

43. Debarre, D., M.J. Booth, and T. Wilson, *Image based adaptive optics through optimisation of low spatial frequencies.* Opt. Express, 2007. **15**(13): p. 8176-8190.

44. Hell, S.W. and J. Wichmann, *Breaking the diffraction resolution limit by stimulated emission: stimulated-emission-depletion fluorescence microscopy.* Opt. Lett., 1994. **19**(11): p. 780-782.

45. Betzig, E., et al., *Imaging intracellular fluorescent proteins at nanometer resolution.* Science, 2006. **313**(5793): p. 1642-5.

46. Hess, S.T., T.P.K. Girirajan, and M.D. Mason, *Ultra-High Resolution Imaging by Fluorescence Photoactivation Localization Microscopy.* Biophys. J., 2006. **91**(11): p. 4258-4272.

47. Rust, M.J., M. Bates, and X. Zhuang, *Sub-diffraction-limit imaging by stochastic optical reconstruction microscopy (STORM).* Nat Meth, 2006. **3**(10): p. 793-796.

48. Gustafsson, M.G., *Surpassing the lateral resolution limit by a factor of two using structured illumination microscopy.* J Microsc, 2000. **198**(Pt 2): p. 82-7.

49. Heintzmann, R. and C.G. Cremer. *Laterally modulated excitation microscopy: improvement of resolution by using a diffraction grating*. in *Proc. of the SPIE*. 1999. Stockholm, Sweden: SPIE.

50. Gustafsson, M.G.L., et al., *Three-Dimensional Resolution Doubling in Wide-Field Fluorescence Microscopy by Structured Illumination.* Biophys. J., 2008. **94**(12): p. 4957-4970.

51. Shao, L., et al., *Super-resolution 3D microscopy of live whole cells using structured illumination.* Nature methods, 2011. **8**(12): p. 1044-6.

52. Fiolka, R., et al., *Time-lapse two-color 3D imaging of live cells with doubled resolution using structured illumination.* Proceedings of the National Academy of Sciences, 2012. **109**(14): p. 5311-5315.

53. Gustafsson, M.G., *Nonlinear structured-illumination microscopy: wide-field fluorescence imaging with theoretically unlimited resolution.* Proc Natl Acad Sci U S A, 2005. **102**(37): p. 13081-6.

54. Somekh, M.G., K. Hsu, and M.C. Pitter, *Resolution in structured illumination microscopy: a probabilistic approach.* Journal of the Optical Society of America A, 2008. **25**(6): p. 1319-1329.

55. Neil, M.A.A., R. Juskaitis, and T. Wilson, *Method of obtaining optical sectioning by using structured light in a conventional microscope.* Optics Letters, 1997. **22**(24): p. 1905-7.

56. Karadaglić, D. and T. Wilson, *Image formation in structured illumination wide-field fluorescence microscopy.* Micron, 2008. **39**(7): p. 808-818.

57. Heintzmann, R. and P.A. Benedetti, *High-resolution image reconstruction in fluorescence microscopy with patterned excitation.* Appl. Opt., 2006. **45**(20): p. 5037-5045.

58. Lim, D., et al., *Optically sectioned in vivo imaging with speckle illumination HiLo microscopy.* Journal of Biomedical Optics, 2011. **16**(1): p. 016014-016014.

59. Karadaglic, D. and T. Wilson, *Image formation in structured illumination wide-field fluorescence microscopy.* Micron, 2008. **39**(7): p. 808-18.

60. Axelrod, D., *Cell-substrate contacts illuminated by total internal reflection fluorescence.* J Cell Biol, 1981. **89**(1): p. 141-5.

61. Fiolka, R., M. Beck, and A. Stemmer, *Structured illumination in total internal reflection fluorescence microscopy using a spatial light modulator.* Opt. Lett., 2008. **33**(14): p. 1629-1631.

62. Kner, P., et al., *Super-resolution video microscopy of live cells by structured illumination.* Nat Methods, 2009. **6**(5): p. 339-42.

63. Cai, D., K.J. Verhey, and E. Meyhofer, *Tracking Single Kinesin Molecules in the Cytoplasm of Mammalian Cells.* Biophys. J., 2007. **92**(12): p. 4137-4144.

64. Heintzmann, R., T.M. Jovin, and C. Cremer, *Saturated patterned excitation microscopy – a concept for optical resolution improvement.* J. Opt. Soc. Am. A, 2002. **19**(8): p. 1599-1609.

65. Rego, E.H., et al., *Nonlinear structured-illumination microscopy with a photoswitchable protein reveals cellular structures at 50-nm resolution.* Proceedings of the National Academy of Sciences, 2012. **109**(3): p. E135-E143.

66. Débarre, D., et al., *Adaptive optics for structured illumination microscopy.* Opt. Express, 2008. **16**(13): p. 9290-9305.

67. Kner, P., et al. *Closed loop adaptive optics for microscopy without a wavefront sensor*. in *SPIE (Three-Dimensional and Multidimensional Microscopy: Image Acquisition and Processing XVII)*. 2010. San Francisco, California, USA: SPIE.

68. Hanser, B.M., et al., *Phase retrieval for high-numerical-aperture optical systems.* Optics Letters, 2003. **28**(10): p. 801-3.

69. Deming, R.W., *Phase retrieval from intensity-only data by relative entropy minimization.* J. Opt. Soc. Am. A, 2007. **24**(11): p. 3666-3679.

70. Zhao, C.Y. and J.H. Burge, *Orthonormal vector polynomials in a unit circle, Part I: basis set derived from gradients of Zernike polynomials.* Optics Express, 2007. **15**(26): p. 18014-18024.

71. Zhao, C.Y. and J.H. Burge, *Orthonormal vector polynomials in a unit circle, Part II : completing the basis set.* Optics Express, 2008. **16**(9): p. 6586-6591.

72. Swedlow, J.R., J.W. Sedat, and D.A. Agard, *Deconvolution in Optical Microscopy*, in *Deconvolution of Images and Spectra*, P.A. Jansson, Editor. 1997, Academic Press, Inc.: San Diego, CA. p. 284-307.

73. Hagen, N., L. Gao, and T.S. Tkaczyk, *Quantitative sectioning and noise analysis for structured illumination microscopy.* Opt. Express, 2012. **20**(1): p. 403-413.

74. Stokseth, P.A., *Properties of a Defocused Optical System.* J. Opt. Soc. Am., 1969. **59**(10): p. 1314-1321.

75. Hernandez-Rodriguez, Y., S. Hastings, and M. Momany, *The septin AspB in Aspergillus nidulans forms bars and filaments and plays roles in growth emergence and conidiation.* Eukaryotic cell, 2012. **11**(3): p. 311-23.

76. Spiliotis, E.T. and A.S. Gladfelter, *Spatial guidance of cell asymmetry: septin GTPases show the way.* Traffic, 2012. **13**(2): p. 195-203.

77. Gavel, D. *Suppressing Anomalous Localized Waffle Behavior in Least Squares Wavefront Reconstructors*. in *Proceedings of SPIE*. 2003. Waikoloa, HI, USA: SPIE.

78. Swoger, J., et al., *Multi-view image fusion improves resolution in three-dimensional microscopy.* Optics express, 2007. **15**(13): p. 8029-8042.

79. Hamahashi, S., S. Onami, and H. Kitano, *Detection of nuclei in 4D Nomarski DIC microscope images of early Caenorhabditis elegans embryos using local image entropy and object tracking.* BMC bioinformatics, 2005. **6**: p. 125.

80. Easter Jr, S.S. and G.N. Nicola, *The Development of Vision in the Zebrafish (< i> Danio rerio</i>).* Developmental biology, 1996. **180**(2): p. 646-663.

81. Preza, C., D.L. Snyder, and J.-A. Conchello, *Theoretical development and experimental evaluation of imaging models for differential-interference-contrast microscopy.* J. Opt. Soc. Am. A, 1999. **16**(9): p. 2185-2199.

82. Mehta, S.B. and C.J. Sheppard, *Partially coherent image formation in differential interference contrast (DIC)microscope.* Opt. Express, 2008. **16**(24): p. 19462-19479.

83. . World Health Organization.

84. Thomas, B., M. Momany, and P. Kner, *Optical sectioning structured illumination microscopy with enhanced sensitivity.* Journal of Optics, 2013: p. In Review.